Strongly Interacting Fermions in Optical Lattices

PhD Thesis

Arnaud Koetsier

Koetsier, Arnaud

Strongly Interacting Fermions in Optical Lattices
PhD thesis
Institute for Theoretical Physics
Utrecht University
ISBN/EAN: 978-9-09-024407-5
Printed by Gildeprint Drukkerijen, The Netherlands

Strongly Interacting Fermions in Optical Lattices

Sterk Wisselwerkende Fermionen in Optische Roosters

(met een samenvatting in het Nederlands)

Proefschrift

ter verkrijging van de graad van doctor aan de Universiteit Utrecht op gezag van de rector magnificus, prof.dr. J.C. Stoof, ingevolge het besluit van het college voor promoties in het openbaar te verdedigen op maandag 6 juli 2009 des middags te 2.30 uur

door

Arnaud Olav Koetsier

geboren op 16 september 1980 te Parijs, Frankrijk

Promotor: Prof.dr.ir. H. T. C. Stoof

This thesis was accomplished with financial support from the Stichting voor Fundamenteel Onderzoek der Materie (FOM) and the Nederlandse Organisatie voor Wetenschaplijk Onderzoek (NWO).

To my father, Albert (1931-2005)

Contents

1 Introduction

Bose-Einstein condensation

The surprising phenomenon of Bose-Einstein condensation was theoretically conjectured some 85 years ago. At that time, Indian physicist Satyendra Nath Bose was working on a statistical description of light quanta to explain the Plank spectrum of black-body radiation. He communicated his work to Einstein, who promptly generalised Bose's theory to a noninteracting gas of indistinguishable matter particles, now known as bosons [1, 2]. That same year, Einstein realised that, below a certain critical temperature, a nonzero fraction of the bosons would occupy the same single-particle ground state with zero momentum. This new state of matter, now known as a Bose-Einstein condensate (BEC), was predicted to have many unusual properties and soon became the subject of intense scrutiny. Creating a Bose-Einstein condensate using bosonic atoms, namely, neutral atoms with an integer total spin quantum number, became a major experimental goal.

One remarkable property of Bose-Einstein condensates is their superfluidity, i.e., they show a persistent flow without viscous damping. This feature was observed in 1937 by Pyotr Kapitsa, John F. Allen, and Don Misener by cooling liquid ^{4}He to below a temperature of 2.17 K, called the lambda point [3, 4]. However, the high densities of liquid ^{4}He leads to strong interactions between the particles. Thus, this system is very different from the noninteracting Bose gas considered by Einstein, and is indeed impossible to treat analytically from first principles. Moreover,

the strong interactions dramatically reduce the occupancy of the single-particle zero-momentum state. Indeed, only about 10% of the superfluid is in fact Bose-Einstein condensed. This sparked the desire to create a weakly interacting Bose gas that would allow for a higher condensate fraction. Using techniques of laser cooling [5], evaporative cooling [6], and magnetic trapping of neutral atoms [7], such a weakly interacting Bose-Einstein condensate was finally realised in 1995 in a dilute gas of rubidium atoms cooled to 170 nK, by the group of Eric Cornell, and Carl Wieman [8]. Within a few months, this success was repeated with lithium and sodium in the groups of Randy Hulet and Wolfgang Ketterle, respectively [9, 10].

Fermions

Since Bose-Einstein condensation can only occur with bosons due to the Pauli principle, its relevance to the previously established phenomenon of the superconductivity of fermions eluded most physicists at the time. Superconductivity was discovered in 1911 by Dutch physicist Heike Kamerlingh-Onnes, who observed that the electrical resistivity of Mercury suddenly disappeared below a critical temperature of $T_c = 4.2$ K [11–14]. Early theoretical studies of superconductivity succeeded in explaining certain macroscopic aspects of the phenomenon, but the precise mechanism behind superconductivity remained mysterious until 1957 when John Bardeen, Leon Cooper and Robert Schrieffer formulated a microscopic theory of superconductivity, the now well known BCS theory [15]. In BCS theory, two electrons of opposite spin form a pair in the vicinity of the Fermi surface, called a Cooper pair, through a phonon-mediated attractive interaction. Being bosonic in character, Cooper pairs can Bose-Einstein condense and it is precisely the appearance of this Bose-Einstein condensate of Cooper pairs below the critical temperature that is posited as the cause of superconductivity. It soon became apparent that Bose-Einstein condensation of pairs of fermions could also find application in the understanding of a host of other systems. The fermionic isotope of helium, ^{3}He, was discovered[1] to exhibit superfluidity below 2 mK. Manifestations of nucleon condensates can be seen in the excitation spectrum of atomic nuclei, the possibility of meson condensates in the cores of neutron stars has been widely discussed, and in quantum chromodynamics the condensation of quark-antiquark pairs forms a chiral condensate that is partly responsible for giving rise to the mass of nuclear particles [16–24].

Soon after Bose-Einstein condensation was achieved in a Bose gas, it was predicted that a BEC could also be observed in a weakly interacting gas of fermionic atoms through the pairing of two fermions in different hyperfine states [25], and several experimental groups turned to achieving this goal. However, this proved significantly more challenging than Bose-Einstein condensing bosonic atoms. Indeed, due to the antisymmetry of the fermion wavefunction, the scattering cross section of fermionic atoms in the same state must vanish at zero energy. In a gas comprised of a single fermionic spin species, this prevents rethermalization of the atom cloud through elastic collisions which is essential for the evaporative cooling stage. The solution, called *sympathetic* cooling, was to mix the fermionic atoms with another species of fermion or boson enabling them to rethermalize by proxy of the other species [26, 27]. This enabled the creation of degenerate Fermi gases cooled to within one quarter of the Fermi temperature [28, 29].

A further complication arises from the Pauli principle which forbids fermions from Bose-Einstein condensing solitarily. Instead, a bound state of two fermions must first be formed. A crucial ingredient to solving this problem was the exploitation of a Feshbach resonance through the application of a bias magnetic field. The Feshbach resonance is responsible for the appearance of a stable bound state within a certain range of magnetic field strengths, and populating this state permitted the creation of the first weakly interacting paired-fermion condensates with ^{40}K [30] and ^{6}Li [31, 32] which were reported at the end of 2003.

As explained further in chapter 5, a Feshbach resonance enables the interaction strength of the atoms, which is characterised by the s-wave scattering length a, to be adjusted by varying the strength of the bias magnetic field [33, 34]. This relationship is shown in Fig. 1.1 for the much used broad Feshbach resonance in ^{6}Li [35]. A particularly interesting aspect of the Feshbach resonance that it links two distinct regimes of fermion pairing. In the 2003 fermion experiments, pair condensation was achieved in a regime where the magnetic field is below but close to the resonant value. On this low magnetic-field side of the Feshbach resonance, $a > 0$ close to the resonance and the atoms effectively repel each other. Moreover, a paired state exists with an energy that is below the energy of two unpaired atoms. Thus, it is energetically favourable for two atoms to form a tightly bound bosonic pair which can then Bose-Einstein condense. This regime is called the BEC limit and the tightly bound pair present in

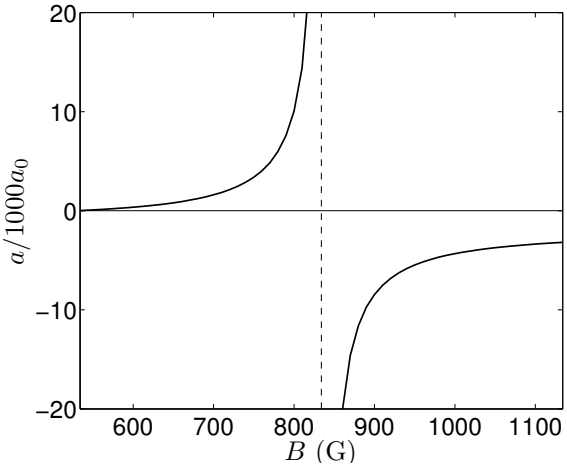

Figure 1.1: Dependence of the scattering length a on the magnetic field B for ^{6}Li. The Feshbach resonance at $B_0 = 834$ G is indicated by the dashed line. Here, a_0 is the Bohr radius.

this case is typically referred to as a molecule. A Bose-Einstein condensate of molecules in the BEC limit behaves similarly to a Bose-Einstein condensate of bosons, however, the other side of the Feshbach resonance is more interesting. There, the atomic interaction is attractive with $a < 0$, and the pairing is strictly a many-body effect reminiscent of the Cooper pairing of electrons in BCS theory. This regime is typically referred to as the BCS limit, and the continuous connection between the deeply bound Bose-Einstein condensate of molecules and the weakly bound BCS pairs is known as the BEC-BCS crossover, which is discussed in more detail in chapter 5.

One additional obstacle to achieving the superfluidity of BCS pairs arises due to the dependence of the critical temperature on the interaction strength of the atoms in the BCS limit, namely, $T_c \propto e^{-\pi/2k_F|a|}$ where $k_F = (3\pi^2 n)^{1/3}$ is the Fermi wave vector in an ideal Fermi gas with total density n. In typical experiments, the sample is dilute, hence $k_F|a| \ll 1$, and the resulting low critical temperature is beyond the reach of experiments. However, the Feshbach resonance can be used to tune the scattering length such that $k_F|a| \gg 1$ where the critical temperature becomes comparable to that of Bose-Einstein condensation in an atomic Bose gas. In this way, soon after the realisation of Bose-Einstein condensates of molecules in the BEC limit, BCS-like pair condensates were observed in the group of Debbie Jin

using ^{40}K atoms [36], and the groups of Wolfgang Ketterle, John Thomas, Rudi Grimm, Christophe Salomon, and Randy Hulet using ^{6}Li [37–41]. It is interesting to mention here that there is also a counterintuitive analogy of the BEC-BCS crossover in Bose gases which is explored in chapter 7.

Optical Lattices

The successes of experiments with ultracold atomic gases of the past few decades have opened up a number of exciting possibilities to study various quantum many-body phenomena in depth which were previously unaccessible. One avenue of research attracting a lot of attention is the study of atomic gases in periodic potentials, called optical lattices, created using counter-propagating laser beams [42]. Studying ultracold fermions in optical lattices opens the possibility to explore experimentally a number of effects which are difficult to observe for electrons in the periodic lattice of a solid. An important example is the study of the poorly understood phenomenon of high-temperature superconductivity, which was first seen in 1986 [43]. There, ceramic materials consisting of different insulating layers which separate CuO_2 planes, called perovskite planes, become superconducting at critical temperatures that are distinctly higher than for conventional superconductors such as Mercury[2]. The regular lattice of electronic orbitals in the perovskite planes form a periodic potential for the electrons which are believed to be described by the famous Hubbard model [44, 45], discussed in more detail in chapter 2. However, despite an arsenal of methods ranging from various many-body theories to numerical approaches, it has turned out not to be possible to uncover the mechanism of how superconductivity arises. Due to their high degree of experimental tunability, cold atomic fermions in optical lattices, which are accurately described by the Hubbard model [46], offer the exciting possibility of gaining more insight into this problem.

There are, however, many other incentives to study atomic gases in optical lattices. By adjusting the laser intensities in various directions, stacks of two-dimensional pancakes or one-dimensional cigar-shaped traps can be created permitting the study of low-dimensional quantum systems, and arrays of two- and one-dimensional lattice potentials can be similarly realised. Also, by altering the configuration of the lasers, the geometry of the lattice can also be changed to study frustration effects in quantum magnetism. As discussed in chapter 3, changing the depth of the lat-

tice potential can cool a Fermi gas into an antiferromagnetic state under certain circumstances, and changing the lattice depth can also give rise to a quantum phase transition known as the superfluid to Mott-insulator transition in Bose gases [47], which has been recently observed [48]. The BEC-BCS crossover can also be studied in a optical lattice and, curiously, takes place far above the Feshbach resonance, as discussed in chapter 6. Another interesting direction with far-reaching implications is the study of two-component Fermi gases that are imbalanced, i.e., with an excess of one spin species over the other. In order to maximise the number of pairs, the seminal paired-fermion condensation experiments were performed with balanced Fermi gases, i.e., with an equal number of each spin species. The question of what precisely happens if the gas is imbalanced has been hotly debated following recent experiments with imbalanced Fermi gases [49,50]. In chapter 4 we address precisely this question in the context of antiferromagnetism in an optical lattice, and find the appearance of a canted antiferromagnetic phase as well as a Kosterlitz-Thouless topological phase transition in the two-dimensional case.

* * *

The first part of this thesis focuses on a special limit of the Hubbard model called the Heisenberg model which is derived in chapter 2, and applications of this model in an ultracold fermionic gas are discussed in chapters 3 and 4. In the second part, consisting of chapters 5, 6 and 7, we introduce the BEC-BCS crossover and explore this phenomenon for fermions in optical lattices and for a homogeneous gas of bosons.

Notes

1. The discovery of superfluid ^{3}He in 1972 by Lee, Richardson and Osheroff earned them the 1996 Nobel prize [51]. They originally believed the new phase they observed was a solid, however, this was cleared up in a subsequent paper [52].
2. Although we mention cuperate superconductors here, which have exhibited critical temperatures has high as $T_c = 138$ K [53,54], there exist other families of high-T_c superconductors such as the Fullerides [55] and the recently discovered iron- and nickel-based compounds with critical temperatures up to $T_c = 43$ K [56,57].

2 Hubbard model

The Hubbard model was originally proposed by John Hubbard in 1963 to describe valence electrons in solids in the limit where they are strongly localised on the ion cores [58]. In this approximation, known as the tight-binding limit, the electrons are viewed as occupying the standard atomic orbitals of their atom and the effect of the lattice is taken into account by allowing the electrons to hop to adjacent atoms. Here, we shall focus on the Hubbard model with repulsive on-site interactions, known as the positive-U Hubbard model, which is thought to embody the physics of high-temperature superconductors [59, 60]. The negative-U Hubbard model which has attractive on-site interactions is considered in chapter 6.

2.1 The single-band Hubbard model in an optical lattice

Typically, the starting point for studies of high-temperature superconductivity in the cuprates is a three-band Hubbard model. This model consists of three atomic orbitals with terms accounting for electronic hops between orbitals, as well as hops to orbitals on nearest-neighbouring atoms. The three-band Hubbard model is very complicated, especially when doping and electron-electron interactions are taken into account, and much of the theoretical work in this area of physics revolves around simplifications of this model. Nevertheless, it remains difficult to know whether the superconductivity is really present in the Hubbard model, or whether it arises due to an extra ingredient. In that respect, cold atomic systems provide

an interesting alternative route to tackling this fundamental question.

The idea of trapping atoms in optical lattices was first suggested by Letokhov in 1968 and achieved twenty years later in a nondegenerate gas of cesium atoms [61, 62]. However, the Hubbard model with ultracold fermions has only recently become available [63, 64]. Here we consider the single-band Hubbard model which is realised by cold atoms when the lattice potential is strong enough such that only the lowest band is populated [46, 65].

The single-band Hubbard Hamiltonian can be written as

$$H = -t \sum_{\sigma} \sum_{\langle i,j \rangle} c^{\dagger}_{i,\sigma} c_{j,\sigma} + U \sum_{i} c^{\dagger}_{i,\uparrow} c^{\dagger}_{i,\downarrow} c_{i,\downarrow} c_{i,\uparrow}, \tag{2.1}$$

where $c^{\dagger}_{i,\sigma}$ ($c^{\dagger}_{i,\sigma}$) creates (annihilates) a fermion with spin $\sigma \in \{\uparrow, \downarrow\}$ on a lattice site labeled by i, and $\langle i, j \rangle$ denotes the sum over nearest-neighbour sites. The first term in Eq. (2.1) is a kinetic term that accounts for hopping to adjacent lattice sites, and the second term is the on-site interaction. For repulsive on-site interactions of interest here, $U > 0$ such that it costs energy to multiply occupy lattice sites.

Since we are not concerned with frustration effects here, and for the sake of simplicity, we shall consider only bipartite Bravias lattices with an even number of sites. To see how this model is achieved in such an optical lattice, we begin by writing the isotropic optical lattice potential as

$$V^{\mathrm{ex}}(\mathbf{x}) = \sum_{\nu} V_0 \cos^2(2\pi x_\nu / \lambda), \tag{2.2}$$

where λ is the wavelength of the lattice lasers, and V_0 is the peak-to-trough depth of the lattice potential[1]. The second-quantised, grand-canonical Hamiltonian for an atomic Fermi gas in this potential is given by

$$H = \sum_{\sigma} \int d^3\mathbf{x}\, \psi^{\dagger}_{\sigma}(\mathbf{x}) \left(-\frac{\hbar^2 \nabla^2}{2m} - \mu_\sigma + V^{\mathrm{ex}}(\mathbf{x}) \right) \psi_\sigma(\mathbf{x}) + T^{\mathrm{2B}} \int d^3\mathbf{x} \psi^{\dagger}_{\uparrow}(\mathbf{x}) \psi^{\dagger}_{\downarrow}(\mathbf{x}) \psi_{\downarrow}(\mathbf{x}) \psi_{\uparrow}(\mathbf{x}) \tag{2.3}$$

where $\psi^{(\dagger)}_{\sigma}(\mathbf{x})$ is the annihilation (creation) operator of a particle at position $\mathbf{x}$ in hyperfine state $\sigma \in \{\uparrow, \downarrow\}$, μ_σ is the chemical potential for the σ species and m is the mass of the atom. Here, we have taken a contact interaction which is valid since the thermal de Broglie wavelength of the

atoms is for the ultra-low temperature of interest always much larger than the typical range of the interaction. The effective strength of the atom-atom interaction is then well approximated by the two-body T-matrix, $T^{2\mathrm{B}} = 4\pi\hbar^2 a/m$ where a is the s-wave scattering length.

The Hamiltonian can be approximated by an on-site Hamiltonian which is obtained by expanding the fields in terms of orthonormal Wannier states of the lattice $\chi_b(\mathbf{x})$ with the band index b, i.e.,

$$\psi_\sigma^{(\dagger)}(\mathbf{x}) = \sum_{b,i} c_{i,\sigma,b}^{(\dagger)} \chi_b^{(*)}(\mathbf{x} - \mathbf{x}_i). \tag{2.4}$$

where i labels the lattice sites. At sufficiently low temperatures, the atoms will form a Fermi sea in the lowest band of the lattice. In this case, we can take $b = 0$ and neglect the band index hereafter. The Hamiltonian then becomes

$$H = \sum_{\sigma,i} (\varepsilon - \mu_\sigma) c_{i,\sigma}^\dagger c_{i,\sigma} - \sum_{\sigma,\langle i,j\rangle} t c_{i,\sigma}^\dagger c_{j,\sigma} + U \sum_i c_{i,\uparrow}^\dagger c_{i,\downarrow}^\dagger c_{i,\downarrow} c_{i,\uparrow}. \tag{2.5}$$

Here, the average energy in the tight-binding band is

$$\varepsilon = \int d^3\mathbf{x} \chi^*(\mathbf{x} - \mathbf{x}_i) \left(-\frac{\hbar^2 \nabla^2}{2m} + V^{\mathrm{ex}}(\mathbf{x}) \right) \chi(\mathbf{x} - \mathbf{x}_i), \tag{2.6}$$

which is independent of the position and spin in the isotropic lattice of interest, the on-site interaction energy is

$$U = T^{2B} \int d^3\mathbf{x} |\chi(\mathbf{x} - \mathbf{x}_j)|^4, \tag{2.7}$$

and the nearest-neighbour tunneling amplitude is

$$t = -\int d^3\mathbf{x} \chi^*(\mathbf{x} - \mathbf{x}_i) \left(-\frac{\hbar^2 \nabla^2}{2m} + V^{\mathrm{ex}}(\mathbf{x}) \right) \chi(\mathbf{x} - \mathbf{x}_j) \tag{2.8}$$

which is also not site-dependent since we restrict ourselves to nearest-neighbour interactions. The wavefunctions, $\chi(\mathbf{x} - \mathbf{x}_i)$ are the Wannier functions in the lowest band of the optical lattice.

In the tight-binding limit, corresponding to a deep lattice potential, the atoms at low temperatures reside near the bottom of the on-site potentials which are then well approximated by harmonic potentials. In this case, the

Wannier functions reduce to Gaussian functions and the on-site interaction energy becomes

$$U = \frac{8\sqrt{\pi}\hbar^2}{m}\frac{a}{l} \tag{2.9}$$

where $l = \sqrt{\hbar/m\omega}$ is the on-site harmonic oscillator length [66]. However, this approximation underestimates the tunneling amplitude which is sensitive to the precise form of the tails of the Wannier wavefunctions. Instead, the tunneling is calculated by solving the single-particle Schrödinger equation exactly in the tight-binding limit, which results in [67]

$$t = 4\left(\frac{V_0^3 E^{\mathrm{R}}}{\pi^2}\right)^{\frac{1}{4}} \exp\left(-2\sqrt{\frac{V_0}{E_{\mathrm{R}}}}\right), \tag{2.10}$$

where

$$E_{\mathrm{R}} = \frac{(2\pi\hbar)^2}{2m}\frac{1}{\lambda^2} \tag{2.11}$$

is the recoil energy of atom initially at rest after absorbing a single photon with wavelength λ from the lattice laser. Eq. (2.9) and Eq. (2.10) describe how the single-band Hubbard Hamiltonian in Eq. (2.1) is realised with ultracold Fermions in an optical lattice.

The phases of this model are illustrated in Fig. 2.1. At for large U and at half filling, corresponding to one fermion per lattice site, the system is an insulator in the lowest band of the lattice since any hopping would doubly occupy a lattice site, which entails an energy cost U on top of the energy cost of hopping alone. This incompressible state is known as the Mott insulator[2], and was recently observed in an ultacold fermionic atom gas [63, 64]. For any other fillings below unit filling the system is conducting. However, hopping is suppressed at unit filling by the energy cost of occupying a higher band, and the system then becomes a band insulator. This band insulator has also been seen experimentally with ultracold fermions [68].

2.2 Strong-coupling limit: Heisenberg Model

In the limit of strong coupling $t/U \ll 1$ and at half filling, the system is a Mott insulator and configurations with doubly occupied sites are energetically suppressed. However, quantum mechanically, there remains a small probability for a particle to hop to an adjacent site which becomes doubly occupied, so long as the other particle on the doubly occupied site

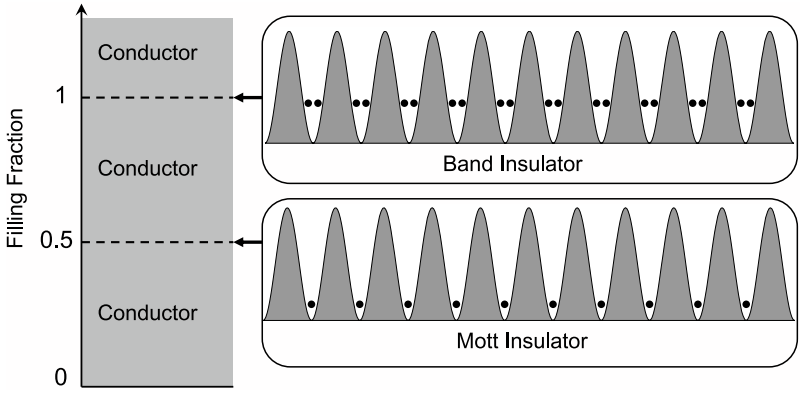

Figure 2.1: Phases of the Hubbard model at various filling factors. The system is a Mott insulator at half-filling, and a band insulator at unit filling. For other filling factors, the system is conducting as hopping is not energetically suppressed.

returns to the original site. This is known as the superexchange mechanism. Formally, the Gaussian quantum fluctuations corresponding to these virtual excursions to adjacent sites can be integrated out from the strong coupling half-filled Hubbard model, which produces the following effective Hamiltonian for the atoms,

$$H_{\text{eff}} = -\frac{J}{4}\sum_{\sigma,\sigma'}\sum_{\langle i,j\rangle} c^{\dagger}_{i,\sigma}c_{j,\sigma}n_{j,\bar{\sigma}}n_{j,\bar{\sigma}'}c^{\dagger}_{j,\sigma'}c_{i,\sigma'}. \tag{2.12}$$

where $J = 4t^2/U$, called the superexchange coupling, is the energy scale associated with the virtual hopping fluctuations. Here, $n_{i,\sigma}$ is the number operator of spin σ on site i and $\bar{\sigma}$ is the complement of σ. We see that creation and annihilation operators acting on the same site appear in pairs in Eq. (2.12), i.e., the atoms are localised and transport is not possible. Indeed, the only degree of freedom remaining in the effective theory is spin. Defining the spin-1/2 operator for the z-component of the spin $\hat{S}^z_i$ on site i and the spin ladder operators $\hat{S}^{\pm}_i$ as

$$\hat{S}^z_i = \frac{1}{2}\left(c^{\dagger}_{i,\uparrow}c_{i,\uparrow} - c^{\dagger}_{i,\downarrow}c_{i,\downarrow}\right), \tag{2.13}$$

$$\hat{S}^+_i = c^{\dagger}_{i,\uparrow}c_{i,\downarrow}, \tag{2.14}$$

$$\hat{S}^-_i = c^{\dagger}_{i,\downarrow}c_{i,\uparrow}, \tag{2.15}$$

we can rewrite Eq. (2.12) up to an additive constant as the Heisenberg Hamiltonian

$$H_{\text{eff}} = \frac{J}{2} \sum_{\langle i,j \rangle} \hat{\mathbf{S}}_i \cdot \hat{\mathbf{S}}_j. \tag{2.16}$$

There is a simple heuristic way of understanding Eq. (2.16) in terms of two neighbouring sites. If U is large, we can treat the tunneling part of the Hubbard Hamiltonian as a perturbation. A superexchange interaction then consists of a hop to a neighbouring site and back again, which leads to an energy contribution proportional to t^2/U in second-order perturbation theory. The sign of the interaction can be understood from the Pauli principle which forbids superexchange fluctuations if the spins are parallel, and the fact that the fluctuation leads to an energy gain for repulsive interactions.

For the positive-U Hubbard model of interest here, $J > 0$ and the system can gain energy by anti-aligning spins. This shows that the ground state is an antiferromagnetically ordered or *Néel* state. An explicit scheme for achieving the Néel state in an optical lattice is developed in chapter 3, and we illustrate this scheme in Fig. 2.2. Although realistic experiments are performed with a harmonic trapping potential on top of the optical lattice, the trap has no effect on the Mott insulator other than placing a limit on the number of particles, as explained in Appendix B.

2.3 The imbalanced Heisenberg and Ising models

The question of what will occur in the imbalanced situation, namely, when there is an excess of one spin species of fermions in the system, is discussed in detail in chapter 4. Here, we derive the free energy for this system, then illustrate the calculation of the phase diagram with the analytically solvable simpler case of the Ising model.

Imbalance gives rise to a net magnetisation in the system. Therefore, a natural choice of Cartesian coordinate system is then one with the z-axis aligned to the magnetisation vector $\mathbf{m} = (0, 0, m_z)$, where

$$m_z = \frac{1}{2} \frac{N_\uparrow - N_\downarrow}{N_\uparrow + N_\downarrow} \tag{2.17}$$

for spin-1/2 fermions and $N_{\uparrow(\downarrow)}$ is the number of $\uparrow$ ($\downarrow$) species of fermions in the system. Since we expect the spins of the system to align

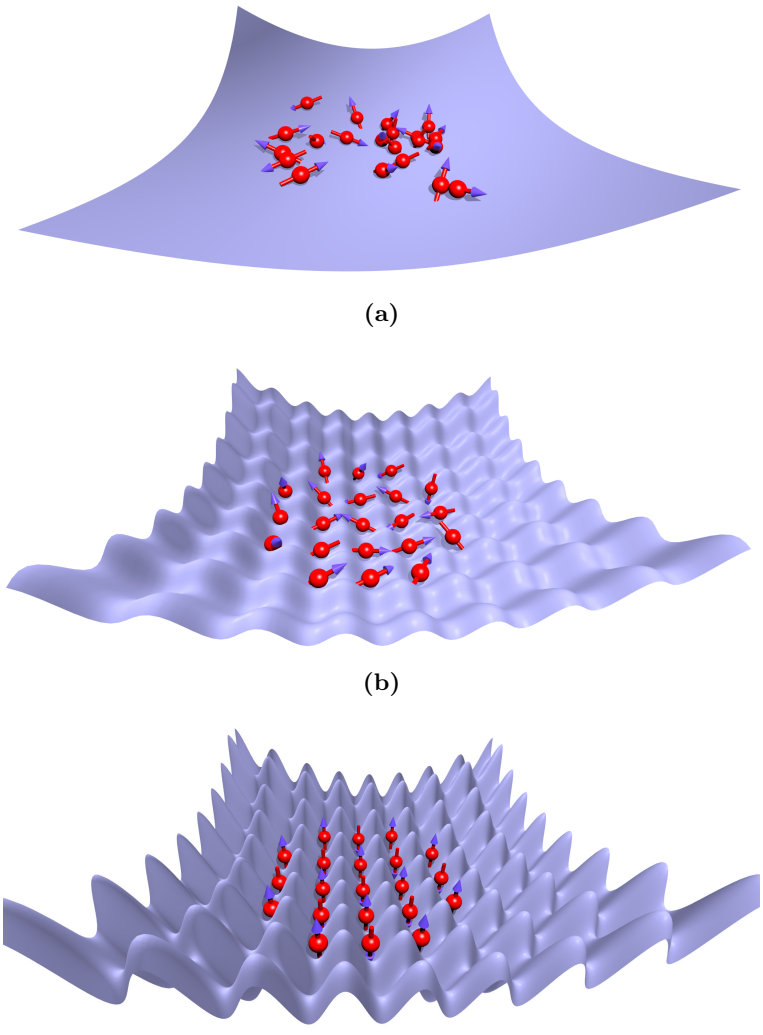

(a)

(b)

(c)

Figure 2.2: Cooling into the Néel state. **(a)** We start with a gas of ultracold fermionic atoms confined to a harmonically trap, depicted here by the blue sheet. **(b)** Adiabatically introducing a periodic potential places the system in the Mott insulator state. **(c)** The Néel state is achieved by further adiabatically ramping up the lattice potential.

with this magnetisation on average, we augment the Heisenberg Hamiltonian in Eq. (2.16) by introducing a Lagrange multiplier $\mathbf{B}$ to enforce this constraint. The Hamiltonian of the system is then

$$H = \frac{J}{2}\sum_{\langle i,j\rangle} \hat{\mathbf{S}}_i \cdot \hat{\mathbf{S}}_j - \sum_i \mathbf{B}\cdot(\hat{\mathbf{S}}_i - \mathbf{m}). \tag{2.18}$$

For $J > 0$ the spins in the ground state are anti-aligned, and the lattice sites can be grouped according to the average orientation of their spins into two sublattices, which we label A and B. By writing the spin operators on sublattice A (B) as their expectation value plus a small fluctuation $\hat{\mathbf{S}}_i^{A\,(B)} = \langle \hat{\mathbf{S}}^{A\,(B)}\rangle + \delta\hat{\mathbf{S}}_i^{A\,(B)}$, we expand the Hamiltonian to quadratic order in the fluctuations to obtain the mean-field Hamiltonian,

$$\begin{aligned} H_{\mathrm{MF}} &= \frac{J}{2}\sum_{\langle i,j\rangle}(\langle\hat{\mathbf{S}}^A\rangle + \delta\hat{\mathbf{S}}_i^A)\cdot(\langle\hat{\mathbf{S}}^B\rangle + \delta\hat{\mathbf{S}}_j^B) - \sum_i \mathbf{B}\cdot(\hat{\mathbf{S}}_i - \mathbf{m}) \\ &= -\frac{Jz}{2}N\langle\hat{\mathbf{S}}^A\rangle\cdot\langle\hat{\mathbf{S}}^B\rangle + N\mathbf{m}\cdot\mathbf{B} \\ &\qquad + \sum_{i\in A}\Big(Jz\langle\hat{\mathbf{S}}^B\rangle - \mathbf{B}\Big)\cdot\hat{\mathbf{S}}_i^A + \sum_{i\in B}\Big(Jz\langle\hat{\mathbf{S}}^A\rangle - \mathbf{B}\Big)\cdot\hat{\mathbf{S}}_i^B \\ &= -\frac{JzN}{2}(\mathbf{m}^2 - \mathbf{n}^2) - \sum_{i\in A}\mathbf{B}^A\cdot\hat{\mathbf{S}}_i^A - \sum_{i\in B}\mathbf{B}^B\cdot\hat{\mathbf{S}}_i^B + N\mathbf{m}\cdot\mathbf{B}. \end{aligned} \tag{2.19}$$

where $N = N_\uparrow + N_\downarrow$. Here, the total magnetisation $\mathbf{m}$ and the Néel vector or *staggered magnetisation* $\mathbf{n}$ are related to the average spin on the sublattices by

$$\mathbf{m} = \frac{\langle\hat{\mathbf{S}}^A\rangle + \langle\hat{\mathbf{S}}^B\rangle}{2} \tag{2.20}$$

$$\mathbf{n} = \frac{\langle\hat{\mathbf{S}}^A\rangle - \langle\hat{\mathbf{S}}^B\rangle}{2}. \tag{2.21}$$

The effective magnetic field is $\mathbf{B}_{A\,(B)} = \mathbf{B} - Jz\mathbf{m} \pm Jz\mathbf{n}$ where we take the upper (lower) sign for the A (B) sublattice. There are two energy eigenvalues at each site given by

$$\varepsilon^{\pm}_{i\in A\,(B)} = -\frac{Jz}{2}(\mathbf{m}^2 - \mathbf{n}^2) + \mathbf{m}\cdot\mathbf{B} \pm \frac{1}{2}\mathbf{B}_{A\,(B)}. \tag{2.22}$$

The total partition function then becomes a product of single-site partition functions

$$\begin{aligned} Z &= \prod_i \left(e^{-\beta\varepsilon_i^+} + e^{-\beta\varepsilon_i^-} \right) \\ &= 4\exp\left(N\beta \frac{JzN}{2}(\mathbf{m}^2 - \mathbf{n}^2) + N\mathbf{m}\cdot\mathbf{B} \right) \\ &\qquad \times \left[\cosh\left(\frac{\beta}{2}|\mathbf{B}_A| \right) \cosh\left(\frac{\beta}{2}|\mathbf{B}_B| \right) \right]^{N/2}. \end{aligned} \tag{2.23}$$

Here, $\beta = 1/k_B T$ where T is the temperature and k_B is Boltzmann's constant. The on-site free energy is then found from $Z = e^{-N\beta f}$. To find the Lagrange multiplier, we note that the gradient of the partition function with respect to the Lagrange multiplier is

$$\nabla_{\mathbf{B}} Z = \nabla_{\mathbf{B}} e^{-N\beta f} = -N\beta Z \nabla_{\mathbf{B}} f \tag{2.24}$$

which can also be written as

$$\nabla_{\mathbf{B}} Z = \nabla_{\mathbf{B}} \ \mathrm{Tr}\ e^{-\beta H_{\mathrm{MF}}} = \frac{N}{2}\beta \left(\langle \hat{\mathbf{S}}^A \rangle + \langle \hat{\mathbf{S}}^B \rangle - 2\mathbf{m} \right) Z = 0. \tag{2.25}$$

Comparing Eqs. (2.24) and (2.25) we obtain $\nabla_{\mathbf{B}} f = 0$ which is the usual equation for the Lagrange multiplier. The Néel vector can be found by minimising the free energy subject to this constraint, and in this way we find that it is always perpendicular to $\mathbf{m}$ below the critical temperature. At the onset of antiferromagnetic order where $|\mathbf{n}|$ is very small, the constraint and the free energy are well approximated by their power series in $|\mathbf{n}|$. As we illustrate below for the special case of the Ising model, this allows us to find an analytic expression for the critical temperature.

A simplified model is obtained if we restrict the spin degrees of freedom from $SU(2)$ to Z_2 by requiring the spins to point only in the positive or negative z-direction. Then, all vectors are aligned to the z-axis and the Heisenberg model reduces to the Ising model. The free energy of the imbalanced Ising model is

$$\begin{aligned} f &= \frac{Jz}{2}\left(n^2 - m^2\right) + Bm \\ &\quad - \frac{1}{2\beta} \ln\left[4\cosh\left(\frac{\beta}{2}(B - Jmz - Jnz) \right) \cosh\left(\frac{\beta}{2}(B - Jmz + Jnz) \right) \right] \end{aligned} \tag{2.26}$$

with the constraint

$$m = \frac{1}{4}\tanh\left(\frac{\beta}{2}(B - Jmz - Jnz)\right) + \frac{1}{4}\tanh\left(\frac{\beta}{2}(B - Jmz + Jnz)\right). \tag{2.27}$$

To find the critical temperature where n becomes nonzero, we perform a small n expansion of the free energy and constraint. Substituting $B = B_0 + B_2 n^2 + \cdots$ into the constraint, expanding to quadratic order in n and solving order by order, we obtain

$$B_0 = Jzm + \frac{2}{\beta}\operatorname{arctanh}(2m), \tag{2.28}$$

and $B_2 = J^2 z^2 m\beta$. Thus the Lagrange multiplier near the critical temperature is

$$B = \frac{2}{\beta}\operatorname{arctanh}(2m) + Jzm(1 + Jzn^2\beta) + \mathcal{O}(n^4). \tag{2.29}$$

Note that we have no odd powers of n in the expansions as the system is symmetric under the transformation $n \to -n$, which is equivalent to interchanging the sublattices. Substituting Eq. (2.29) into the free energy and expanding to second order in n, an expression for the critical temperature is obtained by solving $\partial^2 f / \partial n^2 = 0$. In this case,

$$T_c = \frac{Jz}{4k_B}(1 - 4m^2), \tag{2.30}$$

and the resulting phase diagram is the dashed line in Fig. 4.1(a).

Notes

1. The height of the potential V_0 is related to laser parameters and properties of the alkali atoms of interest here. Neglecting finite-lifetime effects, it is given by

$$V_0 = \frac{(\hbar\Omega)^2}{3}\left(\frac{1}{\hbar\omega - E_{D_1}} - \frac{1}{\hbar\omega + E_{D_1}} + \frac{2}{\hbar\omega - E_{D_2}} - \frac{2}{\hbar\omega + E_{D_2}}\right) \tag{2.31}$$

where Ω is the Rabi frequency of the atom and $\omega = 2\pi c/\lambda$. Here λ is the wavelength of the lattice lasers and c is the speed of light. E_{D_1} (E_{D_2}) is energy in excess of the ground state for the D_1 (D_2) optical transition. When the laser light frequency is far from the frequency of the optical transition, we may take $E_{D_1} \simeq E_{D_2}$ thereby neglecting fine-structure effects, and the height of the lattice

may be written as $V_0 = \Omega^2/\delta$, where $\delta = \omega - (E_e - E_g)/\hbar$ is the detuning of the laser, and E_g and E_e is the energy of the ground state and excited state, respectively. See Ref. [69] for an *ab initio* derivation.

2. The compressibility $C_n = (1/n^2)\partial n/\partial\mu$ here refers to the change in the number of atoms per unit cell n as a function of the chemical potential μ. This differs from the more common definition from the kinetic theory of gases $C_V = -(1/V)\,\partial V/\,\partial p$, which measures the change of volume V of a system as a function of pressure p. A central property of Mott insulators is that C_n vanishes exponentially for small temperatures, which allows the Mott insulator to be distinguished from other insulators such as an Anderson insulator of noninteracting particles in the presence of strong disorder.

3

Achieving the Néel state in an optical lattice

We theoretically study the possibility of reaching the antiferromagnetic phase of the Hubbard model by starting from a normal gas of trapped fermionic atoms and adiabatically ramping up an optical lattice. Requirements on the initial temperature and the number of atoms are determined for a three dimensional square lattice by evaluating the Néel state entropy, taking into account fluctuations around the mean-field solution. We find that these fluctuations place important limitations on adiabatically reaching the Néel state.

3.1 Introduction

An optical lattice is a regular periodic potential for neutral cold atoms [42] which enables the controlled experimental exploration of paradigmatic ideas and models from condensed-matter physics. This is because cold atomic gases generally allow for a great deal of experimental tunability. For example, Feshbach scattering resonances allow for the interaction strength to be experimentally varied over a considerable range [33,34]. Other quantities that may be altered include temperature, density, and strength and shape of the trapping potential. In particular, an optical-lattice potential plays the role of the ion-lattice potential encountered in electronic solid-state physics. The energy bands resulting from this periodic potential lead

This chapter has been previously published as *Achieving the Néel state in an optical lattice*, Arnaud Koetsier, R. A. Duine, Immanuel Bloch, and H. T. C. Stoof, Phys. Rev. A **77,** 023623 (2008).

to a quenching of the kinetic energy of the atoms with respect to their interaction energy, enabling the exploration of strongly-correlated phases that play a significant role in condensed-matter physics.

An important model that can be studied experimentally with cold atoms is the single-band Hubbard model, which consists of interacting fermions in the tight-binding approximation. The Hubbard Hamiltonian is realized by cold atoms in an optical lattice when the potential is strong enough so that only the lowest-energy band is populated [46]. For bosonic atoms one then commonly refers to this model as the Bose-Hubbard model. The theoretically predicted Mott-insulator-to-superfluid phase transition [47] for this model has indeed been observed experimentally [48].

The fermionic Hubbard model, referred to simply as the Hubbard model, is important in the context of high-temperature superconductivity [43, 44] and has also been realized with cold atoms [70]. At half filling, corresponding to one particle per lattice site, the ground state of this model is antiferromagnetic, i.e., a Néel-ordered state, for strong enough on-site interactions. As the filling factor is reduced by doping, the system is conjectured to undergo a quantum phase transition to a d-wave superconducting state [71]. A theoretical proof of the existence of d-wave superconductivity in the Hubbard model is still lacking and would be a major step towards understanding the superconducting state of the cuprates. With the recent experimental advances in the field of ultracold atoms, an experimental exploration of this issue is within reach.

In view of this motivation, a significant problem is determining how the Néel state of the Hubbard model can be reached experimentally. In this paper, we study theoretically the process of adiabatically turning on the optical lattice [72, 73], with the goal of determining the conditions required for an initially trapped balanced two-component Fermi gas with repulsive interactions to reach the Néel state in the lattice. Experimentally, the presence of antiferromagnetic order in this cold-atom experiment can be subsequently detected from shot-noise correlations in the density distribution [74, 75].

Our results are summarized in Fig. 3.1. For initial temperatures lower than T_{F}, the Fermi temperature in the trap, the entropy per particle in the trap depends linearly on temperature as is shown by the dashed line. The optical lattice is then turned on adiabatically and to determine the final temperature of the gas we need the entropy per atom in the lattice. For a sufficiently smooth trapping potential such that the tunneling does not

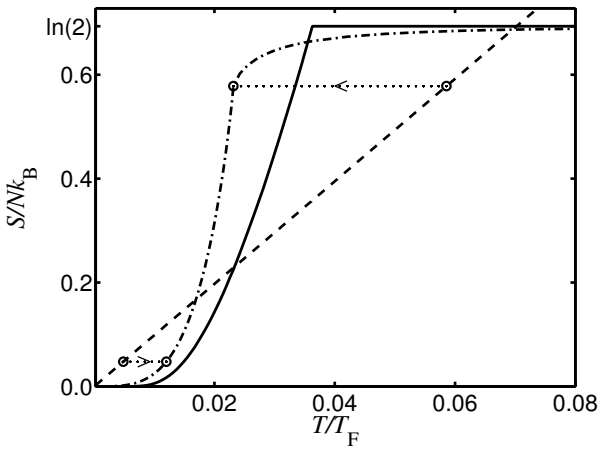

Figure 3.1: The entropy per particle in the harmonic trapping potential only (dashed line), in a lattice of depth $V_0 = 6.5E_R$ (E_R is the recoil energy) from single-site mean-field theory (solid curve) and with fluctuations (dashed-dotted curve), where T_F is the Fermi temperature in the trap. The horizontal dotted lines illustrate cooling and heating into the Néel state at constant entropy by starting in the harmonic trap and adiabatically turning on the lattice.

become site-dependent, the only effect of the trap is to place a restriction on the total number of particles which we discuss later and, other than this, we may neglect the trap for calculations in the lattice. Since we consider balanced gases here, we will at sufficiently low temperatures first enter the Mott phase with one particle per site, and the subsequent evolution of the gas is then described by the Heisenberg model for the spins alone. The result from the usual mean-field theory is shown for a lattice depth of $6.5E_R$ (where E_R is the recoil energy) by the black curve, and is equal to $k_B \ln(2)$ everywhere above the critical temperature T_c. Since entropy is conserved in adiabatic processes, the final temperature is simply the temperature at which the final entropy in the lattice equals the initial entropy in the trap. Two such processes are shown by the dotted lines for different initial temperatures demonstrating that the gas is sometimes heated and not cooled by the lattice. Nevertheless, mean-field theory leads to the intuitive result that as long as the entropy per particle in the initial state is less than $k_B \ln(2)$, which is the maximum entropy of the Heisenberg model, the Néel state is always reached by adiabatically turning on the optical lattice.

The inclusion of fluctuations leads however to a more restrictive condi-

tion. To probe the effect of fluctuations, we present an improved mean-field theory which produces a temperature-dependent entropy above T_c, as seen from the inset of Fig. 3.2. Although this approach is exact at high temperatures, it fails to account for spin waves present at low temperatures and for critical phenomena near T_c. By further extending the improved mean-field theory to reproduce the correct critical and low temperature behaviour due to fluctuations, we are able to determine the entropy in the lattice for all temperatures (dashed-dotted curve in Fig. 3.1). In particular, we find that fluctuations lower the entropy of the atoms in the square lattice at T_c as

$$S(T = T_c) \simeq N k_{\mathrm{B}} \ln(2) - \frac{3NJ^2}{32 k_{\mathrm{B}} T_c^2 (3\nu - 1)} , \tag{3.1}$$

where ν is the critical exponent of the correlation length ξ. For the case of three dimensions, $\nu = 0.63$ [76]. As a result, the initial temperature required to reach the Néel state is more than 20% lower than that found from the usual mean-field theory, but fortunately remains experimentally accessible. For example, with ^{40}K atoms and a final lattice depth of $8E_{\mathrm{R}}$ the Néel state is achieved when the final temperature in the lattice is $0.012T_{\mathrm{F}}$, which can be obtained with an initial temperature of $0.059T_{\mathrm{F}}$.

3.2 Single-site mean-field theory

The Hamiltonian for the Hubbard model is given by

$$H = -t \sum_{\sigma} \sum_{\langle jj' \rangle} c^{\dagger}_{j,\sigma} c_{j',\sigma} + U \sum_{j} c^{\dagger}_{j,\uparrow} c^{\dagger}_{j,\downarrow} c_{j,\downarrow} c_{j,\uparrow} , \tag{3.2}$$

in terms of fermionic creation and annihilation operators, denoted by $c^{\dagger}_{j,\sigma}$ and $c_{j,\sigma}$, respectively, where σ labels the two hyperfine spin states $|\uparrow\rangle$ or $|\downarrow\rangle$ of the atoms. In the first term of this expression, the sum over lattice sites labeled by indices j and j' is over nearest neighbours only and proportional to the hopping amplitude given by

$$t = \frac{4E^{\mathrm{R}}}{\sqrt{\pi}} \left(\frac{V_0}{E^{\mathrm{R}}} \right)^{\frac{3}{4}} e^{-2\sqrt{V_0/E^{\mathrm{R}}}}. \tag{3.3}$$

Here, $V_0 > 0$ is the depth of the optical lattice potential defined by

$$V(\mathbf{x}) = V_0[\cos^2(2\pi x/\lambda) + \cos^2(2\pi y/\lambda) + \cos^2(2\pi z/\lambda)], \tag{3.4}$$

where λ is the wavelength of the lattice lasers. The second term in the Hamiltonian corresponds to an on-site interaction of the strength given in the harmonic approximation by

$$U = 4\pi a \sqrt{\frac{\hbar}{\lambda^3}} \left(\frac{8V_0^3}{m} \right)^{\frac{1}{4}} , \tag{3.5}$$

where a is the s-wave scattering length which is equal to $174a_0$ for ^{40}K. It is well-known [77] that at half filling and in the limit that $U \gg t$ the ground state of the Hubbard model is antiferromagnetic and that, for $k_{\mathrm{B}}T \ll U$, its low-lying excitations are described by the effective Heisenberg Hamiltonian

$$H = \frac{J}{2} \sum_{\langle jk \rangle} \mathbf{S}_j \cdot \mathbf{S}_k , \tag{3.6}$$

with $\mathbf{S}$ being one half times the vector of Pauli matrices. The exchange constant $J = 4t^2/U$ arises from the superexchange mechanism. That is, the system can lower its energy by virtual nearest-neighbour hops only when there is antiferromagnetic ordering.

Within the usual mean-field analysis of the effective Hamiltonian in Eq. (3.6), the total entropy for N atoms in the optical lattice is given by

$$S = -\frac{\partial F_{\mathrm{L}}(\langle \mathbf{n} \rangle)}{\partial T} , \tag{3.7}$$

where F_{L} is the Landau free energy,

$$F_{\mathrm{L}}(\mathbf{n}) = N \left\{ \frac{zJ|\mathbf{n}|^2}{2} - k_{\mathrm{B}}T \ln \left[2 \cosh \left(\frac{zJ|\mathbf{n}|}{k_{\mathrm{B}}T} \right) \right] \right\} , \tag{3.8}$$

in terms of the staggered, or Néel, order parameter $\mathbf{n} = (-)^j \langle \mathbf{S}_j \rangle$ for the phase transition to the antiferromagnetic state. In the expression for the free energy, $z = 6$ is the number of nearest neighbours for a three-dimensional simple square lattice on which we focus here, $k_{\mathrm{B}}T$ is the thermal energy, and $\langle \mathbf{n} \rangle$ is the equilibrium value of the order parameter determined from

$$\left. \frac{\partial F_{\mathrm{L}}(\mathbf{n})}{\partial \mathbf{n}} \right|_{\mathbf{n}=\langle \mathbf{n} \rangle} = 0 . \tag{3.9}$$

It is nonzero below a critical temperature $k_{\mathrm{B}}T_c = Jz/4 = (3/2)J$. After solving Eq. (3.9) the entropy is determined using Eq. (3.7). The results for

S and $\langle \mathbf{n} \rangle$ obtained in this way are plotted as solid black curves in Figs. 3.1 and 3.2.

The entropy $S_{\rm FG}$ of the initial normal state before ramping up the optical lattice is the entropy of a trapped ideal Fermi gas. It is most conveniently determined from the grand potential

$$\Omega(\mu, T) = -k_{\rm B} T \int_0^\infty d\epsilon \rho(\epsilon) \ln \left[1 + e^{-(\epsilon - \mu)/k_{\rm B} T} \right] , \qquad (3.10)$$

where μ is the chemical potential, and the effect of the harmonic trapping potential with the effectively isotropic frequency $\omega = (\omega_x \omega_y \omega_z)^{1/3}$ is incorporated via the density of states $\rho(\epsilon) = \epsilon^2/(\hbar\omega)^3$ of the atoms. The entropy at fixed total particle number $N(\mu) = -\partial\Omega/\partial\mu$ is then given by $S_{\rm FG} = -\partial\Omega/\partial T|_{\mu(N)}$. At temperatures much lower than the Fermi temperature in the trap, given by $T_{\rm F} = (3N)^{1/3}\hbar\omega/k_{\rm B}$, we find in this manner that [78] $S_{\rm FG} = N k_{\rm B} \pi^2 T/T_{\rm F}$. Now, by equating the final and initial entropies we calculate the temperature of the Heisenberg spin system that results after adiabatically turning on the optical lattice, in terms of the initial temperature of the trapped Fermi gas.

From the expression for the free energy, Eq. (3.8) we immediately see that $S = N k_{\rm B} \ln(2)$ for all temperatures $T > T_c$, as was shown in Fig. 3.1. Although this is the correct high-temperature limit of the entropy, temperature dependence will lower the entropy at T_c and therefore lower the initial temperature required to achieve the Néel state. To obtain the temperature dependence above T_c, we must thus go beyond single-site mean-field theory to include fluctuations. The simplest such model described below incorporates the interaction of a given site with one of its neighbours exactly and treats interactions with the rest of the neighbours within mean-field theory.

3.3 Two-site mean-field theory

The two-site Hamiltonian for neighbouring sites labeled "1" and "2" is given by

$$H = J \mathbf{S}_1 \cdot \mathbf{S}_2 + J(z-1)|\mathbf{n}|(\mathbf{S}_1^z - \mathbf{S}_2^z) + J(z-1)|\mathbf{n}|^2 , \qquad (3.11)$$

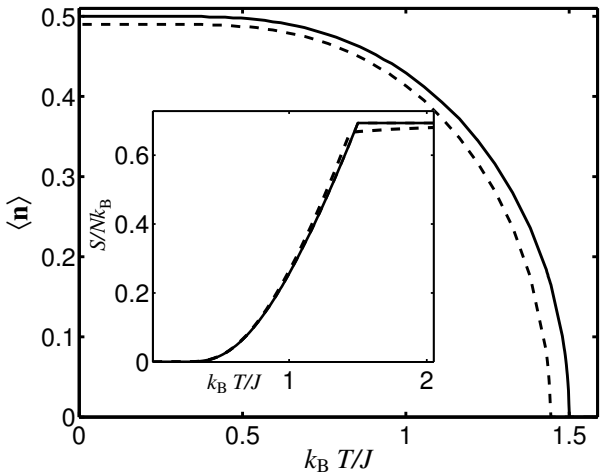

Figure 3.2: The staggered magnetization $\langle \mathbf{n} \rangle$ of the single (solid curves) and two-site (dashed curves) mean-field theories, the latter of which shows depletion at $T = 0$ and a lowering in T_c. The entropy of both theories is plotted in the inset. Above T_c we see that the entropy of the two-site theory is temperature dependent.

where the last term is a correction to avoid double counting of mean-field effects. Diagonalizing this Hamiltonian we obtain the free energy

$$F_{\mathrm{L}}(\mathbf{n}) = N\left\{\frac{1}{2}(z-1)J|\mathbf{n}|^2 - \frac{1}{2\beta}\ln\left[2e^{-\beta J/4} + 2e^{\beta J/4}\cosh\left(\frac{\beta J}{2}\sqrt{1+4(z-1)^2|\mathbf{n}|^2}\right)\right]\right\}, \quad (3.12)$$

and find the entropy from Eq. (3.7) with the condition Eq. (3.9) as in the single-site model. The results are plotted in Fig. 3.2, where we see that fluctuations lower the critical temperature and also bring about a 2% depletion of the order parameter which is now less than 0.5 near $T = 0$.

The two-site result carries the exact $1/T^2$ dependence of the entropy of the Heisenberg model at high temperatures. Near $T = 0$, however, the entropy is still exponentially suppressed reflecting the energy cost of flipping a spin. This exponential suppression is an artefact of the mean-field approximation that ignores the Goldstone modes which are present in the symmetry-broken phase. Furthermore, critical behaviour cannot be properly accounted for by a one-, two- or higher-site model since, near

the onset of Néel order, critical fluctuations extend throughout the entire lattice so one would in principle need to include all sites exactly. To overcome these shortcomings, we extend our two-site model below to all temperatures.

3.4 Fluctuations

The two-site mean-field theory produces the correct normal-state entropy behaviour in the high-temperature limit,

$$S(T \gg T_c) = Nk_{\mathrm{B}} \left[\ln(2) - \frac{3J^2}{64k_{\mathrm{B}}^2 T^2} \right] . \tag{3.13}$$

In the low-temperature regime, the entropy is determined from spin-wave fluctuations prevalent near $T = 0$ which give a black-body-like entropy,

$$S(T \ll T_c) = Nk_{\mathrm{B}} \frac{4\pi^2}{45} \left(\frac{k_{\mathrm{B}} T}{2\sqrt{3} J \langle \mathbf{n} \rangle} \right)^3 . \tag{3.14}$$

The continuous interpolation between these two regimes has the additional constraint that, near T_c, we should obtain the correct critical behaviour of the antiferromagnet, namely, the correct universal ratio of the amplitudes above and below the phase transition A^+/A^- and correct critical exponent $d\nu - 1$ where

$$S(T \simeq T_c) = S(T_c) \pm A^{\pm} |t|^{d\nu - 1}, \quad t = (T - T_c)/T_c \to 0^{\pm} . \tag{3.15}$$

This follows from the fact that the singular part of the free energy density behaves as $F^{\pm}/\xi^d$, where the correlation length diverges like $\xi \sim |t|^{-\nu}$ as $t \to 0$. Explicit expressions for the entropy embodying the correct behaviour in the low-, high- and critical temperature regimes are presented in Appendix A, and plotted as the dashed-dotted curve in Fig. 3.1 for $d = 3$ using $A^+/A^- \simeq 0.54$ and $\nu = 0.63$ [76], and the Néel temperature of $T_c = 0.957 J/k_{\mathrm{B}}$ [79]. Their value at T_c leads to the central result of this paper, namely, Eq. (3.1) which specifies the initial entropy required to reach the Néel state.

3.5 Discussion and Conclusions

As briefly mentioned earlier, there is a limit on the total number of atoms in the trap, beyond which at low temperatures it is energetically more

favourable to doubly occupy sites in the centre of the trap, thereby destroying the antiferromagnetic state, rather than singly occupying outlying sites where the trap potential is larger than U. Thus, insisting that the system end up in the Mott-insulator state with one particle per site entails the upper bound, $N \leqslant N_{\max} = (4\pi/3)(8U/m\omega^2\lambda^2)^{3/2}$, where m is the mass of the atoms and λ is the wavelength of the lattice lasers. This point is illustrated in appendix B. For ^{40}K atoms in a lattice with a wavelength $\lambda = 755$ nm and depth $8E_{\rm R}$, and with a harmonic trap frequency $\omega/2\pi = 50$ Hz, $N_{\max} \simeq 2 \times 10^6$ which is well above the typical number of atoms in experiments.

We have also attempted to determine the effect that fluctuations have on the entropy in a more microscopic manner by studying Gaussian fluctuations about the mean-field $\langle \mathbf{n} \rangle$ for the single-site mean-field theory in the low-temperature regime. But such a random-phase approximation has severe complications related to the fact that $\langle \mathbf{n} \rangle$ enters in the magnon dispersion as $\omega_{\mathbf{k}}^{\rm M} \propto \langle |\mathbf{n}| \rangle |\mathbf{k}|$. Hence, as can be already seen from Eq. (3.14), the contribution of the magnons to the entropy diverges when $\langle \mathbf{n} \rangle \to 0$ near T_c. One way to potentially resolve this issue is to start from the Hubbard Hamiltonian Eq. (3.2) directly but such an analysis is involved [80] and has yet to be carried out.

In the above, we have focused on the $d = 3$ case. Whilst our results can easily be extended to the $d = 2$ case, a more pertinent way to reach the two-dimensional antiferromagnet most relevant to high-temperature superconductors, would be to adiabatically prepare a three-dimensional Néel state, as explained in this paper, and then decrease the tunneling in one direction by changing the intensity of one of the lattice lasers. In this way, the three-dimensional system is changed into a stack of pancakes of atoms in the two-dimensional Néel state. Furthermore, studying doped optical lattices made by introducing a small imbalance in the initial state may shed some light on the physics of high-temperature superconductors and would be an exciting direction for future research.

Acknowledgements

We would like to thank Gerard Barkema, Dries van Oosten and Randy Hulet for helpful discussions. This work is supported by the Stichting voor Fundamenteel Onderzoek der Materie (FOM), the Nederlandse Organisatie voor Wetenschaplijk Onderzoek (NWO), and the Deutsche Forschungsgemeinschaft (DFG).

4

The imbalanced antiferromagnet in an optical lattice

Quantum magnetism is a new direction of research in ultracold atomic physics. Neutral atoms confined in a periodic potential created with standing waves of light, known as an optical lattice, can be used to realise the so-called Hubbard model that is of great importance for high-temperature superconductivity. Achieving the antiferromagnetic ground state of this model in a gas of fermionic atoms is currently a major experimental goal. Another prominent topic that has been the focus of a number of recent ground-breaking experiments is imbalance in two-component Fermi gases [49, 50]. There, the population of each spin species can be controlled permitting the exploration of uncharted imbalanced phases of great interest in condensed-matter, nuclear, high-energy, and astroparticle physics [20–23]. For example, an imbalanced quark-gluon plasma is conjectured to occur in the core of neutron stars [81, 82]. Here we explore the bridge between these two exciting directions in the physics of ultracold atomic gases and study the rich properties of an imbalanced antiferromagnet in an optical lattice. We present its phase diagram, discuss spin waves and explore the emergence of topological excitations, known as merons, which are responsible for a Kosterlitz-Thouless transition that has never unambiguously been observed.

This chapter has been submitted for publication in Nature Phys. as *The imbalanced antiferromagnet in an optical lattice*, Arnaud Koetsier, F. van Liere, and H. T. C. Stoof (2009).

4.1 Introduction

Owing to their exquisite experimental tunability, ultracold atomic gases have become a test bed for many paradigmatic ideas in quantum many-body physics. In particular, ultracold atoms trapped in an optical lattice, i.e., a periodic potential for neutral atoms created by orthogonal retroreflected laser beams [42], are accurately described by the Hubbard model. The narrow energy bands resulting from the periodic potential quench the kinetic energy of the atoms with respect to their interaction energy, enabling the exploration of strongly correlated phases that play a significant role in condensed-matter physics. The single-band Hubbard model is realised by cold atoms when the lattice potential is sufficiently strong that only the lowest-energy band is populated [46]. At a filling corresponding to one particle per lattice site, this model has a Mott-insulator phase for repulsive interactions, and in an atomic Bose gas the theoretically predicted superfluid-to-Mott-insulator phase transition [47] has indeed been observed experimentally [48]. For bosons, one commonly refers to this model as the Bose-Hubbard model. The Fermi-Hubbard model, referred to simply as the Hubbard model, has also been realised experimentally [70], and the fermionic Mott-insulator has only recently been seen [63, 64]. Aside from being rich in novel physics in itself, this system may also shed new light on the still poorly understood phenomenon of high-temperature superconductivity in the cuprates. There, the Hubbard model is believed to describe electrons in the periodic ion-lattice potential of the copper-oxygen planes [43–45] which are believed to undergo a quantum phase transition to a d-wave superconducting state as the filling fraction is reduced by doping [71]. In this case, electrons on the same lattice site repel each other due to the Coulomb interaction. We therefore consider here the repulsive Hubbard model, although the attractive Hubbard model can also be realised and possesses interesting BEC-BCS crossover physics [83]. In the Mott-insulator phase only spin degrees of freedom remain and its low-lying excitations are then effectively described by the Heisenberg model. The three-dimensional phase diagram calculated within mean-field theory for this model is shown in Fig. 4.1 for a cubic lattice which is experimentally most relevant.

In the absence of imbalance, i.e., when there are equal proportions of each spin species, the Mott insulator becomes a pure antiferromagnetic or Néel state below a certain critical temperature and is solely characterised by a nonzero expectation value of the Néel order parameter vector $\mathbf{n}$, also

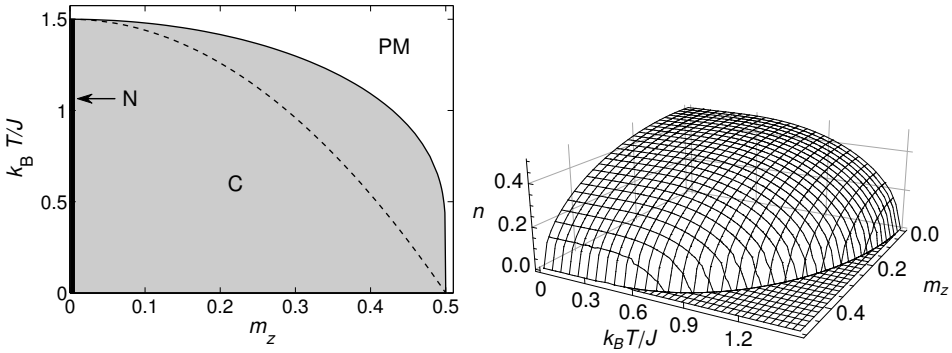

Figure 4.1: Phase diagram of the imbalanced antiferromagnet in three dimensions. (a) The solid curve is the critical temperature $k_B T/J$ for the canted antiferromagnet (C). Above the critical temperature the system is paramagnetic (PM). Here, the imbalance is parameterised by the magnetisation m_z which is equal to the average spin per site of the system, J is the superexchange coupling of the antiferromagnetic Heisenberg model and k_B is the Boltzmann constant. We find that the equilibrium Néel vector $\langle \mathbf{n} \rangle$ is always perpendicular to the magnetisation direction. Also shown is the critical temperature for the corresponding Ising model (dashed line), i.e., when $\mathbf{n}$ is restricted to being parallel with the magnetisation direction. In both cases we retrieve in the absence of imbalance the classical value of the critical temperature in three dimensions $k_B T/J = 3/2$, below which the system is in a pure antiferromagnetic or Néel (N) state. **(b)** The size of the Néel vector $n = |\langle \mathbf{n} \rangle|$ which is nonzero in the antiferromagnetic phase.

known as the staggered magnetisation. Changing the proportion of each spin species gives rise to a nonzero average magnetisation $\mathbf{m} = (0, 0, m_z)$, where $m_z = S(N_\uparrow - N_\downarrow)/(N_\uparrow + N_\downarrow)$. Here, $S = 1/2$ is the atomic pseudospin for the two-component Fermi mixture of interest, and $N_{\uparrow,\downarrow}$ denotes the number of particles of each spin species. In this imbalanced case, the system has a canted antiferromagnetic phase at low temperatures where the Néel vector is always found to be perpendicular to the magnetisation vector [84]. Imbalance therefore breaks the rotational symmetry of the system and defines an easy plane for the Néel vector that is perpendicular to the average magnetisation direction.

In both the Néel and canted phases the low-energy excitations are spin-density waves called magnons. By linearising the Heisenberg equations of motion of the on-site spin operators, we find that for the balanced situation the magnons have the usual doubly degenerate antiferromagnetic disper-

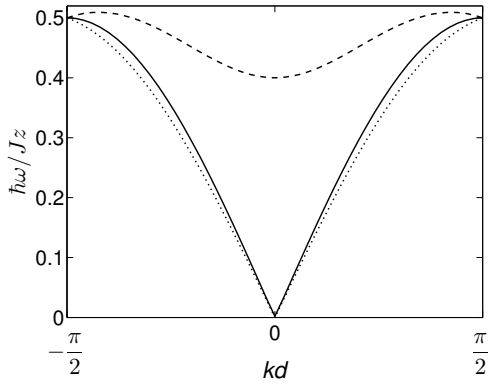

Figure 4.2: The dispersion relation for the spin waves. Here, $\mathbf{k} = k(1, 1, 1)$ is the wave vector and d is the lattice spacing which is equal to half the wavelength of the lattice lasers. For zero magnetisation (solid line), the dispersion is the usual doubly degenerate gapless antiferromagnetic dispersion. The presence of imbalance splits the degeneracy and one of the dispersions (dashed line) becomes quadratic near zero momentum corresponding to a ferromagnetic dispersion and acquires a gap equal to $2Jzm$ with z the number of nearest neighbours, while the other remains antiferromagnetic in nature (dotted line). The imbalanced dispersions shown here are for $m_z = 0.2$.

sion that is linear for small momenta, as shown in Fig. 4.2. However, in the imbalanced case the nonzero average magnetisation lifts this degeneracy. As a result, one of the dispersions becomes gapped corresponding to Larmor precession of the spins around the effective magnetic field generated by the nonzero average magnetisation. The gapped dispersion is quadratic at small momenta signalling the appearance of magnons with a ferromagnetic character.

In experiments the atomic gas is always confined in a trap. However, including a smooth harmonic trapping potential does not lead to inhomogeneities in the Mott-insulator state. Nevertheless, the trap places a limit on the total number of particles beyond which the Mott insulator is destroyed as it becomes energetically favourable to doubly-occupy lattice sites at the centre of the trap rather than singly-occupying empty outlying lattice sites [85]. As a result, the excitation spectrum shown in Fig. 4.2 becomes discretised in the trap due to finite-size effects. In the Mott-insulator phase, the system in a trap is thus essentially homogeneous and we may reasonably neglect the trap here [86].

4.2 Merons

The long-wavelength dynamics obtained above can be summarised by the following non-linear sigma model [87] with an action

$$S[\mathbf{n}(\mathbf{x},t)] = \int \mathrm{d}t \int \frac{\mathrm{d}\mathbf{x}}{d^D} \left\{ \frac{1}{4Jzn^2} \left(\hbar \frac{\partial \mathbf{n}(\mathbf{x},t)}{\partial t} - 2Jz\mathbf{m} \times \mathbf{n}(\mathbf{x},t) \right)^2 - \frac{Jd^2}{2} \left[\nabla \mathbf{n}(\mathbf{x},t) \right]^2 \right\}. \quad (4.1)$$

Here $z = 2D$ is the number of nearest neighbours in the D-dimensional hypercubic lattice, d is the lattice spacing, $\mathbf{m} = (0, 0, m_z)$ is the average magnetisation per site, and $\mathbf{n}(\mathbf{x}, t)$ the local staggered magnetisation at position $\mathbf{x}$ and time t. The equilibrium value of the staggered magnetisation is found from minimising the Landau free energy, given by

$$F[\mathbf{n}(\mathbf{x}), \mathbf{m}] = \int \frac{\mathrm{d}\mathbf{x}}{d^D} \left\{ \frac{Jd^2}{2} \left[\nabla \mathbf{n}(\mathbf{x}) \right]^2 + f[\mathbf{n}(\mathbf{x}), \mathbf{m}] \right\}, \quad (4.2)$$

where $f[\mathbf{n}(\mathbf{x}), \mathbf{m}]$ is the on-site free energy which, as we have seen, breaks the rotational symmetry of the system in the presence of imbalance.

The equation of motion that follows from the non-linear sigma model exhibits long-wavelength spin waves discussed above but also admits a class of topologically stable excitations. In the three dimensional case, these are coreless vortices with a spin component near the location of the vortex line that is out of the easy plane. In the two-dimensional case the topological excitations, known as merons [88, 89], are particularly interesting. Far away from the core of the meron, $\mathbf{n}(\mathbf{x})$ lies in the easy plane perpendicular to the magnetisation and forms a vortex with vorticity of ± 1, while in the core region $\mathbf{n}(\mathbf{x})$ smoothly rotates either up or down out of the easy plane. This spin texture is characterised by two topological invariants, namely, the vorticity and the Pontryagin index which is equal to $\pm 1/2$ depending on the polarity of the core spin [90]. The Pontryagin index does not play an important role for our purposes since, due to the symmetry of the action under the reflection $\mathbf{n} \to -\mathbf{n}$, merons differing only in their Pontryagin index have the same energy. Moreover, the interaction between two merons with a large separation is insensitive to the precise spin configuration in the core. The energy of a single meron diverges logarithmically with the system area A as $(Jn^2\pi/2)\ln(A/\pi\lambda^2)$. Here, $\lambda = dn\sqrt{\pi J/2F_m}$ is the characteristic size of the core, as plotted in Fig. 4.3(b), with F_m the integrated

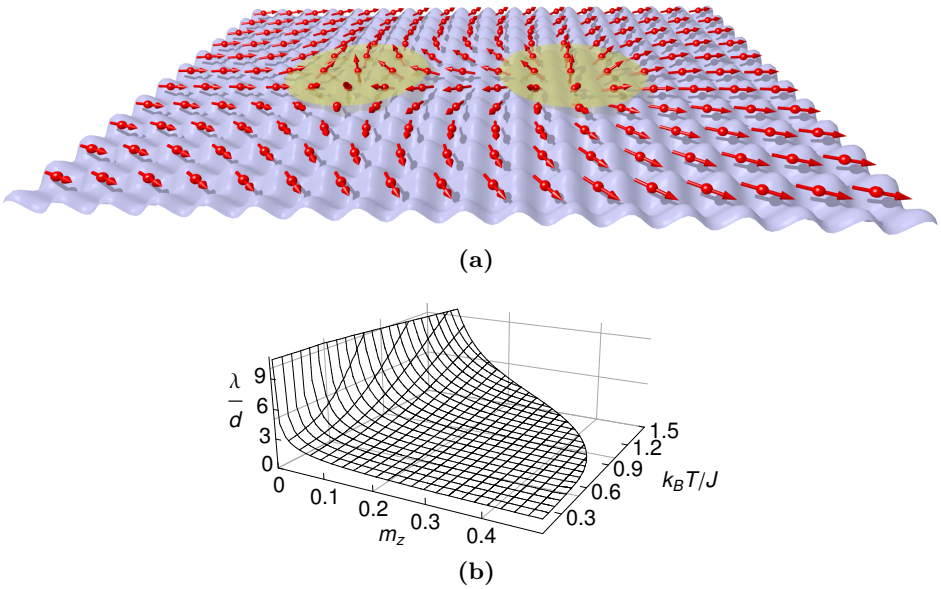

Figure 4.3: Merons in two dimensions. (a) A pair of merons with the same Pontryagin index but opposite vorticities. The arrows indicate the staggered magnetization, the periodic optical lattice potential is shown beneath and the core regions of the merons are shown as yellow discs. **(b)** The radius of the core region λ is plotted as a function of temperature and imbalance. The core size diverges as the imbalance is reduced to zero since full rotational symmetry is then restored and merons no longer exist. The surface terminates at the critical temperature where the system becomes paramagnetic.

on-site free energy required for the formation of a meron spin texture of size $\lambda = d$. Thus, for large system sizes of interest here, it is impossible to thermally excite a single meron below the critical temperature. This behaviour is analogous to the divergence in the kinetic energy of a single vortex in a two-dimensional Bose-Einstein condensate. However, the energy of a pair consisting of a meron together with another meron of opposite vorticity, or antimeron, is finite since the topological deformation of the spin texture cancels far away from the centre of the pair where the Néel vector always points in the same direction, as illustrated in Fig. 4.3(a).

Such meron-antimeron pairs are thermally excited below the critical temperature and are responsible for a Kosterlitz-Thouless phase transition associated with the unbinding of the pairs [91, 92]. Indeed, the entropic

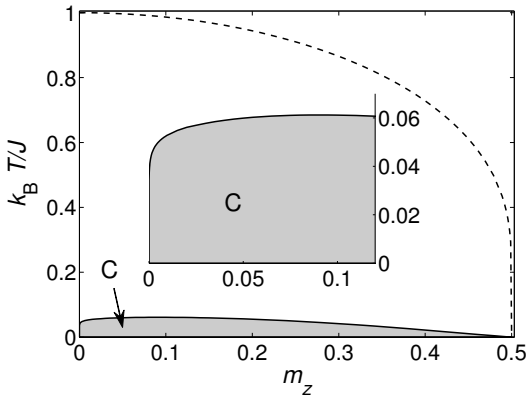

Figure 4.4: Phase diagram of the imbalanced antiferromagnet in two dimensions. The critical temperature for the canted phase (C) is drastically reduced compared to the mean-field result (dashed line) due to fluctuations and becomes a Kosterlitz-Thouless phase transition. Inset: a close-up of the Kosterlitz-Thouless transition for small imbalance, showing that the critical temperature is driven to zero in the absence of imbalance. This is consistent with the Mermin-Wagner theorem for the Heisenberg model in two dimensions [94]. For completeness, we mention here that in one dimension the imbalanced antiferromagnet is paramagnetic at any nonzero temperature [95].

contribution of the merons above the critical temperature is such that the system can lower its free energy through the proliferation of single merons. Topological excitations are notably absent from the mean-field analysis and as a result our mean-field analysis becomes even qualitatively incorrect in two dimensions. To correct for this, we used Monte Carlo results for a similar system [93] to estimate the critical temperature for the Kosterlitz-Thouless transition from the canted antiferromagnet to the paramagnetic phase. We found that this transition occurs at a significantly lower temperature than predicted by mean-field theory in two dimensions, as shown in Fig. 4.4. In particular, the phase transition occurs at zero temperature for the balanced case due to the full rotational symmetry of the system in that case. In three dimensions, however, we do not expect topological excitations or spin waves to significantly alter the phase diagram[1]. Indeed, numerical studies yield only a 36% downward correction of the critical temperature in the balanced case [79].

4.3 Outlook and conclusions

The imbalanced antiferromagnet can be readily investigated experimentally with modern techniques. Imbalance is achieved in an ultracold Fermi gas by driving spin transitions with an RF field, and a Néel-ordered state can be realised by, for example, adiabatically ramping up the optical lattice potential [85]. The Néel character of the imbalanced antiferromagnet can then be probed by the measurement of correlations in atom shot noise [96,97] or using Bragg reflection [98,99] which also enables spin waves to be examined. The unbinding of superfluid vortices in two dimensions has been recently observed in a Bose gas [100]. A similar interference experiment could in principle be performed to detect the Kosterlitz-Thouless phase transition here. Moreover, *in situ* imaging techniques based on scanning electron microscopy have been used to detect single atoms, and could be applied to explore topological and magnon excitations by resolving single lattice sites [101, 102]. Finally, merons possess an internal Ising degree of freedom associated with their Pontryagin index that is very suggestive of their application as a qubit in topological quantum computation, and this is a particularly interesting topic for further investigation.

4.4 Methods

At half filling and for $k_B T \ll U$, with U being the energy cost of adding a second particle to a singly-occupied lattice site, the system is in the Mott-insulator phase and its low-lying excitations are described by the effective antiferromagnetic Heisenberg Hamiltonian [77]. Imbalance in the number of atoms of each spin can be incorporated by means of a constraint, which enforces that the average total spin is equal to the desired magnetisation. Thus, the Hamiltonian of the imbalanced system is

$$\hat{H} = \frac{J}{2} \sum_{\langle i,j \rangle} \hat{\mathbf{S}}_i \cdot \hat{\mathbf{S}}_j - \sum_i \mathbf{B} \cdot (\hat{\mathbf{S}}_i - \mathbf{m}), \tag{4.3}$$

where $\hbar \hat{\mathbf{S}}_i$ is the spin-$\frac{1}{2}$ operator on site i, $\langle i, j \rangle$ denotes a sum over nearest-neighbour sites of the bipartite hypercubic lattice of interest here, and the effective magnetic field $\mathbf{B}$ acts as a Lagrange multiplier. The exchange constant J arises from the superexchange mechanism and is positive. That is, the system can lower its energy by virtual nearest-neighbour hops only when there is antiferromagnetic ordering. Note that the total spin operator

$\sum_i \hat{\mathbf{S}}_i$ commutes with $\hat{H}$ and thus the magnetisation is a constant of the motion.

Within the usual mean-field analysis we obtain the free energy per site

$$f(\mathbf{n},\mathbf{m};\mathbf{B}) = \frac{Jz}{2}(\mathbf{n}^2-\mathbf{m}^2) + \mathbf{m}\cdot\mathbf{B} - \frac{1}{2}k_BT\ln\left[4\cosh\left(\frac{|\mathbf{B}_A|}{2k_BT}\right)\cosh\left(\frac{|\mathbf{B}_B|}{2k_BT}\right)\right], \quad (4.4)$$

where $\mathbf{B}_{A\,(B)} = \mathbf{B} - Jz\mathbf{m} \pm Jz\mathbf{n}$ and we take the upper (lower) sign for the A (B) sublattice, T is the temperature, k_B is the Boltzmann constant, and $\mathbf{n}$ is the staggered magnetisation which is related to the average on-site value of the spin by $\langle\hat{\mathbf{S}}_{A(B)}\rangle = \mathbf{m}\pm\mathbf{n}$. The Lagrange multiplier $\mathbf{B}$ is then found from the constraint

$$\mathbf{m} = \frac{1}{4}\left[\frac{\mathbf{B}_A}{|\mathbf{B}_A|}\tanh\left(\frac{|\mathbf{B}_A|}{2k_BT}\right) + \frac{\mathbf{B}_B}{|\mathbf{B}_B|}\tanh\left(\frac{|\mathbf{B}_B|}{2k_BT}\right)\right]. \quad (4.5)$$

Minimising the free energy subject to this constraint, we find the critical temperature at which $\langle\mathbf{n}\rangle$ becomes nonzero to be

$$T_c = Jzm_z/[2k_B\,\mathrm{arctanh}(2m_z)]. \quad (4.6)$$

At this point and throughout the antiferromagnetic phase, the constraint is solved by $\mathbf{B} = 2Jz\mathbf{m}$ and $\langle\mathbf{n}\rangle$ is perpendicular to $\mathbf{m}$ in the minimum of the free energy. By contrast, in the Ising model where $\mathbf{n}$ and $\mathbf{m}$ are restricted to be parallel, the critical temperature one obtains is $T_c = zJ(1/4-m^2)/k_B$.

We perform a variational calculation substituting the spin-texture of the meron into equation (4.1) to determine its characteristic size for a range of temperatures and imbalance. A meron spin texture in the x-y plane with vorticity $n_v = \pm 1$ can be described by

$$\mathbf{n} = \left\{\sqrt{n^2-[n_z(r)]^2}\cos\phi, n_v\sqrt{n^2-[n_z(r)]^2}\sin\phi, n_z(r)\right\}, \quad (4.7)$$

where $n = |\langle\mathbf{n}\rangle|$ and ϕ is the azimuth in the x-y plane. Exact meron solutions that follow from minimising the non-linear sigma model action with this texture have an out-of-plane component that behaves as $n - n_z(r) \propto r^2$ near the origin and that decays exponentially far from the origin [103]. A suitable variational ansatz that has the right properties near the origin but decays only as a power law for large r is $n_z(r) = n/[(r/\lambda)^2+1]^2$. In this case, the energy of a single meron due to the

gradient term in the non-linear sigma model is $Jn^2\pi[(511/60) - \pi - 6\ln 2 + (1/2)\ln(A/\pi\lambda^2)] + \mathcal{O}(A^{-1})$ which diverges as the logarithm of the area A of the system. Incorporating the correct exponential decay at large distances changes the constant terms in this expression but leaves the logarithm unaffected, indicating that our ansatz is indeed suitable to determine the characteristic core radius λ of a single meron. The core radius can be found by minimising the sum of the gradient energy and the integrated on-site free energy in equation (4.4) of the meron texture, which leads to the optimal size shown in Fig. 4.3(b). The Pontryagin index of the texture with this variational ansatz is $+1/2$ and the texture with index $-1/2$ is produced by substituting $n_z(r) \to -n_z(r)$. However, as noted earlier, our variational result for a texture with an opposite index will be identical. Also, the core structure will play no role in the interaction so long as the spacing of a pair of merons is larger than the size λ.

The Kosterlitz-Thouless critical temperature has been calculated for an anisotropic $O(3)$ model using Monte Carlo techniques [93]. By making an analogy between the free energy contribution of our non-linear sigma model and the anisotropy term in the anisotropic $O(3)$ model, we can use the numerical results of the anisotropic $O(3)$ model to estimate the critical temperature for the imbalanced antiferromagnet that incorporates fluctuations beyond mean-field theory. Although for $m_z \lesssim 0.2$ our anisotropy is more complicated than that which is used in the Monte Carlo simulations, we do not expect a rigourous calculation to deviate significantly from the results presented in Fig. 4.4.

Acknowledgements

We are very grateful to Rembert Duine and Randy Hulet for providing useful comments and Niels Pannevis for his help with obtaining the results of the imbalanced Ising antiferromagnet. This work is supported by the Stichting voor Fundamenteel Onderzoek der Materie (FOM) and the Nederlandse Organisatie voor Wetenschaplijk Onderzoek (NWO).

Notes

1. In three dimensions, vortex rings also have a finite energy below the critical temperature. The core spins then lie on a vortex line that forms closed loop in the lattice.

5 The BEC-BCS crossover

One feature of ultracold atomic gases that underpins the success of experiments with such gases is that the interaction strength between the atoms can be tuned. This is possible due to the presence of Feshbach resonances in those gases. As we shall see, these Feshbach resonances stitch together two contrasting pairing regimes in what has been called the BEC-BCS crossover. Determining the critical temperature for Bose-Einstein condensation of pairs throughout this crossover is an important theoretical challenge, and significant progress was made to resolve this problem when Nozières and Schmitt-Rink realised that they could reproduce certain crucial properties of the crossover in a Fermi gas by summing a particular class of diagrams in the perturbative expansion of the partition function.

After introducing Feshbach resonances and the BEC-BCS crossover, we shall show below how the technique of Nozières and Schmitt-Rink is applied to a Bose gas. Then, the BEC-BCS crossover in an optical lattice will be considered in chapter 6, and a Nozières and Schmitt-Rink theory will be used to calculate the critical temperature in a Bose gas in chapter 7, where we also consider effects beyond those which are present in Nozières and Schmitt-Rink theory.

5.1 Feshbach resonances

Feshbach originally described resonances observed in scattering of neutrons with atomic nuclei by introducing two distinct channels by which the scattering process can occur [104, 105]. Elastic scattering occurs via

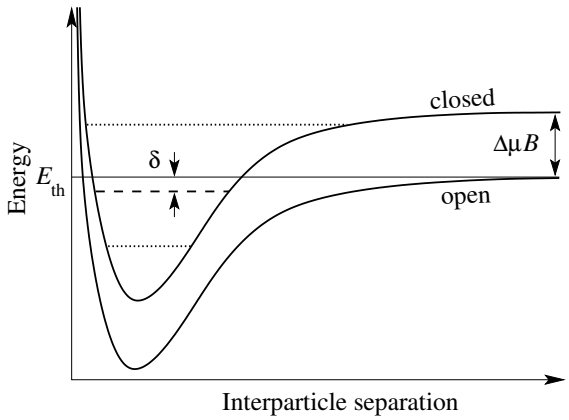

Figure 5.1: Schematic of a Feshbach resonance in a two-channel system. The solid curves are the interaction potentials of the open and closed channels for various interatomic separations, and the bound state supported by the closed-channel potential is shown as the dashed line. The threshold energy $E_{\rm th}$ is the energy of the atomic continuum, and the detuning δ is the energy of the bound state with respect to $E_{\rm th}$. Here, $\Delta\mu$ is the difference of magnetic moments between the open- and closed-channel atoms and B is the magnetic field bias. A Feshbach resonance occurs when $\delta \to 0$. The dotted lines denote other closed-channel bound states which give rise to other Feshbach resonances.

the *open* channel, while scattering mediated by the formation of a long-lived intermediate state, a compound nucleus in this case, occurs in the *closed* channel. The intermediate state is responsible for the observed resonance in the scattering cross-section and exists in a different part of the quantum-mechanical Hilbert space than that of the incoming particles. Scattering resonances described in such a two-channel picture have since become known as Feshbach resonances, and have also been found to occur in ultracold atomic gases [33, 34]. There, two atoms in different hyperfine states interacting in the closed channel form a long-lived diatomic molecule with a binding energy close to that of the incoming atoms. This is illustrated in Fig. 5.1, which shows the interaction potentials of the two channels as a function of the atomic separation.

Incoming atoms that are in the open channel at the threshold energy $E_{\rm th}$ can scatter into the closed-channel bound state, and back into the open channel. The magnetic moment of atoms in the closed channel differs from that of the open channel atoms by $\Delta\mu$. Thus, when an magnetic field bias with strength B is applied, the Zeeman shift of atoms in the closed channel

will differ by $\Delta\mu B$ for large interatomic spacings compared with that of the open channel atoms. In turn, this shifts the energy difference δ of the bound state with respect to the threshold allowing the total s-wave scattering length to be dialed to almost any value, as shown in Fig. 1.1.

The contribution to the scattering length of the open channel potential and other bound states in the closed channel is typically referred to as the background scattering length and denoted by $a_{\rm bg}$.[1] The total scattering length can then be expressed as a sum of this background plus a resonant piece as

$$a(B) = a_{\rm bg}\left(1 - \frac{\Delta B}{B - B_0}\right). \tag{5.1}$$

Here, ΔB is the characteristic width of the resonance which describes the coupling between the open and closed channels, and B_0 is the experimentally determined location of the Feshbach resonance. The energy of the closed channel bound state measured with respect to the energy of atoms in the open channel, $\delta = \Delta\mu(B - B_0)$, is called the detuning from resonance and vanishes on resonance. Eq. (5.1) shows that although the two-body interactions considered here always have a strongly attractive potential well, the presence of a bound state in the closed channel can give rise to a positive scattering length.

5.2 BEC-BCS crossover

The situation depicted in Fig. 5.1 corresponds to the regime when $B < B_0$ which is called the BEC limit. There, two particles in a vacuum will form a tightly bound closed-channel molecule, and the ground state of the many-particle system is a Bose-Einstein condensate of such molecules that are bound by two-body effects. As B is increased, the energy level of the closed-channel bound state increases, reaching the atomic threshold energy at the Feshbach resonance when $B = B_0$. In the opposite regime when $B > B_0$, called the BCS limit, there is no stable two-body molecule as the binding energy of the closed-channel pair is above the atomic threshold energy. However, many-body effects play an important role in the BCS limit. There, $a < 0$ and the resulting attractive interactions gives rise to the formation of Cooper pairs, which is purely a many-body effect.

The crossover occurring as B is varied between the BEC and BCS limits, known as the BEC-BCS crossover, can be described at zero temperature by a mean-field analysis using the usual BCS variational ansatz

for the ground-state wavefunction. There, the presence of a Bose-Einstein condensate of Cooper pairs in the BCS limit is signaled by a nonzero value of the BCS order parameter Δ, where 2Δ can be interpreted as the binding energy of a Cooper pair at zero temperature. The mean-field theory leads to two coupled equations for the density and the order parameter which can be solved throughout the crossover and smoothly interpolate between these two limits at zero temperature. In the BCS limit, the solution for the gap is

$$|\Delta| = \frac{8}{e^2}\varepsilon_F e^{-\pi/2k_F|a|} \tag{5.2}$$

while in the BEC limit,

$$|\Delta| = \varepsilon_F \sqrt{\frac{16}{3\pi k_F|a|}} \tag{5.3}$$

where $k_F = (3\pi^2 n)^{1/3}$ is the Fermi wave vector in an ideal Fermi gas with total density n, and $\varepsilon_F = \hbar^2 k_F^2/2m$.

The critical temperature for the Bose-Einstein condensation of Cooper pairs in the weak-coupling BCS limit can also be found from mean-field theory. There, the depletion of the condensate is driven by the breaking of Cooper pairs into individual atoms, and the corresponding increase in entropy dominates the thermodynamics. This process is easily incorporated in usual BCS mean-field theory which then produces the famous result

$$T_c = \frac{e^\gamma}{k_\mathrm{B}\pi}\Delta \tag{5.4}$$

where $\gamma \simeq 0.5772$ is Euler's constant, k_B is Boltzmann's constant, and Δ is determined from Eq. (5.2). This result is shown as the dashed line in Fig. 5.2. However, in the opposite BEC limit, the pairs are deeply bound molecules that never unbind at the ultracold temperatures of interest. Instead, T_c is determined by the centre-of-mass motion of the molecules and the onset of condensation is signaled by a macroscopic occupation of the zero-momentum state. The critical temperature is then one of an ideal Bose gas of molecules,

$$T_c = \frac{\pi\hbar^2}{mk_\mathrm{B}}\left(\frac{n_\mathrm{m}}{\zeta(3/2)}\right)^{2/3} \tag{5.5}$$

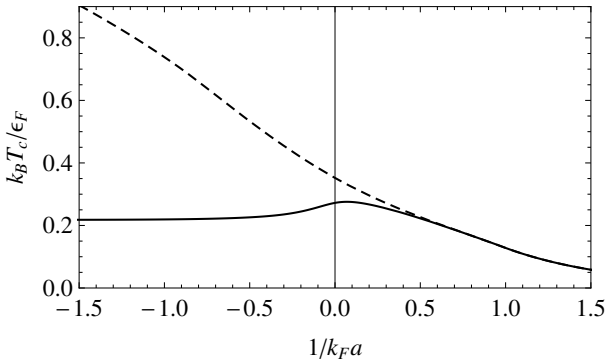

Figure 5.2: Illustration of critical temperature for condensation T_c in a Fermi gas (solid line). In the BEC limit on the left side of the plot, the critical temperature calculated from BCS mean-field theory (dashed line) differs significantly from the limiting value given by Eq. (5.5).

where $n_{\mathrm{m}} = n/2$ is the density of molecules. BCS mean-field theory fails to reproduce the correct critical temperature in the BEC limit due to the absence of noncondensed molecules in the BCS wavefunction.

The emergence of molecules in the BEC limit is signaled by the appearance of a pole in the scattering T-matrix. Therefore, a theory which smoothly connects the BEC and BCS limits at nonzero temperatures should incorporate the T-matrix. As explained below, from the Lippmann-Schwinger equation for the T-matrix, this is equivalent to summing ladder diagrams in the perturbative expansion of the partition function.

5.3 Nozières and Schmitt-Rink theory

Prompted by the need for a theory that includes the T-matrix, Nozières and Schmitt-Rink proceeded to sum all the ladder diagrams for a Fermi gas to calculate the critical temperature for the onset of superconductivity as a function of the coupling strength throughout the BEC-BCS crossover [106]. Here, in anticipation of chapter 7, we will illustrate their calculation for a homogeneous Bose gas.

5.3.1 Action for a Bose gas

The action for interacting bosons of mass m is $S = S_0 + S_{\rm int}$, where

$$\begin{aligned} S_0[\phi^*,\phi] =& \int_0^{\hbar\beta} d\tau \int d\mathbf{x}\ \phi^*(\mathbf{x},\tau)\left\{\hbar\partial_\tau - \frac{\hbar^2\nabla^2}{2m} - \mu\right\}\phi(\mathbf{x},\tau), \\ S_{\rm int}[\phi^*,\phi] =& \frac{1}{2}\int_0^{\hbar\beta} d\tau d\tau' \int d\mathbf{x} d\mathbf{x}'\ \phi^*(\mathbf{x},\tau)\phi^*(\mathbf{x}',\tau')V(\mathbf{x}-\mathbf{x}')\phi(\mathbf{x}',\tau')\phi(\mathbf{x},\tau). \end{aligned} \tag{5.6}$$

At low temperatures where the thermal De Broglie wavelength $\Lambda_{\rm th} = \sqrt{2\pi\hbar^2/mk_{\rm B}T}$ is much larger than the range of the interatomic interaction, the interaction potential may be accurately modeled as a δ-function and the interaction part of the action becomes

$$S_{\rm int}[\phi^*,\phi] = \frac{V_0}{2}\int_0^{\hbar\beta} d\tau \int d\mathbf{x}\ \phi^*(\mathbf{x},\tau)^2\phi(\mathbf{x},\tau)^2. \tag{5.7}$$

We define the noninteracting expectation value as

$$\langle \ldots \rangle_0 \equiv \frac{1}{Z_0}\int \mathscr{D}\phi^*\mathscr{D}\phi\ \ldots e^{-\frac{1}{\hbar}S_0[\phi^*,\phi]}, \tag{5.8}$$

where

$$Z_0 \equiv \int \mathscr{D}\phi^*\mathscr{D}\phi\ e^{-\frac{1}{\hbar}S_0[\phi^*,\phi]} = \exp\left[-\sum_{\mathbf{k}} \ln(1-e^{-\beta(\varepsilon_{\mathbf{k}}-\mu)})\right]. \tag{5.9}$$

The interacting part of the partition function of the system Z can be expanded as a series,

$$\begin{aligned} Z =& \int \mathscr{D}\phi^*\mathscr{D}\phi\ e^{-\frac{1}{\hbar}S_0[\phi^*,\phi]} e^{-\frac{1}{\hbar}S_{\rm int}[\phi^*,\phi]} \\ =& Z_0\langle e^{-\frac{1}{\hbar}S_{\rm int}[\phi^*,\phi]}\rangle_0 \\ =& Z_0\left(1 - \frac{1}{\hbar}\langle S_{\rm int}[\phi^*,\phi]\rangle_0 + \frac{1}{\hbar^2}\frac{1}{2!}\langle S_{\rm int}[\phi^*,\phi]^2\rangle_0 + \cdots\right) \\ =& Z_0\Bigg(1 + \frac{1}{2}2 \quad + \frac{1}{2!}\left(\frac{1}{2}\right)^2\Bigg[4 \quad + 4 \quad \\ & \qquad\qquad +16 \quad \Bigg] + \cdots\Bigg) \end{aligned} \tag{5.10}$$

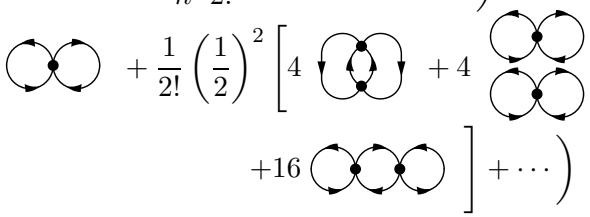

where the multiplicities of the diagrams were calculated from the pre-diagrams constructed from oriented vertices since the fields are complex. The total number of diagrams at the p^{th} order is $(2p)!$, and we adopt the convention that each vertex contributes a factor of $-V_0/\hbar$. By rewriting the series as an exponent, the disconnected diagrams are automatically canceled and we obtain

$Z =$ 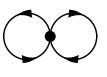 (5.11)

For a dilute system we must at least incorporate the two-body physics, and summing ladder diagrams does so exactly. Thus, although Eq. (5.11) is general, we only consider the contribution of ladder diagrams here. Bubble diagrams become important for long-range interactions and screening effects, and are discussed in Appendix D.

5.3.2 Many-body T-matrix

The T-matrix is the solution of the Lippmann-Schwinger equation. Diagrammatically, this can be written as a sum of ladder diagrams

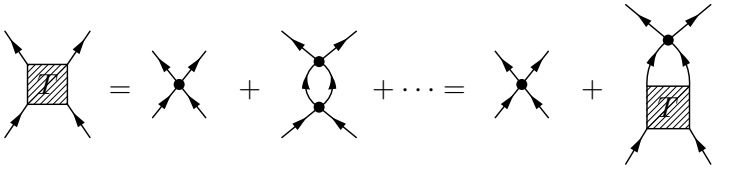 (5.12)

By closing the external lines, we obtain the self-energy in the ladder approximation, which, aside from a prefactor $1/p$, is the diagrammatic series we wish to calculate in the exponent in Eq. (5.11), namely,

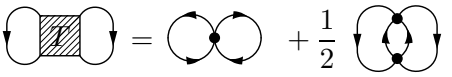 (5.13)

To explicitly calculate the first few diagrams in the ladder sum, we Fourier transform the fields according to

$$\phi(\mathbf{x},\tau) = \sum_{n,\mathbf{k}} \phi(\mathbf{k}, i\omega_n) \frac{e^{i\mathbf{k}\cdot\mathbf{x}}}{\sqrt{V}} \frac{e^{-i\omega_n \tau}}{\sqrt{\hbar\beta}},$$

where $\omega_n = 2\pi n/\hbar\beta$ are the even Matsubara frequencies. Using Wick's theorem, the first order term is then,

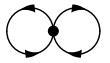

$$\begin{aligned}
&= -\frac{1}{\hbar}\langle S_{\text{int}}[\phi^*,\phi]\rangle_0 \\
&= -\frac{V_0}{2\hbar}\int_0^{\hbar\beta} d\tau \int d\mathbf{x}\ \langle \phi^*(\mathbf{x},\tau)\phi^*(\mathbf{x},\tau)\phi(\mathbf{x},\tau)\phi(\mathbf{x},\tau)\rangle_0 \\
&= -\frac{V_0}{\hbar}\int_0^{\hbar\beta} d\tau \int d\mathbf{x}\ \langle \phi(\mathbf{x},\tau)\phi^*(\mathbf{x},\tau)\rangle_0^2 \\
&= -\frac{V_0}{\hbar}\frac{1}{\hbar\beta V}\sum_{nn'}\sum_{\mathbf{k}\mathbf{k}'} G(\mathbf{k},n)G(\mathbf{k}',n') \\
&= -V_0 n^2 \beta V, \qquad (5.14)
\end{aligned}$$

where n is the total particle density. Similarly, the diagram in the second term of the ladder sum is

$$= \frac{V_0^2}{\hbar^2}\int_0^{\hbar\beta} d\tau d\tau' \int d\mathbf{x} d\mathbf{x}' \left(\langle \phi(\mathbf{x}',\tau')\phi^*(\mathbf{x},\tau)\rangle_0\right)^2 \left(\langle \phi(\mathbf{x},\tau)\phi^*(\mathbf{x}',\tau')\rangle_0\right)^2 \qquad (5.15)$$

$$\begin{aligned}
&= \frac{V_0}{\hbar}\frac{1}{(\hbar\beta V)^2}\sum_{n,n'}\sum_{\mathbf{k},\mathbf{k}'}\frac{-\hbar}{-i\hbar\omega_n + \varepsilon_{\mathbf{k}} - \mu}\frac{-\hbar}{-i\hbar\omega_{n'} + \varepsilon_{\mathbf{k}'} - \mu} \\
&\quad \times \frac{V_0}{\hbar}\sum_{m,\mathbf{q}}\frac{-\hbar}{-i\hbar\omega_{n'+m} + \varepsilon_{\mathbf{k}'+\mathbf{q}} - \mu}\frac{-\hbar}{-i\hbar\omega_{n-m} + \varepsilon_{\mathbf{k}-\mathbf{q}} - \mu}. \qquad (5.16)
\end{aligned}$$

The internal Matsubara summation over m can be evaluated, which gives

$$\begin{aligned}
&\frac{V_0}{\hbar}\sum_{m,\mathbf{q}}\frac{\hbar}{i\hbar\omega_m + i\hbar\omega_{n'} - (\varepsilon_{\mathbf{k}'+\mathbf{q}} - \mu)}\frac{-\hbar}{i\hbar\omega_m - i\hbar\omega_n + \varepsilon_{\mathbf{k}-\mathbf{q}} - \mu} \\
&\qquad = -\hbar\beta V\, V_0 \frac{1}{V}\sum_{\mathbf{q}}\frac{N(\varepsilon_{\mathbf{K}/2+\mathbf{q}} - \mu) + N(\varepsilon_{\mathbf{K}/2-\mathbf{q}} - \mu) + 1}{i\hbar\omega_M - \varepsilon_{\mathbf{K}/2-\mathbf{q}} - \varepsilon_{\mathbf{K}/2+\mathbf{q}} + 2\mu} \\
&\qquad \equiv -\hbar\beta V\, V_0 \Xi(\mathbf{K}, i\omega_M)
\end{aligned}$$

where we defined $\mathbf{K} = \mathbf{k} + \mathbf{k}'$ and $M = n + n'$, and shifted $\mathbf{q} \mapsto \mathbf{q} + \frac{\mathbf{k}-\mathbf{k}'}{2}$. The function $\Xi(\mathbf{K}, i\omega_M)$ is the response function in the particle-particle channel. Substituting this into Eq. (5.16), we obtain the following

expression for the second order diagram in the ladder sum,

$$= -\frac{V_0}{\hbar}\frac{1}{(\hbar\beta V)^2}\hbar\beta V \sum_{n,n'}\sum_{\mathbf{k},\mathbf{k}'} G(\mathbf{k},n)G(\mathbf{k}',n')V_0\Xi(\mathbf{k}+\mathbf{k}',n+n'). \tag{5.17}$$

To obtain the entire ladder series in Eq. (5.13), we note that the p-th order diagram of the series has p internal loops, each contributing a factor of $V_0\Xi(\mathbf{K},n+n')$. Including the overall combinatorial factor $1/(p+1)$, we thus write down an expression for the ladder sum,

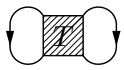

$$\begin{aligned}
&= \frac{-V_0}{\hbar^2\beta V}\sum_{n,n'}\sum_{\mathbf{k},\mathbf{k}'}\frac{G(\mathbf{k},n)G(\mathbf{k}',n')}{V_0\Xi(\mathbf{k}+\mathbf{k}',i\omega_M)}\sum_{p=1}^{\infty}\frac{1}{p}\big[V_0\Xi(\mathbf{k}+\mathbf{k}',M)\big]^p \\
&= \frac{-1}{\hbar^2\beta V}\sum_{\substack{M,m''\\ P(M)=P(m'')}}\sum_{\mathbf{K},\mathbf{k}''} G\left(\frac{\mathbf{K}}{2}+\mathbf{k}'',\frac{M+m''}{2}\right)G\left(\frac{\mathbf{K}}{2}-\mathbf{k}'',\frac{M-m''}{2}\right) \\
&\qquad\qquad \times\frac{V_0}{V_0\Xi(\mathbf{K},i\omega_M)}\sum_{p=1}^{\infty}\frac{1}{p}\big[V_0\Xi(\mathbf{K},i\omega_M)\big]^p
\end{aligned} \tag{5.18}$$

where the centre-of-mass frequency and momentum is $M = n + n'$ and $\mathbf{K} = \mathbf{k} + \mathbf{k}'$, and the relative frequency and momentum is $m'' = n - n'$, and $\mathbf{k}'' = (\mathbf{k} - \mathbf{k}')/2$, respectively. Here, $P(M) = P(m'')$ denotes that M and m'' should have the same parity[2].

Relative Matsubara summation

The sum over the relative Matsubara frequency m'' can be performed explicitly[3],

$$\begin{aligned}
&\sum_{\substack{m'',\mathbf{k}''\\ P(M)=P(m'')}} G\left(\frac{\mathbf{K}}{2}+\mathbf{k}'',\frac{M+m''}{2}\right)G\left(\frac{\mathbf{K}}{2}-\mathbf{k}'',\frac{M-m''}{2}\right) \\
&\quad= \sum_{\mathbf{k}''}\frac{-\hbar}{-i\hbar\omega_M+\varepsilon_{\mathbf{K}/2+\mathbf{k}''}+\varepsilon_{\mathbf{K}/2-\mathbf{k}''}-2\mu} \\
&\qquad\qquad\times\sum_{n\in\mathbb{Z}}\left[\frac{\hbar}{i\hbar\omega_n-(\varepsilon_{\mathbf{K}/2+\mathbf{k}''}-\mu)}-\frac{\hbar}{i\hbar\omega_n+\varepsilon_{\mathbf{K}/2-\mathbf{k}''}-\mu}\right] \\
&\quad= -\hbar^2\beta\sum_{\mathbf{k}''}\frac{N(\varepsilon_{\mathbf{K}/2+\mathbf{k}''}-\mu)+N(\varepsilon_{\mathbf{K}/2-\mathbf{k}''}-\mu)+1}{i\hbar\omega_M-\varepsilon_{\mathbf{K}/2+\mathbf{k}''}-\varepsilon_{\mathbf{K}/2-\mathbf{k}''}+2\mu} \\
&\quad= -\hbar^2\beta V\Xi(\mathbf{K},i\omega_M)
\end{aligned} \tag{5.19}$$

Substituting this into Eq. (5.18), we obtain

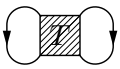

$$= \sum_{M,\mathbf{K}} \sum_{p=1}^{\infty} \frac{1}{p} \left[V_0 \Xi(\mathbf{K}, i\omega_M) \right]^p. \tag{5.20}$$

To verify this result, we calculate the first term of this series which, as we saw in Eq. (5.14), should be equal to $V_0 n^2 (-\beta V)$. Indeed, we find

$$\begin{aligned}
\frac{-V_0}{\beta V} \sum_{M,\mathbf{K}} \Xi(\mathbf{K}, i\omega_M) =& \frac{-V_0}{\beta V^2} \sum_{M,\mathbf{K},\mathbf{k}''} \frac{N(\varepsilon_{\mathbf{K}/2+\mathbf{k}''} - \mu) + N(\varepsilon_{\mathbf{K}/2-\mathbf{k}''} - \mu) + 1}{i\hbar\omega_M - \varepsilon_{\mathbf{K}/2+\mathbf{k}''} - \varepsilon_{\mathbf{K}/2-\mathbf{k}''} + 2\mu} \\
=& \frac{V_0}{V^2} \sum_{\mathbf{K},\mathbf{k}''} \left[N(\varepsilon_{\mathbf{K}/2+\mathbf{k}''} - \mu) + N(\varepsilon_{\mathbf{K}/2-\mathbf{k}''} - \mu) + 1 \right] \\
& \times N(\varepsilon_{\mathbf{K}/2+\mathbf{k}''} + \varepsilon_{\mathbf{K}/2-\mathbf{k}''} - 2\mu) \\
=& \frac{V_0}{V^2} \sum_{\mathbf{k},\mathbf{k}'} N(\varepsilon_{\mathbf{k}} - \mu) N(\varepsilon_{\mathbf{k}'} - \mu) = V_0 n^2
\end{aligned}$$

as expected.

Renormalization

The momentum sum in $\Xi(\mathbf{K}, i\omega_M)$ gives rise to an ultraviolet divergence. Indeed, for large momenta the Bose occupations numbers are zero, and

$$\frac{1}{i\hbar\omega_M - \varepsilon_{\mathbf{K}/2-\mathbf{q}} - \varepsilon_{\mathbf{K}/2+\mathbf{q}} + 2\mu} \simeq \frac{-1}{2\varepsilon_{\mathbf{q}}}. \tag{5.21}$$

Thus, the internal momentum sum diverges,

$$\frac{1}{V} \sum_{\mathbf{q}} \frac{-1}{2\varepsilon_{\mathbf{q}}} = \lim_{\Lambda\to\infty} 4\pi \int_0^{\Lambda} \frac{dq}{(2\pi)^3} q^2 \frac{-2m}{2\hbar^2 q^2} = \lim_{\Lambda\to\infty} \frac{-2m}{\hbar^2 (2\pi)^2} \Lambda.$$

This is due to the assumption of a contact interaction potential $V_0 \delta(\mathbf{x} - \mathbf{x}')$ which presumes that the interaction is local, i.e., momentum independent. However, the momenta in the perturbative corrections are not restricted to the range $\hbar/\Lambda_{\text{th}}$ and therefore these corrections are sensitive to the precise details of the potential $V(\mathbf{x} - \mathbf{x}')$. By solving the Lippmann-Schwinger equation, Eq. (5.12), for the two-body T-matrix, we obtain

$$\frac{1}{T^{2\text{B}}(i\omega_M)} = \frac{1}{V_0} - \frac{1}{V} \sum_{\mathbf{q}} \frac{1}{i\hbar\omega_M - 2\varepsilon_{\mathbf{q}}}. \tag{5.22}$$

In particular, this also holds at zero energy,

$$\frac{1}{V_0} = \frac{1}{T^{2\mathrm{B}}} - \frac{1}{V}\sum_{\mathbf{q}} \frac{1}{2\varepsilon_{\mathbf{q}}} \tag{5.23}$$

where, from elementary scattering theory, $T^{2\mathrm{B}}(0) \equiv T^{2\mathrm{B}} = 4\pi a\hbar^2/m$. The second term has precisely the form of the divergence in the response function in Eq. (5.21). This motivates us to replace V_0 by the two-body T-matrix to remove the divergence due to the contact potential. Thus, Eq (5.22), becomes

$$\begin{aligned}
\frac{1}{T^{2\mathrm{B}}(i\omega_M)} =& \frac{1}{T^{2\mathrm{B}}} - \frac{1}{V}\sum_{\mathbf{q}} \left(\frac{1}{i\hbar\omega_M - 2\varepsilon_{\mathbf{q}}} + \frac{1}{2\varepsilon_{\mathbf{q}}} \right) \\
=& \frac{1}{T^{2\mathrm{B}}} - 4\pi \int_0^\infty \frac{dq}{(2\pi)^3} q^2 \left(\frac{1}{i\hbar\omega_M - \hbar^2q^2/m} + \frac{1}{\hbar^2q^2/m} \right) \\
=& \frac{1}{T^{2\mathrm{B}}} - \frac{m^{3/2}}{4\pi\hbar^3}\sqrt{-i\hbar\omega_M}
\end{aligned} \tag{5.24}$$

where we took the thermodynamic limit in the second step. To cancel the divergence, we thereby renormalize the theory with the substitution

$$\frac{1}{V_0} - \Xi(\mathbf{K}, i\omega_M) \to \frac{1}{T^{2\mathrm{B}}(i\omega_M)} - \Xi'(\mathbf{K}, i\omega_M) \tag{5.25}$$

where the renormalized response function in the particle-particle channel is

$$\begin{aligned}
\Xi'(\mathbf{K}, i\omega_M) =& \Xi(\mathbf{K}, i\omega_M) - \frac{1}{V}\sum_{\mathbf{q}} \frac{1}{i\hbar\omega_M - 2\varepsilon_{\mathbf{q}}} \\
=& \frac{1}{V}\sum_{\mathbf{q}} \left[\frac{N(\varepsilon_{\mathbf{K}/2+\mathbf{q}} - \mu) + N(\varepsilon_{\mathbf{K}/2-\mathbf{q}} - \mu) + 1}{i\hbar\omega_M - \varepsilon_{\mathbf{K}/2-\mathbf{q}} - \varepsilon_{\mathbf{K}/2+\mathbf{q}} + 2\mu} - \frac{1}{i\hbar\omega_M - 2\varepsilon_{\mathbf{q}}} \right].
\end{aligned} \tag{5.26}$$

Now, summing the ladder series, we finally obtain a finite expression for the self-energy in the ladder approximation in terms of the many-body

T-matrix,

$$\begin{aligned}
\text{ 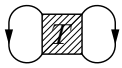 } &= \sum_{M,\mathbf{K}} \sum_{p=1}^{\infty} \frac{1}{p} \left[V_0 \Xi(\mathbf{K}, i\omega_M) \right]^p \\
&= \sum_{M,\mathbf{K}} \ln \left[\frac{1}{V_0} \frac{1}{\frac{1}{V_0} - \Xi(\mathbf{K}, i\omega_M)} \right] \\
&= \sum_{M,\mathbf{K}} \ln \left[\frac{T^{2\mathrm{B}}(i\omega_M)}{1 - T^{2\mathrm{B}}(i\omega_M) \Xi'(\mathbf{K}, i\omega_M)} \right] - \ln V_0 \\
&= \sum_{M,\mathbf{K}} \left(\ln \left[T^{\mathrm{MB}}(\mathbf{K}, i\omega_M) \right] + \ln \frac{1}{V_0} \right) \qquad (5.27)
\end{aligned}$$

where the many-body T-matrix is

$$T^{\mathrm{MB}}(\mathbf{K}, i\omega_M) = \frac{1}{[T^{2\mathrm{B}}(i\omega_M)]^{-1} - \Xi'(\mathbf{K}, i\omega_M)}. \qquad (5.28)$$

The constant term proportional to $\ln V_0$ in Eq. (5.27) will not contribute to the thermodynamics and can hence be dropped from the thermodynamic potential.

5.3.3 Thermodynamic Potential

Thermodynamic quantities of the system such as the critical temperature and pressure are most conveniently expressed in terms of the thermodynamic potential Ω. Using Eq. (5.27) we can write this as,

$$\begin{aligned}
\frac{\Omega}{V} &\equiv - \frac{1}{\beta V} \ln Z \\
&= - \frac{\ln Z_0}{\beta V} - \frac{1}{\beta V} \text{ 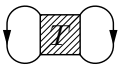 } \\
&= - \frac{1}{\beta V} \ln Z_0 - \frac{1}{\beta V} \sum_{M,\mathbf{K}} \ln \left[T^{\mathrm{MB}}(\mathbf{K}, i\omega_M) \right] \qquad (5.29)
\end{aligned}$$

where we still need to evaluate a momentum and frequency sum. The Matsubara summation can be evaluated explicitly by performing the analytic continuation of the Matsubara frequencies to the complex plane $i\omega_M \to z$. The Matsubara summation can then be expressed as an integral along a contour C_M enclosing the imaginary axis, with a kernel equal to the Bose

function $N(z) = (e^{\hbar\beta z} - 1)^{-1}$. In the first instance, we shall work with an energy-independent two-body T–matrix in Eq. (5.28) and set $T^{2\mathrm{B}}(i\omega_M)$ to $T^{2\mathrm{B}} = 4\pi a\hbar^2/m$. For convenience, we define

$$f(\mathbf{K}, z) = 1 - T^{2\mathrm{B}}\Xi'(\mathbf{K}, z) = \frac{T^{2\mathrm{B}}}{T^{\mathrm{MB}}(\mathbf{K}, z)}, \tag{5.30}$$

and write the Matsubara summation in Eq. (5.29) as

$$\frac{1}{\beta}\sum_M \ln f(i\omega_M) = \frac{\hbar}{2\pi i}\oint_{C_M} dz\, N(z)\ln f(z). \tag{5.31}$$

where for compactness we do not explicitly show the $\mathbf{K}$ dependence.

Now the integration contour enclosing the imaginary axis can be deformed to enclose the real axis as shown in Fig. 5.3, which allows us to rewrite the contour integral as a line integral. For this purpose, we define the analytic continuation of the logarithm in two different ways such that its argument lies within the range $(0, 2\pi)$ or within the range $(-\pi, \pi)$. It will soon become clear that this gives us the freedom to choose where to place the branch cut of the logarithm such that it never bisects the imaginary axis where a Matsubara pole lies at the origin. We denote these two branches of the logarithm as $\ln^{\pm}$, where

$$\begin{aligned}
\ln^+ f(z) &\equiv \ln|f(z)| + i\arg_{(0,2\pi)}[f(z)] \\
&= \ln|f(z)| + i\arctan\left(\frac{\Im f(z)}{\Re f(z)}\right) + i\pi\Big(\Theta[\Re f(z)]\,\mathrm{sgn}[-\Im f(z)] + 1\Big) \\
\ln^- f(z) &\equiv \ln|f(z)| + i\arg_{(-\pi,\pi)}[f(z)] \\
&= \ln|f(z)| + i\arctan\left(\frac{\Im f(z)}{\Re f(z)}\right) + i\pi\Theta[-\Re f(z)]\,\mathrm{sgn}[\Im f(z)].
\end{aligned} \tag{5.32}$$

Here, $\Theta[x]$ is the unit step, $\arg_{(\theta_1,\theta_2)}[z]$ denotes the argument of z expressed in the range (θ_1, θ_2), $\mathrm{sgn}(x)$ is the sign of x, and $\Re\, z$ and $\Im\, z$ denote the real and imaginary parts of z, respectively. Then the Matsubara summation

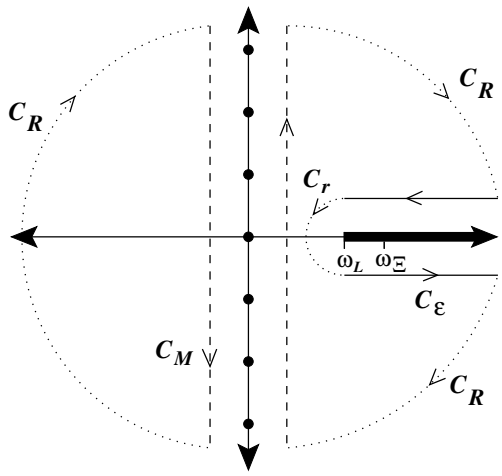

Figure 5.3: The domain of integrand in Eq. (5.31) showing the integration contours used in evaluating the Matsubara sum. The dots on the imaginary axis designate the poles of the Bose function, the branch point at ω_L marks the beginning of the of the branch cut of the logarithm and the branch cut of Ξ' begins at ω_Ξ (shown arbitrarily to lie to the right of ω_L here). The contour C_M consisting of dashed lines yields the Matsubara sum, which is equivalent to the contour C_ϵ consisting of horizontal lines a distance ϵ above and below the branch cuts. The contribution of the semicircular caps C_R and C_r, denoted by dotted lines, vanish leaving only a contribution from the line integrals above and below the branch cuts which begin at $\omega_0 = \min(\omega_L, \omega_\Xi)$.

becomes

$$\begin{aligned}
\frac{1}{\beta}\sum_M \ln f(i\omega_M) &= \lim_{\epsilon\to 0^+} \frac{\hbar}{2\pi i}\oint_{C_\epsilon} dz\, N(z)\ln f(z). \\
&= -\frac{\hbar}{2\pi i}\lim_{\epsilon\to 0^+}\int_{\omega_0}^{\infty} d\omega N(\omega)\left[\ln^{\pm} f(\omega+i\epsilon) - \ln^{\pm} f(\omega-i\epsilon)\right], \\
&= \hbar\lim_{\epsilon\to 0^+}\int_{\omega_0}^{\infty} d\omega N(\omega)\left[\frac{1}{\pi}\arctan\left(\frac{\Im f(\omega+i\epsilon)}{\Re f(\omega+i\epsilon)}\right)\right. \\
&\qquad \left. + \Theta[\pm\Re f(\omega+i\epsilon)]\,\mathrm{sgn}[\mp\Im f(\omega+i\epsilon)]\right].
\end{aligned} \tag{5.33}$$

The lower limit of integration $\omega_0 = \min(\omega_L, \omega_\Xi)$ will be determined in a moment. We see that by deforming the integration contour, the Matsubara

summation has thus been reduced to a real integral involving the real and imaginary parts of $f(z)$.

Taking the limit $\epsilon \to 0^+$, the imaginary part is

$$\begin{aligned}
&\Im f(\mathbf{K}, \omega + i\epsilon) \\
&= \lim_{\epsilon \to 0+} T^{2\mathrm{B}} \frac{1}{V} \sum_{\mathbf{q}} \hbar\epsilon \frac{N(\varepsilon_{\mathbf{K}/2+\mathbf{q}} - \mu) + N(\varepsilon_{\mathbf{K}/2-\mathbf{q}} - \mu) + 1}{\epsilon^2\hbar^2 + E(\mathbf{K}, \mathbf{q}, \omega)^2} \\
&= T^{2\mathrm{B}} \frac{1}{V} \sum_{\mathbf{q}} \frac{1}{\hbar} \left[N(\varepsilon_{\mathbf{K}/2+\mathbf{q}} - \mu) + N(\varepsilon_{\mathbf{K}/2-\mathbf{q}} - \mu) + 1 \right] \pi\delta(E(\mathbf{K}, \mathbf{q}, \omega)/\hbar)
\end{aligned}$$

where $E(\mathbf{K}, \mathbf{q}, \omega) = \hbar\omega - \varepsilon_{\mathbf{K}}/2 - 2\varepsilon_{\mathbf{q}} + 2\mu$ is the denominator of $\Xi(\mathbf{K}, z)$ along the line $z = \omega + i0$, and we used the Dirac delta function representation as a limit of the Lorentz distribution $\delta(x) = (1/\pi) \lim_{\epsilon \to 0} \epsilon/(\epsilon^2 + x^2)$. In the thermodynamic limit, this becomes

$$\Im f(\mathbf{K}, \omega + i0) = T^{2\mathrm{B}} \frac{1}{4\pi} \frac{m}{\hbar^2 K} \frac{m}{\hbar^2} \int_{\varepsilon_a}^{\varepsilon_b} d\varepsilon \left[N(\hbar\omega - \varepsilon + \mu) + N(\varepsilon - \mu) + 1 \right], \tag{5.34}$$

where the limits of integration imposed by the Dirac delta function are

$$\varepsilon_a = \frac{\hbar^2}{2m}(K/2 - \widetilde{K})^2, \qquad \varepsilon_b = \frac{\hbar^2}{2m}(K/2 + \widetilde{K})^2, \tag{5.35}$$

with

$$\widetilde{K} = \sqrt{\frac{2m}{\hbar^2}\left(\frac{\hbar\omega}{2} + \mu\right) - \left(\frac{K}{2}\right)^2}. \tag{5.36}$$

Performing the integral, we finally obtain the analytic expression

$$\Im f(\mathbf{K}, \omega + i0) = \frac{T^{2\mathrm{B}}}{2\pi\beta} \frac{m^2}{\hbar^4 K} \ln \left| \frac{\sinh\left[\frac{\beta}{2}\left(\frac{\hbar\omega}{2} - \frac{\hbar^2}{2m} K \widetilde{K}\right)\right]}{\sinh\left[\frac{\beta}{2}\left(\frac{\hbar\omega}{2} + \frac{\hbar^2}{2m} K \widetilde{K}\right)\right]} \right|. \tag{5.37}$$

Similarly, for the real part, we find

$$\begin{aligned}\Re f(\mathbf{K},\omega+i0) &= 1-\lim_{\epsilon\to 0^+} T^{2\mathrm{B}}\frac{1}{V}\sum_{\mathbf{q}}\Bigg\{\frac{1}{2\varepsilon_{\mathbf{q}}} \\ &\quad + E(\mathbf{K},\mathbf{q},\omega)\frac{N(\varepsilon_{\mathbf{K}/2+\mathbf{q}}-\mu)+N(\varepsilon_{\mathbf{K}/2-\mathbf{q}}-\mu)+1}{\epsilon^2\hbar^2+E(\mathbf{K},\mathbf{q},\omega)^2}\Bigg\} \\ &= 1-T^{2\mathrm{B}}\frac{m}{4\pi^2\hbar^2}\int_0^\infty dq\Bigg\{\frac{q}{K}\left[\frac{2}{e^{\beta(\varepsilon_q-\mu)}-1}+1\right] \\ &\quad \times\ln\left|\frac{\hbar\omega-\varepsilon_K-2\varepsilon_q+\frac{\hbar^2}{m}qK+2\mu}{\hbar\omega-\varepsilon_K-2\varepsilon_q-\frac{\hbar^2}{m}qK+2\mu}\right|+2\Bigg\}.\end{aligned} \tag{5.38}$$

Here, the integral cannot be evaluated analytically and must be performed numerically.

Branch cut structure

In order to evaluate the thermodynamic potential, we must find the lower limit of the frequency integral ω_0, which is determined by the branch cut structure of $\ln f(\mathbf{K},z)$, as illustrated in Fig. 5.3. Additionally, we must choose an appropriate analytic continuation of the logarithm, such that no branch cuts bisect the imaginary axis in order for the deformed integration contour to remain valid.

In $f(\mathbf{K},z)$, $\Xi'(\mathbf{K},\omega)$ is singular for a range of frequencies ω where its denominator is zero. The resulting branch cut begins at the branch point ω_Ξ given by

$$\omega_\Xi = \frac{\varepsilon_{\mathbf{K}}}{2}-2\mu, \tag{5.39}$$

which follows from $E(\mathbf{K},0,\omega_\Xi)=0$.

The branch cut due to the $\ln f(z)$ begins at the branch point ω_L, determined from the condition $f(\omega_L)=0$, and we find numerically that $\omega_L>0$ for the parameter ranges of interest here. However, the direction in which the branch cut extends from this branch point depends on how we analytically continue the logarithm to the complex plane. The two analytic continuations $\ln^\pm(z)$ proposed in Eq. (5.32) place the branch cut on the real axis, and we denote the set of all points on the branch cut corresponding to the two analytic continuations by

$$\mathrm{Cut}\left[\ln^\pm(z)\right]=\{\omega;\omega\in\mathbb{R},\omega\gtrless 0\}. \tag{5.40}$$

To see if the branch cut is present on the positive or negative side of the real axis, we check if a branch cut is present in the limit $\omega \to -\infty$. There, we have that $T^{\mathrm{MB}}(\omega) \to T^{\mathrm{2B}}(\omega)$ and

$$f(\omega) \to \frac{T^{\mathrm{2B}}}{T^{\mathrm{2B}}(\omega)} \simeq 1 - T^{\mathrm{2B}}\sqrt{-\omega} \tag{5.41}$$

Thus, in this limit,

$$\begin{aligned} \mathrm{Cut}\left[\ln^{\pm} f(z)\right] =& \{z; f(z) \in \mathbb{R}, f(z) \gtrless 0\} \\ \to& \{\omega; \omega \to -\infty, T^{\mathrm{2B}} \lesseqgtr 1\}. \end{aligned} \tag{5.42}$$

so we conclude that the branch cut is present on the negative real axis whenever $\mathrm{sgn}[T^{\mathrm{2B}}] = \mp 1$.

Since we are still at liberty to choose the definition of the logarithm, we choose the definition $\ln^{\mathrm{sgn}(T^{2B})} f(z)$ thereby ensuring that the cut does not lie on the interval $(-\infty, \omega_L)$ which would cause it to bisect the imaginary axis. With this choice, the contribution of the step-function to the integrand simplifies to

$$\begin{aligned} &\Theta[\pm \Re f(\omega + i0)]\, \mathrm{sgn}[\mp \Im f(\omega + i0)] \\ &\qquad = -\Theta[\mathrm{sgn}(T^{2B}) \Re f(\omega + i0)]\, \mathrm{sgn}[T^{2B} \Im f(\omega + i0)] \\ &\qquad = -\Theta[T^{2B} \Re f(\omega + i0)]. \end{aligned} \tag{5.43}$$

With this, we may write the thermodynamic potential per unit volume in Eq. (5.29) as a real and finite integral,

$$\begin{aligned} \frac{\Omega}{V} = &\frac{1}{\beta}\frac{1}{2}\left(\frac{2m}{\hbar^2}\right)^{3/2} \frac{4\pi}{(2\pi)^3} \int d\varepsilon \sqrt{\varepsilon} \ln\left(1 - e^{-\beta(\varepsilon - \mu)}\right) \\ &+ \hbar \int \frac{d\mathbf{K}}{(2\pi)^3} \int_{\omega_0}^{\infty} d\omega N(\omega) \left[\frac{1}{\pi} \arctan\left(\frac{\Im f(\mathbf{K}, \omega + i0)}{\Re f(\mathbf{K}, \omega + i0)}\right)\right. \\ &\left. - \Theta[T^{2B} \Re f(\mathbf{K}, \omega + i0)]\right] \end{aligned} \tag{5.44}$$

where $\omega_0 = \min(\omega_L, \omega_\Xi)$, and the imaginary and real parts of $f(\mathbf{K}, z) = T^{\mathrm{2B}}/T^{\mathrm{MB}}(\mathbf{K}, z)$ are given by Eq. (5.37) and Eq. (5.38), respectively.

5.3.4 Critical Temperature

The many-body T-matrix $T^{MB}(\mathbf{K},\omega) = T^{2B}f^{-1}(\mathbf{K},\omega)$ has a branch cut beginning at $\omega_\Xi(\mathbf{K},\mu)$ corresponding to the atomic continuum and, crucially, it also has a pole at $\omega_L(\mathbf{K},\mu)$ corresponding to infinite-lifetime molecules where $f[\omega_L(\mathbf{K},\mu)] = 0$ and $\omega_L(\mathbf{K},\mu) < \omega_\Xi(\mathbf{K},\mu)$. For $\omega_L(\mathbf{K},\mu) > \omega_\Xi(\mathbf{K},\mu)$ the pole becomes a resonance in the atomic continuum with $\Re f[\omega_L(\mathbf{K},\mu)] = 0$ and $\Im f[\omega_L(\mathbf{K},\mu)] \neq 0$, which corresponds to finite-lifetime pairs which can break into two atoms.

The presence of a molecular pole underlies the success of the NSR formalism in smoothly interpolating between the BEC and BCS regimes and, in particular, retrieving the correct critical temperature in both those limits. Throughout the BEC-BCS crossover, the critical temperature for the onset of Bose-Einstein condensation can be found from the Thouless criterion $\omega_L(\mathbf{0},\mu) = 0$, and this is the solid line plotted in Fig. 7.1.

One important shortcoming of the NSR formalism is the absence of interactions between pairs. These interactions are repulsive in Fermi gases due to Pauli blocking [107], however, attractive interactions between pairs in a Bose gas are important and can even cause the gas to collapse near the critical temperature. Extending the NSR formalism to include pair interactions is the topic of chapter 7.

Notes

1. The background scattering length $a_{\rm bg}$ also incorporates contributions arising from other bound states in the open and closed channel. If the energy of one particular bound state in the closed channel is close to the threshold energy, then contributions to the scattering length from other bound states will vary slowly with energy and their energy dependence in $a_{\rm bg}$ is usually neglected. However, energy dependence can be readily included; see chapter 7 for an example of this.
2. The sum over two Matsubara frequencies n, n' becomes a sum over "relative" and "centre-of-mass" Matsubara frequencies, denoted by m'' and M, respectively with the condition $P(m'') = P(M)$. Proof: For $n, n' \in \mathbb{Z}$, and $P(n)$ denoting the parity of n,

$$\begin{aligned}\mathbb{Z}\times\mathbb{Z} =& \{n,n';P(n)=P(n')\}+\{n,n';P(n)\neq P(n')\}\\ =& \{\frac{M+m''}{2},\frac{M-m''}{2};M,m''\in 2\mathbb{Z}\}+\{\frac{M+m''}{2},\frac{M-m''}{2};M,m''\in 2\mathbb{Z}+1\}\\ =& \{\frac{M+m''}{2},\frac{M-m''}{2};P(M)=(m'')\}\end{aligned}$$

where the second step can be shown explicitly using $P(n) = P(n')$
$\Leftrightarrow n = 2q + \alpha, n' = 2q' + \alpha \; \forall q, q' \in \mathbb{Z}, \alpha \in \{0, 1\}$, and $P(n) \neq P(n')$
$\Leftrightarrow n = 2q + \alpha, n' = 2q' + \alpha + 1$, etc.

3. Note that $\{(m'' \pm M)/2; M, m'' \in \mathbb{Z}, P(M) = P(m'')\} = \mathbb{Z}$.

6

BEC-BCS crossover in an optical lattice

We present the microscopic theory for the BEC–BCS crossover of an atomic Fermi gas in an optical lattice, showing that the Feshbach resonance underlying the crossover in principle induces strong multiband effects. Nevertheless, the BEC–BCS crossover itself can be described by a single–band model since it occurs at magnetic fields that are relatively far away from the Feshbach resonance. A criterion is proposed for the latter, which is obeyed by most known Feshbach resonances in ultracold atomic gases.

6.1 Introduction

Ever since the compelling work of DeMarco and Jin [28], the study of degenerate Fermi gases has been at the forefront of ultracold atomic physics. Much of the impetus behind current research in this field was provided by the successful experimental investigation in the last two years of the crossover between the Bose–Einstein condensate (BEC) of molecules and the Bardeen–Cooper–Schrieffer (BCS) state of Bose–Einstein condensed Cooper pairs [36–41, 108]. The pairing observed in an unequal spin mixture is presently under intense scrutiny [49, 109]. Another exciting direction being explored lately is the physics of ultracold Fermi gases in an optical lattice [110]. The latter gives, for instance, the possibility to experimentally solve the famous positive–U Hubbard model with repulsive on–site

This chapter has been previously published as *BEC-BCS crossover in an optical lattice*, Arnaud Koetsier, D. B. M Dickerscheid, and H. T. C. Stoof, Phys. Rev. A **74,** 033621 (2006).

interactions which is believed to embody the physics of high–temperature superconductors [59, 60]. The negative–U Hubbard model with an attractive on–site interaction [111] can also be explored. This model is interesting for example because, at half filling, particle–hole symmetry leads to an exact $SO(4)$ symmetry. Therefore, the physics at half filling is analogous with that of the $SO(5)$ theory proposed for high–temperature superconductors [112–114]. Moreover, at low filling fractions, a BEC–BCS crossover takes place. This is the subject of the present paper.

In the atomic gases of interest, studying the BEC–BCS crossover demands the exploitation of a Feshbach resonance [33, 34]. As a result, the physics is much richer than in the negative–U Hubbard model and requires a multiband description. This is elucidated in Fig. 6.1. In the absence of an optical lattice, and including solely two–body effects, a dressed molecule formally exists only below the Feshbach resonance with a binding energy which, near resonance, depends quadratically on the magnetic field. Its binding energy is shown as the dash–dotted line. Above the Feshbach resonance, the dressed molecule is merely a resonance state as it then has a finite lifetime due to the possibility of decaying into the atomic continuum [115] as represented by the dotted line continuation.

Placing the system in a sufficiently deep optical lattice, the bare (closed–channel) molecular state of the Feshbach resonance interacts primarily with a discrete set of atomic states instead of an atomic continuum. Thus, a dressed molecule now exists for all magnetic fields and its energy, plotted as dashed lines, shows a number of avoided crossings before it ultimately becomes a resonance in the continuum above the optical lattice potential.

Using this result, we can restate the interacting problem for deep optical lattices in terms of atoms and dressed molecules emerging from the on–site two–body solution. The binding energy of these dressed molecules obtained from our exact solution of the on–site Feshbach problem is in good agreement with recent experimental data [116, 117], showing the validity of this approach. Many–body physics enters if we allow both the atoms and the dressed molecules to hop to adjacent lattice sites [66]. In particular, for the low filling fractions considered, the two–body binding energy of the dressed molecules passes through the Fermi sea in the lowest Bloch band, as shown in the inset of Fig. 6.1. It is due to this phenomenon that the BEC–BCS crossover occurs in this resonantly interacting case [118]. The interaction of the molecules with the Fermi sea further

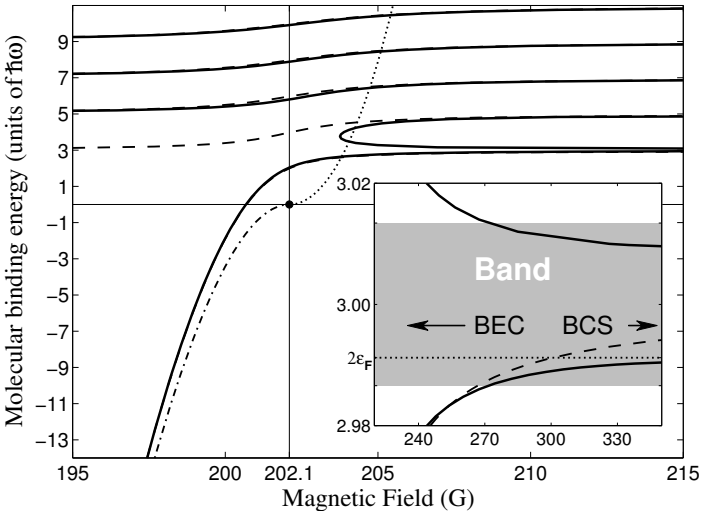

Figure 6.1: Comparison of the dressed molecular binding energy at various magnetic fields for the homogeneous, the on–site two–body, and the many–body cases corresponding to the dash–dotted, dashed, and solid lines, respectively. We use ^{40}K atoms near the Feshbach resonance at $B_0 = 202.1$G and with a filling fraction of 0.1. The on–site harmonic oscillator frequency ω is $2\pi \times 58275$Hz, which corresponds to a lattice with wavelength $\lambda = 806$nm and a Rabi frequency of $\Omega_{\rm R} = 2\pi \times 1.43$GHz. In the homogeneous case, the molecules become short lived resonances above B_0 and this is indicated by a dotted curve. The inset shows the two–particle continuum associated with the lowest Bloch band. The two–body binding energy crosses through twice the Fermi energy at $B \simeq 300G$, demonstrating that the BEC–BCS crossover occurs far from B_0. The upper curve in the inset corresponds to the hole–particle symmetric solution of the BCS gap equation.

clads the dressed molecules with many–body effects resulting in a change of the binding energy such that it only asymptotically reaches twice the Fermi energy at high magnetic fields, as shown by the solid line. Mathematically, this arises because the two–body pole at $3\hbar\omega$ in the self–energy of the molecules is replaced by the famous logarithmic BCS singularity at twice the Fermi level. By placing the system in an optical lattice, we thus find that the BEC–BCS crossover takes place rather far from the resonance. Consequently, as we shall show below, we may always use the single–band approximation to describe the BEC–BCS crossover for all experimentally relevant Feshbach resonances.

6.2 BEC–BCS crossover theory in the lattice

We now begin with an outlay of our general BEC–BCS crossover theory in the lattice before discussing the specific case of ^{40}K. The second–quantized grand–canonical Hamiltonian in the presence of an optical lattice potential $V(\mathbf{x})$ is

$$\begin{aligned} H = &\int d\mathbf{x}\, \psi_{\mathrm{m}}^{\dagger}(\mathbf{x}) \left(-\frac{\hbar^2\nabla^2}{4m} + \delta - 2\mu + 2V(\mathbf{x}) \right) \psi_{\mathrm{m}}(\mathbf{x}) \\ &+ \sum_{\sigma=\uparrow,\downarrow} \int d\mathbf{x}\, \psi_{\sigma}^{\dagger}(\mathbf{x}) \left(-\frac{\hbar^2\nabla^2}{2m} - \mu + V(\mathbf{x}) \right) \psi_{\sigma}(\mathbf{x}) \\ &+ g \int d\mathbf{x} \left(\psi_{\mathrm{m}}^{\dagger}(\mathbf{x}) \psi_{\uparrow}(\mathbf{x}) \psi_{\downarrow}(\mathbf{x}) + \psi_{\downarrow}^{\dagger}(\mathbf{x}) \psi_{\uparrow}^{\dagger}(\mathbf{x}) \psi_{\mathrm{m}}(\mathbf{x}) \right), \end{aligned} \tag{6.1}$$

where $\psi_{\sigma}(\mathbf{x})$ are the atomic and $\psi_{\mathrm{m}}(\mathbf{x})$ the molecular annihilation operators, and μ is the chemical potential. The atom–molecule coupling is given by $g = \hbar\sqrt{4\pi a_{\mathrm{bg}} \Delta B \Delta\mu_{\mathrm{mag}}/m}$, where a_{bg} is the background scattering length, ΔB is the width of the Feshbach resonance, $\Delta\mu_{\mathrm{mag}}$ is the difference in magnetic moments between the closed and open channels of the Feshbach resonance, and m is the atomic mass [115,118]. The detuning from resonance is $\delta = \Delta\mu_{\mathrm{mag}}(B - B_0)$, where B_0 is the value of the magnetic field B at the resonance. It gives the location of the bare molecular level with respect to the atomic continuum in the absence of the lattice.

With a lattice potential present, we turn to a description in terms of Bloch bands since plane wave states no longer diagonalize the Hamiltonian. Summing the effects of nearest–neighbour tunneling leads to a dispersion in the lowest band of the optical lattice equal to $\varepsilon(\mathbf{k}) = -2t^{\mathrm{a}}[\cos(k_x\lambda/2) + \cos(k_y\lambda/2) + \cos(k_z\lambda/2)] + 3\hbar\omega/2$, with λ the wavelength of the lattice laser and $3\hbar\omega/2$ the on–site, ground–state energy of a single atom. The atomic and molecular tunneling amplitudes are given by

$$t_{\mathrm{a,m}} = 4 \left(\frac{V_0^3 E_{\mathrm{a,m}}^{\mathrm{R}}}{\pi^2} \right)^{\frac{1}{4}} \exp\left(-2\sqrt{\frac{V_0}{E_{\mathrm{a,m}}^{\mathrm{R}}}} \right), \tag{6.2}$$

where V_0 is the peak–to–trough depth of the optical lattice potential and the atomic and molecular recoil energies are $E_{\mathrm{a}}^{\mathrm{R}} = 2(\pi\hbar)^2/m\lambda^2$ and $E_{\mathrm{m}}^{\mathrm{R}} = E_{\mathrm{a}}^{\mathrm{R}}/2$. Moreover, the effective on–site atom–molecule coupling $g_b^2 = g^2 \int d\mathbf{x} |\chi_b(\mathbf{x})|^4$ becomes band–dependent, where $\chi_b(\mathbf{x})$ is the Wannier function in band $b = 0, 1, 2, \ldots$ of the optical lattice. In the lowest

band, we write this effective coupling as $g' \equiv g_0 = g/(2\pi l^2)^{3/4}$ where $l = \sqrt{\hbar/m\omega}$ is the on–site harmonic oscillator length [66].

Obtaining pertinent thermodynamic quantities for this system involves the calculation of the molecular self–energy. We obtain this self–energy by first integrating the fermions out of the partition function exactly. We then perform an RPA or Bogoliubov approximation around the mean field $\Delta = g'\langle\psi_{\rm m}\rangle \equiv g'\sqrt{n^{\rm B}_{\rm mc}}$ of the bare molecular condensate. This approach is known to work well in the zero–temperature limit considered here [119]. In the on–site two–body limit, we have $t_{\rm a} = 0$ and $\Delta = 0$, leaving dispersionless harmonic oscillator bands with energies $\varepsilon_b = (b + 3/2)\hbar\omega$. The two–body molecular self–energy then becomes $\hbar\Sigma(E) = g'^2\sqrt{\pi}G(E - 3\hbar\omega)/\hbar\omega$ where the analytic sum over dispersionless bands is encapsulated in the function [120] $G(E) \equiv \Gamma(-E/2\hbar\omega)/\Gamma(-E/2\hbar\omega - 1/2)$. The binding energy of the dressed molecules is then found from $E = \delta + 3\hbar\omega/2 + \hbar\Sigma(E)$.

In the many–body case, where $t_{\rm a}$, $t_{\rm m}$, and Δ are all nonzero in general, we work in a regime where the temperature is sufficiently below the Fermi temperature that we may use a zero–temperature approximation. Due to the large band gap in a deep optical lattice, the structure of all bands but the lowest has a negligible effect and they can be taken to be dispersionless, as in the two–body case. However, they can not be excluded altogether from calculations since, as we have just witnessed, they renormalize the two–body energy levels. The BCS dispersion relation of the fermions is now $\hbar\omega(\mathbf{k}) = \sqrt{(\varepsilon(\mathbf{k}) - \mu)^2 + |\Delta|^2}$ and we can write the normal and anomalous molecular self–energies in terms of the usual coherence factors of BCS theory $|u(\mathbf{k})|^2 = [\hbar\omega(\mathbf{k}) + \varepsilon(\mathbf{k}) - \mu]/2\hbar\omega(\mathbf{k})$ and $|v(\mathbf{k})|^2 = [\hbar\omega(\mathbf{k}) - (\varepsilon(\mathbf{k}) - \mu)]/2\hbar\omega(\mathbf{k})$ to obtain

$$\hbar\mathbf{\Sigma}_{11}(\mathbf{k}, i\omega_n) = \frac{g'^2\sqrt{\pi}G(E)}{\hbar\omega} - \frac{g'^2}{i\hbar\omega_n - 3\hbar\omega + 2\mu} + \frac{g'^2}{N_{\rm S}}\sum_{\mathbf{k}'}\left\{\frac{|u(\mathbf{k}_+)|^2|u(\mathbf{k}_-)|^2}{i\hbar\omega_n - \hbar\omega(\mathbf{k}_+) - \hbar\omega(\mathbf{k}_-)} - \frac{|v(\mathbf{k}_+)|^2|v(\mathbf{k}_-)|^2}{i\hbar\omega_n + \hbar\omega(\mathbf{k}_+) + \hbar\omega(\mathbf{k}_-)}\right\}, \tag{6.3}$$

$$\hbar\mathbf{\Sigma}_{12}(\mathbf{k}, i\omega_n) = \frac{2g'^2}{N_{\rm S}}\sum_{\mathbf{k}'} u(\mathbf{k}_+)v(\mathbf{k}_+)u(\mathbf{k}_-)v(\mathbf{k}_-) \times \frac{\hbar\omega(\mathbf{k}_+) + \hbar\omega(\mathbf{k}_-)}{[\hbar\omega(\mathbf{k}_-) + \hbar\omega(\mathbf{k}_+)]^2 + \hbar^2\omega_n^2}, \tag{6.4}$$

where $\mathbf{k}_\pm = \mathbf{k}' \pm \mathbf{k}/2$, $E = i\hbar\omega_n + 2\mu - 3\hbar\omega$, $N_{\rm S}$ is the total number of

lattice sites and the sums are over the first Brillouin zone only: $k'_x, k'_y, k'_z \in (-2\pi/\lambda, 2\pi/\lambda)$. An equation for the BCS gap Δ is then found in the form of a Hugenholtz–Pines relation

$$2\mu = \delta + \frac{3\hbar\omega}{2} - 6t^{\mathrm{m}} + \hbar\mathbf{\Sigma}_{11}(\mathbf{0}, 0) - \hbar\mathbf{\Sigma}_{12}(\mathbf{0}, 0). \tag{6.5}$$

Having these quantities in hand enables us to determine the partition function of the system from the Gaussian effective action of our RPA theory and, via the resulting thermodynamic potential Ω, we can calculate the total number of particles using the identity $N = -\partial\,\Omega/\partial\,\mu$. This leads to the equation of state for the total atomic filling fraction $n = N/N_{\mathrm{S}}$ given by

$$n = \mathrm{Tr}\,[\tau_3 \mathbf{G}_{\mathrm{BCS}}] + 2\frac{|\Delta|^2}{g'^2} - \mathrm{Tr}\,[\mathbf{G}_{\mathrm{m}}] + \frac{1}{2}\,\mathrm{Tr}\left[\mathbf{G}_{\mathrm{m}}\frac{\partial\,\hbar\mathbf{\Sigma}}{\partial\,\mu}\right], \tag{6.6}$$

where τ_3 is the third Pauli matrix and the 2×2 Nambu space matrices $\mathbf{G}_{\mathrm{BCS}}$, $\mathbf{G}_{\mathrm{m}}$ and $\mathbf{\Sigma}$ are the BCS atomic Greens function, the molecular Greens function, and self–energy matrix composed of Eqs. (6.3) and (6.4) respectively.

6.3 Results and discussion

Although our approach is quite general, the numerical calculations in this paper are for the $B_0 = 202.1$G Feshbach resonance of ^{40}K atoms, which has a width of $\Delta B = 7.8$G [36], and for a total filling fraction of 0.1 as an illustrative and experimentally relevant case. For every δ, solving the BCS gap equation, Eq. (6.5), and the equation of state simultaneously yields self–consistent values for μ and the filling fraction of the bare molecular condensate $n^{\mathrm{B}}_{\mathrm{mc}} = \Delta^2/g'^2$. Since fluctuation effects are expected to be less important away from resonance, in the first instance we neglect the fluctuation contribution reflected by the last two terms on the right–hand side of Eq. (6.6). In order to examine $n^{\mathrm{B}}_{\mathrm{mc}}$, it proved requisite to include the structure of the higher bands to which intermediate states strongly couple in the neighbourhood of the Feshbach resonance. Having done so, the many–body result monotonically approaches the 2–body limit in the resonant region as more bands are included in the self–energy calculation. This is clear from Fig. 6.2. When including higher bands, we used a multiband generalization of Eqs. (6.3) and (6.4) that did not factor in any

interband coupling other than the already present interaction of the mean field $\Delta_b = g_b\langle\psi_{\rm m}\rangle$ with the molecular condensate. Although this leads to only qualitative results in the higher bands, the correct two–body physics is obtained and the importance of multiband effects near resonance is well demonstrated.

We also determine the filling fraction of Bose–Einstein condensed dressed molecules as this will provide us with another good indication of where the crossover from a Bose–Einstein condensate of dressed molecules to the BCS state composed of Bose–Einstein condensed Cooper pairs takes place. This fraction is given by $n_{\rm mc} = n_{\rm mc}^{\rm B}/Z$, where Z is the so–called wavefunction renormalisation factor which determines the probability amplitude for the dressed molecular wavefunction to be in the bare molecular state [115]. This is plotted in the inset of Fig. 6.3. For this purpose, we did not calculate the true many–body Z, which would involve the full fluctuation calculation [119], but used instead the 2–body wavefunction renormalisation factor given by $Z^{\rm 2B} = 1/(1 - \partial\,\hbar\Sigma(E)/\,\partial\,E)$, where $\hbar\Sigma(E)$ is the two–body self–energy discussed earlier. This results in an upper bound

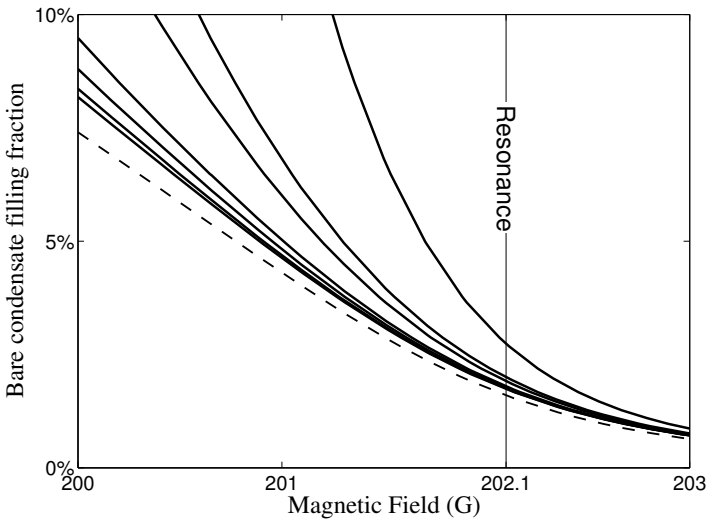

Figure 6.2: The filling fraction of the bare molecular condensate, $n_{\rm mc}^{\rm B}$, drawn as solid lines, decreases monotonically to the two–body limit as progressively more bands are included, from 1 to 300 in this case. The dashed line is $Z^{\rm 2B}$, which is equivalent to the filling fraction of the molecular condensate in the BEC region shown here.

for $n_{\rm mc}$, owing to the fact that $Z^{\rm 2B}$ is always smaller than its many–body

counterpart Z. The magnetic field region where this dressed filling fraction decreases from one to zero indicates the position of the BEC–BCS crossover, which is clearly in the same neighbourhood as where the two–body molecular energy enters the Fermi sea. From the inset in Fig. 6.3, we see that the BEC–BCS crossover is dominated by contributions from the lowest band only; including higher bands in the self–energy calculation does not bring about any apparent change.

In Fig. 6.3 we compare Z^{2B} with $2n^{B}_{mc}/n$. Indeed, $2n^{B}_{mc}/n$ and Z^{2B} are similar in the BEC limit, since the gas then consists solely of a Bose–Einstein condensate of dressed molecules. This is a result of the fact that in this regime the energies of the atomic states lie far above the dressed molecular state, as seen in Fig. 6.1, which suppresses many–body effects. The BCS region, however, sees a pronounced difference between the two–body renormalisation factors and the bare molecular condensate fraction.

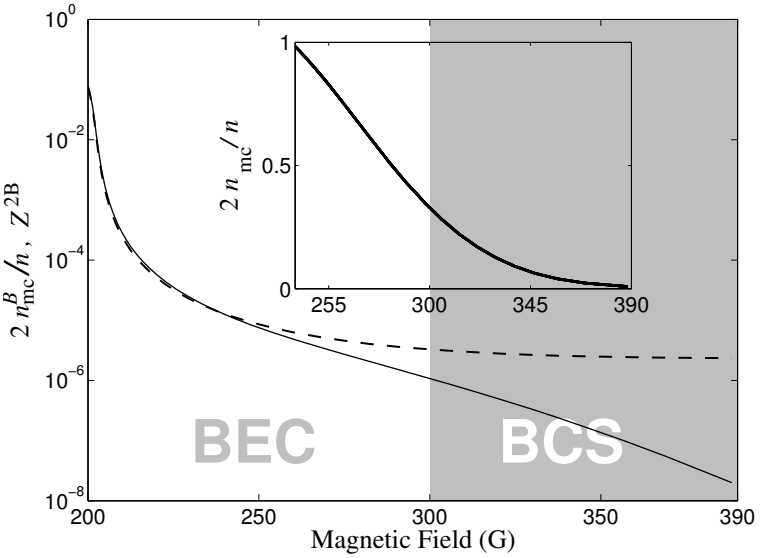

Figure 6.3: Two–body wavefunction renormalisation factor Z^{2B} (dashed line) plotted together with the filling fraction of the bare molecular condensate $2n^{B}_{mc}/n$ including a varying number of bands (solid lines), which shows that a single–band calculation is adequate in the BEC–BCS crossover region of interest. The inset shows the approximate filling fraction of dressed molecules, $2n_{mc}/n$, in the crossover region. The multiple solid lines of the main graph all lie on top of each other in this high magnetic field region.

Our solutions of the BCS gap equation confirm the presence of the logarithmic BCS singularity arising at high detuning where the gap then scales as $\Delta \simeq 2t^{\sigma} \exp(-29\, t^{\sigma}/|U_{\rm eff}|)$ [111]. Here, $U_{\rm eff} \simeq -g'^2/(\delta + 3\hbar\omega - 2\mu)$, is the on–site Hubbard attraction of the atoms. In the crossover region, the molecular energy crosses the lowest–band boundary when $\delta \simeq g'^2/12t_{\rm a}$. Furthermore, $U_{\rm eff}$ indicates this crossing occurs close to a Feshbach resonance when $\delta \simeq 3\hbar\omega/2$. This leads to the criterion $\Delta B \gg 18t_{\rm a}\sqrt{4\pi\hbar/m\omega}/a_{\rm bg}\Delta\mu_{\rm mag}$ which ensures that the Feshbach resonance and the BEC–BCS crossover are well separated, as required for the applicability of a single–band model to the BEC–BCS crossover in an optical lattice. Most known Feshbach resonances adhere to this criterion.

In conclusion, we have presented the full microscopic many–body theory that describes the BEC–BCS crossover in an optical lattice due to the presence of a Feshbach resonance. Both two–channel physics and the possible effects of higher bands were taken into account. We have shown that in general the BEC–BCS crossover takes place far from the Feshbach resonance, such that a single–band model suffices to accurately describe the BEC–BCS crossover. The many–body Z can only be obtained from the full fluctuation calculation and this is an important topic of further study.

Acknowledgements

We would like to thank Mathijs Romans, Michiel Snoek, and Usama Al Kahwaja for helpful discussions. This work is supported by the Stichting voor Fundamenteel Onderzoek der Materie (FOM) and the Nederlandse Organisatie voor Wetenschaplijk Onderzoek (NWO).

7

A strongly interacting Bose gas: Nozières and Schmitt-Rink theory and beyond

We calculate the critical temperature for Bose-Einstein condensation in a gas of bosonic atoms across a Feshbach resonance, and show how medium effects at negative scattering lengths give rise to pairs reminiscent of the ones responsible for fermionic superfluidity. We find that the formation of pairs leads to a large suppression of the critical temperature. Within the formalism developed by Nozières and Schmitt-Rink the gas appears mechanically stable throughout the entire crossover region, but when interactions between pairs are taken into account we show that the gas becomes unstable close to the critical temperature. We discuss prospects of observing these effects in a gas of ultracold ^{133}Cs atoms where recent measurements indicate that the gas may be sufficiently long-lived to explore the many-body physics around a Feshbach resonance.

7.1 Introduction

In a Fermi gas there exists a smooth crossover connecting two apparently distant states, namely, the Bardeen-Cooper-Schrieffer (BCS) state which is found for weakly attractive interactions and the Bose-Einstein condensed (BEC) state of diatomic molecules obtained for weakly repulsive effective

This chapter has been previously published as *A strongly interacting Bose gas: Nozières and Schmitt-Rink theory and beyond*, Arnaud Koetsier, P. Massignan, R. A. Duine, and H. T. C. Stoof, Phys. Rev. A **79,** 063609 (2009).

interactions [121,122]. This crossover between a superfluid of loosely bound pairs of fermions and a condensate of tightly bound dimers takes place in the vicinity of a Feshbach resonance, where the effective interaction changes from attractive to repulsive through a divergence of the coupling constant. What lies at the heart of this continuous crossover is the fact that a pair of fermions makes up a boson which is bound either by two-body effects in the BEC limit or by many-body effects in the BCS limit. It is this composite boson that undergoes Bose-Einstein condensation.

While fermions can condense only in the form of pairs, bosons can condense solitarily. A Bose gas at low temperatures is therefore subject to a competition between the condensation of atoms and of pairs. Pairing in a bosonic gas leads either to the formation of tightly bound molecules which are stable even in the vacuum, or to the creation of loosely bound pairs stabilized by the medium. The latter are reminiscent of Cooper pairs arising in BCS superconductivity. In this article we investigate the properties of a Bose gas near a Feshbach resonance and address important issues regarding stability of such a strongly interacting Bose gas.

The BEC-BCS crossover for fermions has been recently explored in a series of ground breaking experiments with ultracold alkaline gases [36,123] by exploiting so-called Feshbach resonances which enable the interaction strength to be tuned. By contrast, early experimental attempts to create strongly interacting bosonic gases have been plagued by large losses [124]. This is primarily because inelastic collisions provoking the decay of pairs into deeply bound states increase rapidly in the neighborhood of a resonance of the s-wave scattering length a. The decay imparts a kinetic energy to the products that is in general much larger than the confining potential, causing atoms to escape from the trap. Moreover, attractive atomic interactions may induce a mechanical instability at sufficiently large densities resulting in the collapse of the gas [125]. Both problems do not arise with fermions due to the stabilizing effects of Pauli blocking [107].

However, in recent experiments a gas of $6s$ molecules composed of bosonic ^{133}Cs atoms was observed to have relatively small inelastic losses [126, 127]. This stability against decay offers the intriguing possibility of experimentally realizing a molecular BEC with bosonic atoms and of studying the BEC-BCS crossover in a bosonic gas.

The paper is organized as follows. In Sec. 7.2 we demonstrate that a crossover exists in the case of bosons that is analogous to the BEC-BCS crossover occurring in Fermi gases. We show that the compressibility ob-

tained within the Nozières and Schmitt-Rink (NSR) formalism [106] is positive throughout the normal phase, indicating that the gas may be mechanically stable. However, attractive interactions beyond the NSR formalism between long-lived preformed pairs of bosons can mechanically destabilize the gas and the elucidation of this effect is the subject of Sec. 7.2.2. In Sec. 7.3 we discuss the experimental feasibility of observing such a crossover in ^{133}Cs, and present our conclusions in Sec. 7.4.

7.2 Universal phase diagram

In principle, a two-channel model is required to completely describe a Feshbach resonance [115]. However, sufficiently close to the resonance, a single-channel description which lends itself to the NSR formalism suffices. The phase diagram describing the transition from the normal state of a bosonic gas with density n to the condensed state of either atoms or pairs is then universal, in the sense that it depends only on a single interaction parameter, namely, the total scattering length a divided by the average interparticle spacing $n^{-1/3}$. In the limit $n^{1/3}a \to 0^-$, atoms condense at the critical temperature for an ideal gas $T_a = (2\pi\hbar^2/mk_{\mathrm{B}})[n/\zeta(3/2)]^{2/3}$, where n is the total atomic density. In the opposite limit $n^{1/3}a \to 0^+$ there exists a deep two-body bound state, and atoms bind into dimers which condense at the lower temperature $T_{\mathrm{m}} = T_a/2^{5/3}$. Within a simple two-body approximation (dashed line in Fig. 7.1), we find a critical temperature for pair condensation T_c that quickly interpolates between these two limits. However, within the NSR many-body approach (solid line in Fig. 7.1) we find that T_c is strongly suppressed on the attractive side of the resonance. As we will see in the following, this suppression is due to the population of a low-energy resonant two-body state brought about by many-body effects. This is in many ways reminiscent of what occurs in superconductors, where electrons in a medium pair up below a critical temperature in the presence of an attractive interaction. While in the fermionic case the critical temperature falls to zero exponentially, we find that here T_c reaches its limiting value T_a according to a power law [1]. Within the NSR approach, the gas is found to be stable in the normal phase at all temperatures down to the critical temperature T_c. In Sec. 7.2.2 we will see that inclusion of molecule-molecule interactions leads to a critical temperature that is higher than the NSR result, and in the region close to the resonance the gas acquires a negative compressibility at temperatures close to T_c.

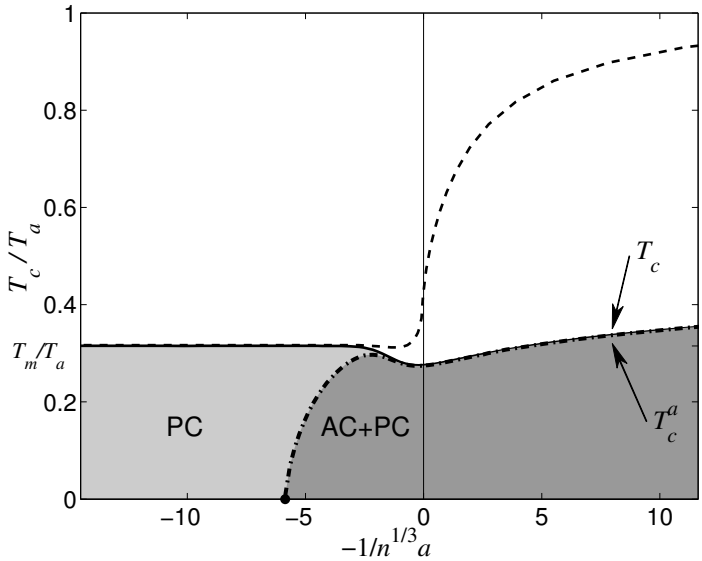

Figure 7.1: Universal phase diagram for bosons as a function of the interaction parameter $1/n^{1/3}a$ where n is the total density of atoms. The solid line shows T_c calculated within the NSR formalism, while the dashed line is the two-body result. The dash-dotted line is the critical temperature T_c^a for the condensation of unpaired bosons in units of the critical temperature T_a of an ideal atomic gas. The phase with a pair condensate (PC), which lies between T_c and T_c^a, extends all the way to $-1/n^{1/3}a = +\infty$. Both an atomic condensate and a pair condensate (AC+PC) exist below T_c^a.

7.2.1 NSR calculation

The results from the NSR formalism are summarized in Fig. 7.1 which shows the critical temperatures T_c and T_c^a for the Bose-Einstein condensation of paired and unpaired bosons, respectively. The critical temperature and the pressure of the gas was calculated within the grand canonical ensemble by introducing the thermodynamic potential Ω of a gas of particles of mass m at temperature T. The pressure and the density of the gas are related to Ω by $P = -\Omega/V$ and $n = -(1/V)\partial\Omega/\partial\mu$ respectively, where V is the volume and μ the chemical potential. Following NSR, we write Ω as [106]

$$\Omega = \frac{1}{\beta}\sum_{\mathbf{k}} \ln[1 - \exp(-\beta\xi_{\mathbf{k}})] + \frac{1}{\beta}\sum_{n,\mathbf{k}} \ln \frac{T^{2\mathrm{B}}(0)}{T(\mathbf{k}, i\omega_n)}. \tag{7.1}$$

The first term is the contribution of an ideal gas of atoms with $\xi_{\mathbf{k}} = \hbar^2\mathbf{k}^2/2m - \mu$ and $\beta = 1/k_{\mathrm{B}}T$. The second term (rederived in Sec. 7.2.2) represents the contribution of paired atoms where $\omega_n = 2\pi n/\hbar\beta$ are the even Matsubara frequencies and the two-body T-matrix is given by

$$T^{2\mathrm{B}}(z) = \frac{4\pi\hbar^2 a}{m}\frac{1}{1 - a\sqrt{-zm/\hbar^2}}, \tag{7.2}$$

where z is the energy in the centre-of-mass frame. The instability towards pair condensation is signaled by the appearance of a pole in the T-matrix at $\mathbf{k} = \mathbf{0}$ and $i\omega_n = 0$, which is the Thouless criterion [128]. Neglecting many-body effects in the first instance, we take $T(\mathbf{k}, i\omega_n) = T^{2\mathrm{B}}(z)$ with $z \equiv z(\mathbf{k}, i\omega_n) = i\hbar\omega_n + 2\mu - \hbar^2\mathbf{k}^2/4m$. This two-body result is plotted as a dashed line in Fig. 7.1.

To include many-body effects, we take $T(\mathbf{k}, i\omega_n) = T^{\mathrm{MB}}(\mathbf{k}, i\omega_n)$, where the many-body T-matrix is [129]

$$T^{\mathrm{MB}}(\mathbf{k}, i\omega_n) = \frac{1}{[T^{2\mathrm{B}}(z)]^{-1} - \Xi(\mathbf{k}, i\omega_n)}. \tag{7.3}$$

Here, the renormalized correlation function in the particle-particle channel $\Xi(\mathbf{k}, i\omega_n)$ is given by

$$\Xi(\mathbf{k}, i\omega_n) = \frac{1}{V}\sum_{\mathbf{q}} \frac{N(\xi_{\mathbf{k}/2+\mathbf{q}}) + N(\xi_{\mathbf{k}/2-\mathbf{q}})}{i\hbar\omega_n - \xi_{\mathbf{k}/2-\mathbf{q}} - \xi_{\mathbf{k}/2+\mathbf{q}}}, \tag{7.4}$$

with the Bose factor $N(x) = (e^{\beta x} - 1)^{-1}$. Within this formalism, the Thouless criterion for condensation yields the solid line in Fig. 7.1.

The strong suppression of T_c for negative scattering lengths can be understood from the spectral function for the pairs which is proportional to $\mathrm{Im}[T(\mathbf{k}, \omega + i0)]$ and is plotted in Fig. 7.2. The many-body spectral function (solid line) acquires a narrow peak near zero energy in the continuum. For small momenta, a delta-function is also present just below the continuum that is associated with the presence of infinite-lifetime pairs (not shown). Both features are notably absent from the two-body spectral function (dashed line) [115,130], and enhance the density of states for pairs at low energy leading to a reduction of T_c compared to the two-body case. In addition, populating these many-body resonances reduces the atomic density thereby reducing the atomic condensation temperature T_c^a. The inset shows the binding energy at T_c of the two-body bound state in the

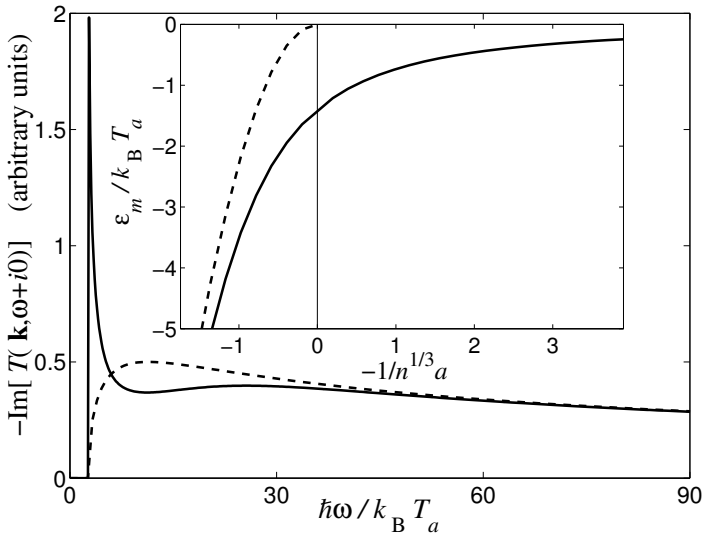

Figure 7.2: Spectral function of a pair evaluated at $1/n^{1/3}a = 2.18$, $T = T_c$ and $|\mathbf{k}| \simeq 0$. The two-body (dashed) and many-body (solid) calculations agree at high energy, but differ substantially at low energy. Also, a delta-function is present at positive frequency just below the continuum in the many-body case (not shown). At $|\mathbf{k}| = 0$ this delta function corresponds to the Thouless pole at $\omega = 0$. Inset: binding energy of a pair at $T = T_c$. The dashed line is the ideal gas limit $\varepsilon_m = -\hbar^2/ma^2$, while the solid line is the NSR result given by $\varepsilon_m = 2\mu$.

presence of the medium (solid line) which approaches the two-body result (dashed line) as $a \to 0^+$. For $a < 0$ there is no bound state in the vacuum, and the binding energy in the medium is that of the pair associated with the delta-function in the spectral function.

The pressure of the gas in the normal phase is plotted in Fig. 7.3 as a function of density up to the critical density for pair condensation which is denoted by a dot terminating the lines. We show results for $n^{1/3}a \simeq 0^+$, at resonance, and for $n^{1/3}a \simeq 0^-$. As expected, in the low density limit the first curve reproduces the ideal gas law for atoms ($P = nk_BT$), while the last yields the corresponding relation for molecules ($P = nk_BT/2$). We see that the compressibility ($= n^{-1}\partial n/\partial P$) calculated within the NSR approach is always positive, implying that the gas in its normal phase remains mechanically stable throughout the whole crossover.

Below T_c, bosons initially condense in the form of pairs [131] and this region is denoted by PC in the phase diagram. Interactions between pairs

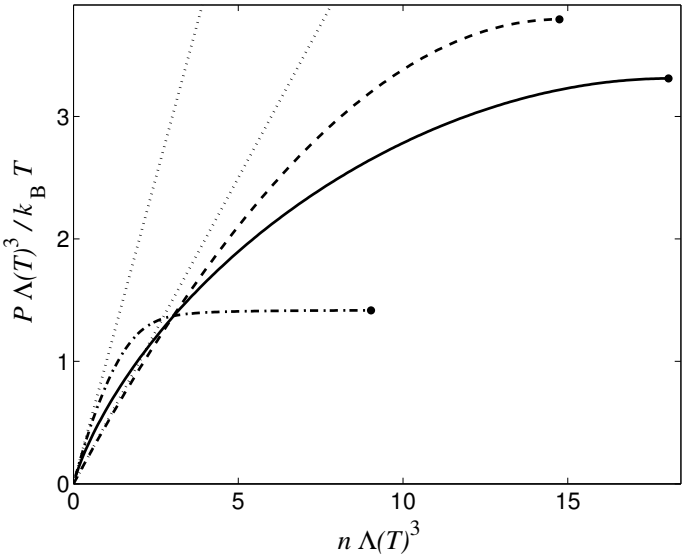

Figure 7.3: The pressure of the gas in its normal phase as a function of density in the NSR formalism for $-1/n^{1/3}a \simeq -10^3$ (dashed), 0 (solid), and 10^3 (dashed-dotted). Here, $\Lambda(T) = \sqrt{2\pi\hbar^2/mk_BT}$ is the thermal de Broglie wavelength. The dotted lines are the ideal gas law for atoms and molecules.

are neglected within the NSR formalism, and below T_c we therefore have an ideal Bose-Einstein condensate of pairs. The Thouless criterion is then always satisfied but the total number of atoms found from Eq. (7.1) is too small. This is because the number equation misses a nonzero pair-condensate contribution n_c which emerges as a result of a zero-momentum divergence connected to the Thouless pole of the many-body T-matrix. For $T < T_c$ it is

$$n_c = \hbar \frac{N(0)}{V} \frac{\partial T^{\rm MB}(\mathbf{0},0)}{\partial \mu} \left(\frac{\partial T^{\rm MB}(\mathbf{0},0)}{\partial i\omega_n} \right)^{-1} . \tag{7.5}$$

The pair condensate is characterized by the BCS order parameter $\Delta_0 \equiv \langle \Delta(\mathbf{x},\tau) \rangle = V_0 \langle \psi(\mathbf{x},\tau)\psi(\mathbf{x},\tau) \rangle \neq 0$ and $\langle \psi(\mathbf{x},\tau) \rangle = 0$. Here $\Delta(\mathbf{x},\tau)$ is the pairing field, V_0 is the bare atomic interaction and $\psi(\mathbf{x},\tau)$ is the atomic field. Noting that the Fourier transform of the BCS Green's function $G_\Delta(\mathbf{x},\tau;\mathbf{x}',\tau') = -\langle \Delta(\mathbf{x},\tau)\Delta^*(\mathbf{x}',\tau') \rangle$ can be written in terms of the many-body T-matrix as $G_\Delta(\mathbf{k},i\omega_n) = 2\hbar T^{\rm MB}(\mathbf{k},i\omega_n)$ [125], we find an expression for the order parameter $|\Delta_0|^2 = -\sum_n G_\Delta(\mathbf{0},i\omega_n)/\hbar\beta V$ in terms

of the many-body T-matrix

$$|\Delta_0|^2 = \frac{2\hbar N(0)}{V}\left[\frac{\partial}{\partial i\omega_n}\frac{1}{T^{\mathrm{MB}}(\mathbf{0},0)}\right]^{-1}. \tag{7.6}$$

Now, by comparing the divergences in Eqs. (7.5) and (7.6) we express the gap in terms of the condensate fraction as

$$|\Delta_0|^2 = 2n_c\left[\frac{\partial}{\partial\mu}\frac{1}{T^{\mathrm{MB}}(\mathbf{0},0)}\right]^{-1}. \tag{7.7}$$

Furthermore, the atomic dispersion in the pair condensate becomes a gapped Bogoliubov quasiparticle dispersion $\hbar\omega_{\mathbf{k}} = \sqrt{\xi_{\mathbf{k}}^2 - |\Delta_0|^2}$. Thus, condensation of atoms, signaled by $\langle\psi(\mathbf{x},\tau)\rangle$ becoming nonzero, takes place when the quasiparticle dispersion vanishes at zero momentum. The onset of atomic condensation is hence found as the temperature T_c^a at which $|\Delta_0| = -\mu$. This is the dash-dotted line in Fig. 7.1.

It is only at the temperature $T_c^a < T_c$ that an atomic condensate (AC) of solitary bosons appears, and coexists with the condensate of pairs. The phase transition separating the AC and AC+PC regions becomes an Ising-like quantum phase transition when $T_c^a = 0$ [132,133]. We find no point at which the three phases (normal, PC, AC+PC) meet, as T_c^a remains strictly smaller than T_c at any value of the scattering length.

7.2.2 Beyond NSR

Interactions between infinite-lifetime dimers corresponding to the positive frequency pole of the many-body T-matrix are neglected in the NSR theory presented above. In order to estimate the effect of these interactions in the normal phase, we add a mean-field shift $n_{\mathrm{m}}T_{\mathrm{mm}}$ to the binding energy of these infinite-lifetime dimers, and the corresponding additional interaction energy $Vn_{\mathrm{m}}^2T_{\mathrm{mm}}$ in the thermodynamic potential. Here, $T_{\mathrm{mm}} = 4\pi\hbar^2a_{\mathrm{mm}}/2m$ is the molecular T-matrix, a_{mm} is the dimer-dimer s-wave scattering length and n_{m} is the density of dimers that is the contribution of the pole in the T-matrix to the number equation.

To calculate the dimer-dimer scattering length, we begin by performing a Hubbard-Stratonovich transformation and subsequently integrate out the

atomic fields to obtain an effective action in terms of the pairing field

$$S^{\text{eff}}[\Delta,\Delta^*] = \frac{-1}{2V_0}\int_0^{\hbar\beta} d\tau \int d\mathbf{x}|\Delta(\mathbf{x},\tau)|^2 + \frac{\hbar}{2}\,\text{Tr}\,\left[\ln(-\mathbf{G}_0^{-1})\right] - \frac{\hbar}{2}\sum_{n=1}^{\infty}\frac{1}{n}\,\text{Tr}\,\left[(\mathbf{G}_0\mathbf{\Sigma})^n\right], \quad (7.8)$$

where the noninteracting Green's function is a 2×2 matrix in Nambu space given by

$$\hbar\mathbf{G}_0(\mathbf{x},\tau;\mathbf{x}',\tau')^{-1} = \begin{pmatrix} -\hbar\partial_\tau + \frac{\hbar^2\nabla^2}{2m} + \mu & 0 \\ 0 & \hbar\partial_\tau + \frac{\hbar^2\nabla^2}{2m} + \mu \end{pmatrix}\delta(\mathbf{x}-\mathbf{x}')\delta(\tau-\tau') \quad (7.9)$$

and the self-energy is

$$\hbar\mathbf{\Sigma}(\mathbf{x},\tau;\mathbf{x}',\tau') = \begin{pmatrix} 0 & \Delta(\mathbf{x},\tau) \\ \Delta^*(\mathbf{x},\tau) & 0 \end{pmatrix}\delta(\mathbf{x}-\mathbf{x}')\delta(\tau-\tau'). \quad (7.10)$$

The first term in Eq. (7.8) corresponds to the thermodynamic potential of a noninteracting gas that is the first term in Eq. (7.1). The BCS Green's function defined in the previous section is obtained from the terms in Eq. (7.8) that are quadratic in the pairing fields. They may be written as

$$S^{(2)}[\Delta,\Delta^*] = -\hbar\sum_{\mathbf{k},n}\Delta^*(\mathbf{k},i\omega_n)\frac{1}{2\hbar T^{\text{MB}}(\mathbf{k},i\omega_n)}\Delta(\mathbf{k},i\omega_n). \quad (7.11)$$

Neglecting all higher-order terms and performing the Gaussian functional integral yields the second term in Eq. (7.1), where the factor $T^{2\text{B}}(0)$ appears due to the normalization involved in the Hubbard-Stratonovich transformation.

By introducing the renormalized pairing field $\phi(\mathbf{k},i\omega_n) = \Delta(\mathbf{k},i\omega_n)/\sqrt{Z}$ with the renormalization factor

$$Z = \frac{2}{\hbar}\left[\frac{\partial}{\partial i\omega_n}\frac{1}{T^{\text{MB}}(\mathbf{0},\omega_{\mathbf{0}}^m)}\right]^{-1}, \quad (7.12)$$

where $\omega_{\mathbf{0}}^m$ is the frequency of the molecular pole in the many-body T-matrix at zero momentum, this quadratic action can be recast into the action for an ideal Bose gas

$$S^{(2)}[\phi,\phi^*] = \sum_{\mathbf{k},n}\phi^*(\mathbf{k},i\omega_n)(-i\hbar\omega_n + \hbar\omega_{\mathbf{k}}^m)\phi(\mathbf{k},i\omega_n). \quad (7.13)$$

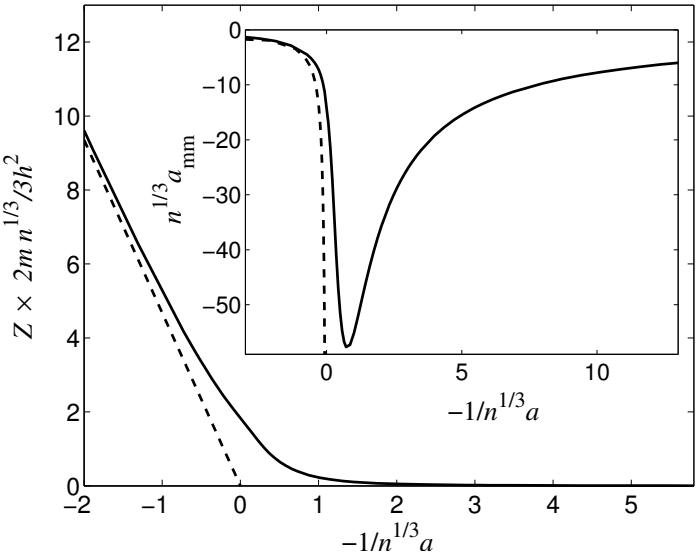

Figure 7.4: The renormalization factor Z (solid line). Inset: the dimer-dimer scattering length $a_{\rm mm}$ (solid line). The respective BEC limits which are recovered as $a \to 0^+$ are shown as dashed lines.

Lowest-order corrections to NSR due to interactions between pairs are then obtained from the fourth-order term of the effective action. Writing it as $S^{(4)}[\phi, \phi^*] \equiv (\hbar\beta V/2)|\phi_0|^4 T_{\rm mm}$, where $\phi_0 = \Delta_0/\sqrt{Z}$, we thereby find the molecule-molecule scattering length

$$a_{\rm mm} = \frac{\sqrt{2m^5}}{\hbar^5}\frac{Z^2}{32\pi^3}\left\{\frac{-\pi}{(-4\mu)^{\frac{3}{2}}} - 2\beta^2\int_{-\beta\mu}^{\infty} dx \frac{\sqrt{x/\beta+\mu}}{x^2}\frac{2}{e^x-1}\left[\frac{1}{x}+2+\frac{2}{(e^x-1)}\right]\right\}. \quad (7.14)$$

The integrand in Eq. (7.14) is sharply peaked about $x = 0$ thus in the BEC limit, where $Z = 16\pi\hbar^4/m^2 a$ and $\mu \simeq -\hbar^2/2ma^2$ is large and negative, the integral can be neglected and the molecule-molecule scattering length reduces to $a_{\rm mm} = -4a$. Note that this is the same result found in Ref. [133] up to a minus sign which was erroneously omitted there. Plots of $a_{\rm mm}$ and Z are shown in Fig. 7.4.

The critical temperature obtained by including mean-field effects due to the stable dimers is plotted as the solid line in Fig. 7.5, and is always higher

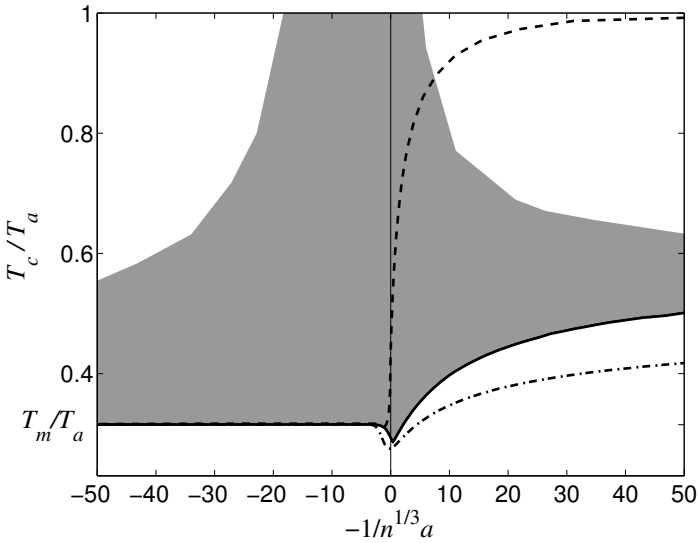

Figure 7.5: Universal phase diagram beyond NSR for the same parameters as in Fig. 7.1. The solid line is T_c computed including molecular interactions. The dashed-dotted and dashed lines are same many-body and two-body T_c results respectively shown in Fig. 7.1. The shading denotes the mechanical instability region.

than the critical temperature predicted within the NSR formalism (dashed-dotted line) owing to the presence of an attractive interaction between the stable dimers throughout the crossover. The pressure of the gas for densities below the critical density is shown in Fig. 7.6 at various atomic scattering lengths (solid lines). We see that the inclusion of molecule-molecule interactions gives rise to a region of negative compressibility, indicating a mechanical instability at temperatures above the critical temperature. The shading in Fig. 7.5 denotes the resulting unstable region with an upper boundary given by the temperature for which $\partial n/\partial P = 0$. A striking feature of this phase diagram is the presence of a mechanically stable region at negative scattering lengths, where the gas remains in the normal phase far below the ideal gas critical temperature due to the many-body effects discussed above.

The effects of screening of the interatomic interaction may be estimated by dressing the atomic interaction in the many-body T-matrix with an

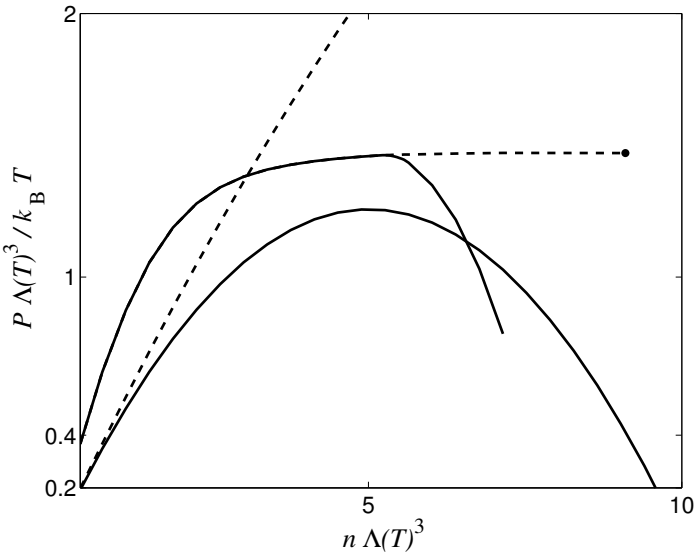

Figure 7.6: The pressure of the gas in the NSR formalism (dashed lines) and with molecular interactions beyond NSR included (solid lines). The curves beginning at $P\Lambda(T)^3/k_BT = 0.2$ and 0.4 correspond to $-1/n^{1/3}a \simeq 10^{-3}$ and 10^3, respectively.

RPA bubble sum,

$$T^{\mathrm{MB}}(\mathbf{k}, i\omega_n) = \frac{1}{[T^{2\mathrm{B}}(z)]^{-1} - \Pi(\mathbf{0}, 0) - \Xi(\mathbf{k}, i\omega_n)}, \tag{7.15}$$

where

$$\Pi(\mathbf{0}, 0) = -\frac{4}{\hbar^2 \beta V} \sum_{\mathbf{k}, n} G(\mathbf{k}, i\omega_n)^2 \tag{7.16}$$

and $G(\mathbf{k}, i\omega_n) = \hbar/(i\hbar\omega_n - \xi_{\mathbf{k}})$. We have estimated that this correction raises the critical temperature by less than 15% on the BCS side (see Appendix D). The phase diagram obtained within a more refined calculation which includes screening fully self-consistently is beyond the scope of this paper but should therefore not deviate substantially from the one presented here.

7.3 Cesium phase diagram

We now turn our attention to the specific case of a gas of ^{133}Cs atoms near the narrow s-wave Feshbach resonance due to a d-wave molecule located at

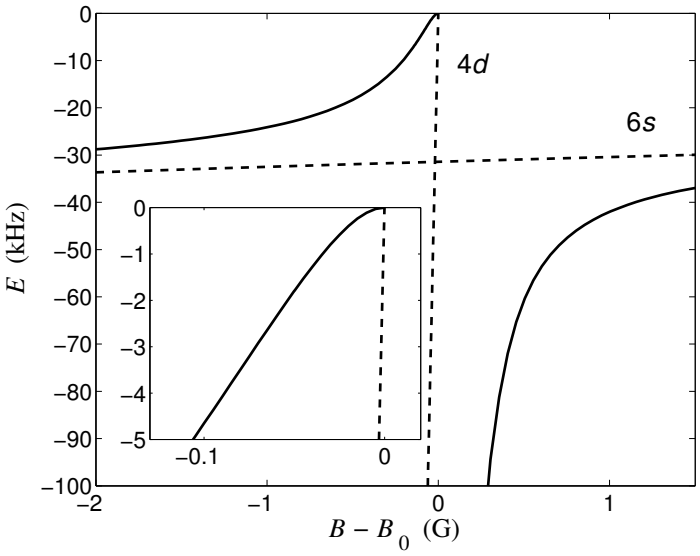

Figure 7.7: Binding energy of the $6s$ and $4d$ bare states (dashed lines) giving rise to the avoided crossing between the two dressed states (solid lines). In the close-up we show the Wigner threshold behavior of the binding energy near the continuum.

$B_0 = 47.78$ G [134]. The shallow $6s$ bound state where small inelastic losses were experimentally observed is present just below the atomic continuum and should be taken into account since it crosses the $4d$ state that causes the Feshbach resonance. Thus, the two-body T-matrix for the ^{133}Cs s-wave Feshbach resonance considered here is obtained from Eq. (7.2) by replacing a with $a_{\rm bg}(B)[1 + \Delta\mu\Delta B/(z - \delta)]$ [115, 135, 136]. Here, the difference of magnetic moments between the $4d$ bound state and the atomic continuum is $\Delta\mu = 1.15\mu_B$ [134], and $a_{\rm bg}(B)$ is the background scattering length [2]. The energy detuning from the Feshbach resonance is defined as $\delta = \Delta\mu(B - B_0)$ and the width of the resonance is found to be $\Delta B = 0.16$ G [134].

The energy of the poles of the cesium two-body T-matrix are plotted as solid lines in Fig. 7.7 which shows the avoided crossing between the $4d$ and $6s$ states. The binding energies of the bare states are shown as dashed lines. Also shown is a close-up near the Feshbach resonance showing the Wigner threshold behavior of the binding energy that is characteristic of an s-wave resonance. This mirrors the behavior of the binding energy in the

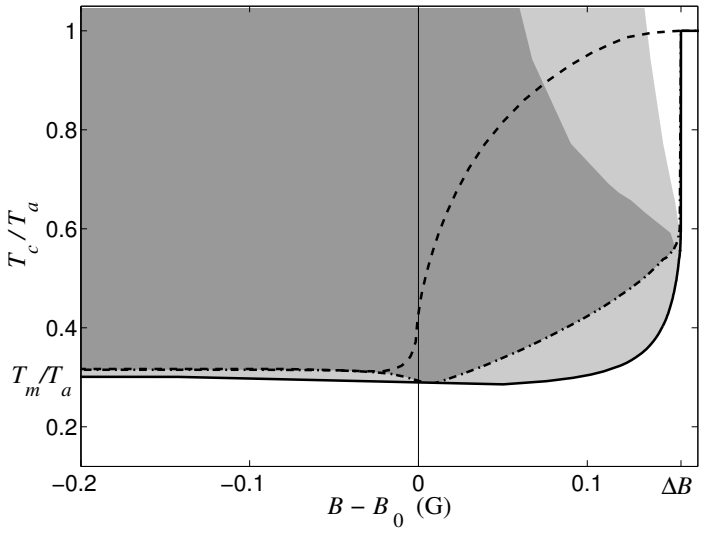

Figure 7.8: Critical temperature for pair condensation T_c in a gas of ^{133}Cs for particle densities $n = 10^{11}\text{cm}^{-3}$ (dash-dotted) and 10^{14}cm^{-3} (solid), and the corresponding instability regions (dark and light grey, respectively). For $n = 10^{14}\text{cm}^{-3}$ we have T_a=79 nK and T_m=25 nK. Note that the curve has no kink at $B - B_0 = \Delta B = 0.16G$ although this is not visible on this scale. The dashed line is the two-body result for $n = 10^{11}\text{cm}^{-3}$.

two-body limit which is plotted as the dashed line in the inset of Fig. 7.2. The many-body T-matrix is found by inserting the two-body T-matrix for cesium obtained above into Eq. (7.3).

The experimentally relevant crossover is between a BCS-like state in the atomic continuum and a gas of condensed dimers occupying the upper branch of the avoided crossing. To describe theoretically this metastable configuration, we neglect the contribution to the thermodynamic potential that arises from the deeper-lying pole of the cesium two-body T-matrix corresponding to the lower branch of the avoided crossing. The resulting critical temperature for two densities is plotted in Fig. 7.8. As the magnetic field is increased across the Feshbach resonance, the character of the pairs changes gradually from stable and deeply-bound dimers to infinite-lifetime pairs weakly bound by many-body effects. The density of the pairs decreases gradually as B is increased, reaching zero as $B - B_0$ reaches ΔB, where the scattering length vanishes. For $B \geqslant B_0 + \Delta B$ there are no longer any pairs and both T_c and T_c^a reach their asymptotic value of T_a. In principle, experiments hint that ^{133}Cs molecules may be sufficiently

stable against decay caused by inelastic collisions [126, 127] but we find that the crossover will nevertheless be subject to a mechanical instability due to the attractive interaction between the molecules. Inelastic losses can also be induced in the vicinity of the Feshbach resonance by the presence of Efimov states. Indeed, by using methods employed in Ref. [136], we find that these three-body states lie in the narrow magnetic field range of $|B - B_0| \lesssim 0.01$ G.

The mechanical instability may be overcome on the BEC side by a positive background scattering length for the molecules, however it is not possible to properly treat this in a single-channel NSR setting and the inclusion of this and other effects of molecular interactions is an interesting problem for future exploration in the context of a two-channel model.

7.4 Outlook and conclusions

The effects described in this paper may be readily investigated in a variety of ways. Pairs of bosonic atoms can be experimentally detected using techniques that have been successfully employed to observe fermionic-atom pairs, for example, by the measurement of correlations in atom shot noise [97] or by radio-frequency spectroscopy [137, 138]. Furthermore, the experimental observation of a pronounced reduction in the critical temperature for condensation of paired and unpaired atoms is in itself compelling evidence that pairing is taking place. As is shown in Figs. 7.5 and 7.8, this striking effect can indeed be seen at relatively high temperatures where the gas remains mechanically stable.

Although the mechanical instability of the cesium gas may be overcome on the BEC side of the resonance due to a positive background scattering length for the molecules as mentioned in the previous section, it remains to be shown experimentally whether the gas is stable enough against inelastic losses. Indeed, measurements performed in Ref. [126] found inelastic losses due to dimer-dimer collisions of $1 \times 10^{-11}\mathrm{cm}^3/\mathrm{s}$ around $B = 46$ G which then increase for a fixed temperature as B_0 is approached. On the other hand, the loss rate was found to be strongly temperature-dependent and this may serve to significantly stabilize the gas near T_c.

Although not the focus of this paper, the condensation of unpaired atoms can also be used to experimentally shed light on some other interesting physics. For example, below T_c a transition between bound and unbound (half-)vortex pairs will take place as the T_c^a line is crossed from

the PC+AC phase to the PC phase [132, 133]. It would be very exciting if this could be directly observed as in the case of the Kosterlitz-Thouless transition in a two-dimensional Bose gas [100, 139]. However, it is not possible to make a definite prediction regarding the mechanical stability of the gas across this phase transition within the framework presented here [3]. Further insight may be obtained by using a two-channel approach to treat molecular interactions beyond mean-field theory. This has the added advantage that a background scattering length for the molecules as well as atom-molecule interactions can be readily included, and would be an interesting topic for further research.

Acknowledgements

The authors would like to thank Steven Knoop for fruitful discussions that inspired this project and for providing data on the Feshbach resonance. We also wish to thank Georg Bruun for his help in the early stages of the calculation. This work is supported by the Stichting voor Fundamenteel Onderzoek der Materie (FOM) and the Nederlandse Organisatie voor Wetenschaplijk Onderzoek (NWO), the Spanish MEC project TOQATA (FIS2008-00784) and the ESF/MEC project FERMIX (FIS2007-29996-E).

Notes

1. For $a \to 0^-$ we find numerically that $T_c - T_a \sim 2.03 \times (1/n^{1/3}a)^{-0.37}$. This contrasts with fermions where a logarithmic divergence of the correlation function in the particle-particle channel $\Xi(\mathbf{k}, i\omega_n)$ due to the presence of a Fermi sea leads to an exponential suppression of T_c.
2. The background scattering length is magnetic field-dependent predominantly due to a Feshbach resonance at -11.74G which is unrelated to the Feshbach resonance of interest here. It behaves as [140]

$$\frac{a_{\rm bg}(B)}{a_0} = (1722 + 1.52B)\left[1 - \frac{28.72}{B + 11.74}\right].$$

3. The stability at $T = 0$ has been explored in mean-field theory in [141] and [142].

A

Entropy Formulas

In this appendix we present the entropy formulas used in chapter 3.

For temperatures above T_c we use

$$\frac{S(T \geqslant T_c)}{Nk_\mathrm{B}} \simeq \alpha_1 \left[\left(\frac{T - T_c}{T} \right)^\kappa - 1 + \frac{\kappa T_c}{T} \right] + \ln(2) \ ,$$

with $\alpha_1 = 3J^2/32\kappa(\kappa-1)k_\mathrm{B}^2 T_c^2$ and $\kappa = 3\nu - 1 \simeq 0.89$ [76]. The first term embodies the correct critical behavior whereas the remaining terms are present to recover the correct high-temperature limit. Below T_c, however, we have

$$\begin{aligned} \frac{S(T \leqslant T_c)}{Nk_\mathrm{B}} = -\alpha_2 \Bigg[\left(\frac{T_c - T}{T_c} \right)^\kappa - 1 + \kappa \frac{T}{T_c} \\ - \frac{\kappa(\kappa-1)}{2} \frac{T^2}{T_c^2} \Bigg] + \beta_0 \frac{T^3}{T_c^3} + \beta_1 \frac{T^4}{T_c^4} \ , \end{aligned}$$

where

$$\begin{aligned} \alpha_2 =& \frac{6}{(\kappa-1)(\kappa-2)(\kappa-3)} \Bigg(\frac{4\pi^2 k_\mathrm{B}^3 T_c^3}{135\sqrt{3}J^3} \\ & - \alpha_1(\kappa-1) + \beta_1 - \ln(2) \Bigg) \ ; \\ \beta_0 =& \frac{\kappa}{(\kappa-3)} \left(\frac{4\pi^2 k_\mathrm{B}^3 T_c^3}{45\sqrt{3}\kappa J^3} + \alpha_1(\kappa-1) - \beta_1 + \ln(2) \right) \ ; \\ \beta_1 =& \ln 2 - J^2 \frac{6(A^+/A^- + 1) + \kappa(\kappa-5)}{64\kappa k_\mathrm{B}^2 T_c^2 A^+/A^-} - \frac{4\pi^2 k_\mathrm{B}^3 T_c^3}{135\sqrt{3}J^3} \ . \end{aligned}$$

The first and last terms in $S(T \leqslant T_c)$ embody the critical phenomena and allow for the continuous interpolation with $S(T \geqslant T_c)$ respectively, whereas the remaining terms are included to retrieve the correct low-temperature behavior.

B

The Mott insulator in a harmonic trap

A smooth harmonic confining potential has no effect on the Mott insulator other than to place a limit on the total number of atoms which, if exceeded, disrupts the Mott insulator state. This is illustrated in Fig. B.1. The Mott insulator in a harmonic trap for the one-dimensional case is shown in Fig. B.1(a), where the number of atoms is at the maximum. The energy levels for single and double occupancy of the lattice are shown as dashed lines. If more atoms are added, they should be placed in an empty sites in order to preserve the Mott insulator state. However, the energy cost of placing atoms at an outlying empty sites is higher than the energy cost of doubly-occupying lattice sites at the centre of the trap, as shown by the solid line, as shown in Fig. B.1(b).

For an isotropic optical lattice and smooth harmonic trap in d dimensions, the maximum number of atoms is

$$N_{\max} = \frac{1}{\Gamma(d/2+1)} \left(\frac{8\sqrt{\pi}U}{m\omega^2\lambda^2} \right)^{\frac{d}{2}} \tag{B.1}$$

where $\Gamma(x)$ is the Euler-gamma function, m is the mass of the atoms, ω is the frequency of the harmonic trap, and λ is the wavelength of the optical lattice lasers. For $d = 3$ this reduces to $N_{\max} = (4\pi/3)(8U/m\omega^2\lambda^2)^{3/2}$ which is the result presented in chapter 3.

To see how this result comes about, add a harmonic trapping potential

$$V(r_i) = \frac{1}{2} m\omega^2 \left(\frac{\lambda}{2} r_i \right)^2 \tag{B.2}$$

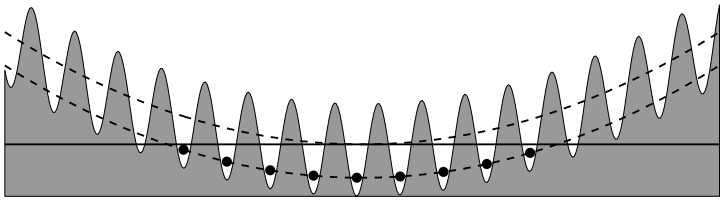

(a)

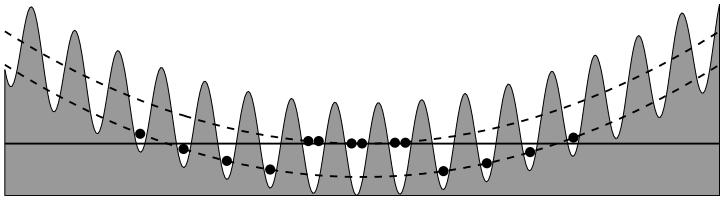

(b)

Figure B.1: Atoms in an optical lattice on top of a harmonic trap in one dimension. The dashed curves are the energy levels for singly and doubly occupied sites, and the solid line shows the energy of a doubly occupied site at the centre of the trap. **(a)** The number of particles is below the maximum. **(b)** The maximum number of particles is exceeded thereby disrupting the Mott insulator.

to the lattice, where $\lambda r_i/2$ is the distance of site i from the minimum of the trap. To prevent doubly occupied sites, we must have $V(r_i) < U$, as can be clearly deduced from Fig. B.1((b)). In the continuum limit, this becomes

$$r < \sqrt{\frac{U8}{m\omega^2\lambda^2}} \tag{B.3}$$

and writing $N_{\max} \simeq V_d$ with $V_d = \pi^{\frac{d}{2}} r^d/\Gamma(d/2+1)$ the volume of a d-dimensional sphere with radius r, we substitute for r to obtain the result in Eq. (B.1).

C

Kosterlitz-Thouless transition

Here we explain in detail how the critical temperature for the Kosterlitz-Thouless phase transition was obtained from the anisotropic $O(3)$ model studied by Klomfass *et al.* in [93]. The dimensionless free energy of that model is

$$\beta f_3 = -\beta_3 \sum_{\langle i,j \rangle} \mathbf{S}_i \cdot \mathbf{S}_j + \gamma_3 \sum_i (S_i^z)^2 \tag{C.1}$$

where $|\mathbf{S}_i| = 1$ [143]. The phase diagram obtained from Monte-Carlo simulations for the Kosterlitz-Thouless phase transition is shown in Fig. C.1. A fit function satisfying $\beta_3 = 1.06$ for $\gamma_3 \to \infty$ was obtained which approaches $\gamma_3 = 0$ exponentially as $\beta \to \infty$, as stated in Ref. [93], namely,

$$\gamma_3(\beta_3) = \frac{\beta_3}{\beta_3 - 1.06} \exp[-5.6(\beta_3 - 1.085)]. \tag{C.2}$$

To make make an analogy with this model, we relate the unit spin in Eq. (C.1) to the local staggered magnetization[1] as $\mathbf{n}_i = n\mathbf{S}_i$ where $n = \langle |\mathbf{n}| \rangle$ $= \langle |(-1)^j \hat{\mathbf{S}}_j| \rangle$ is the average value of the staggered magnetization. Then, the dimensionless free energy corresponding to the Heisenberg Hamiltonian is

$$\beta f_H = -\frac{J\beta}{2} \sum_{\langle i,j \rangle} \mathbf{n}_i \cdot \mathbf{n}_j. \tag{C.3}$$

The anisotropy caused by imbalance is embodied by the on-site mean-field free energy f_{MF} which we add to f_H to obtain the total free energy of the

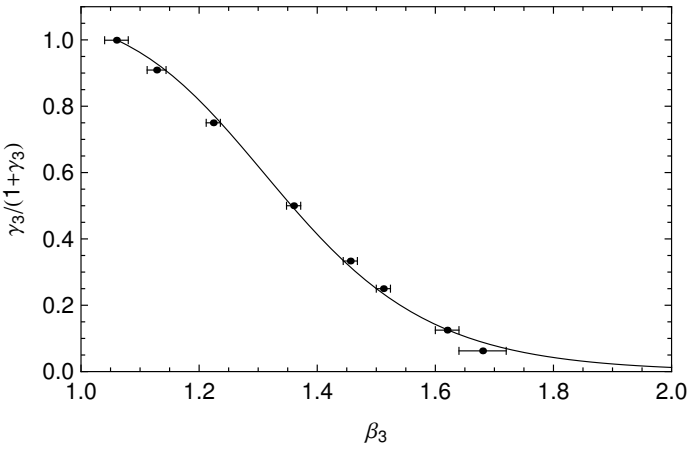

Figure C.1: Plot of Kosterlitz-Thouless critical line for the anisotropic $O(3)$ model, as found from Monte Carlo simulations (points with error bars). The curve is the fit given in Eq. (C.2).

imbalanced system

$$f = f_H + \sum_i f_{\mathrm{MF}}(\mathbf{m}, \mathbf{n}_i, \beta). \tag{C.4}$$

Now, we write the z-component of $\mathbf{n}_i$ as

$$n_i^z = \mathbf{n}_i \cdot \hat{\mathbf{z}} \equiv n \cos \alpha_i. \tag{C.5}$$

Expanding f to quadratic order in n_z, we obtain up to an additive constant,

$$\begin{aligned} \beta f \simeq & -\frac{J\beta}{2} \sum_{\langle i,j \rangle} \mathbf{n}_i \cdot \mathbf{n}_j + \beta\gamma(\mathbf{m}, \beta) n^2 \cos^2 \alpha_i \\ = & -\frac{J\beta n^2}{2} \sum_{\langle i,j \rangle} \mathbf{S}_i \cdot \mathbf{S}_j + \beta n^2 \gamma(\mathbf{m}, \beta) \sum_i (S_i^z)^2 \\ \equiv & -\beta_3 \sum_{\langle i,j \rangle} \mathbf{S}_i \cdot \mathbf{S}_j + \gamma_3 \sum_i (S_i^z)^2 \end{aligned} \tag{C.6}$$

where $\gamma(\mathbf{m}, \beta)$ is the prefactor with dimensions of energy found by fitting the anisotropy of the on-site mean-field free energy to a cosine squared, and is plotted in Fig. C.2 for various temperatures. Hence we identify

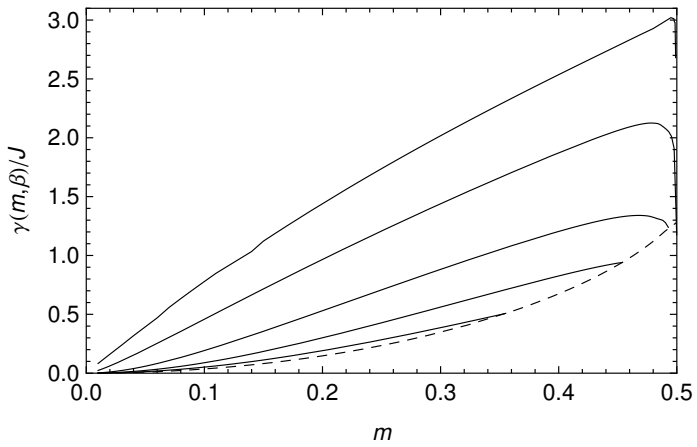

Figure C.2: Plot of $\gamma(\mathbf{m}, \beta)$. The solid curves are, from top to bottom, plotted for $1/J\beta = 0.02$, 0.2, 0.4, 0.6, and 0.8, respectively. The dashed curve is the value of $\gamma(\mathbf{m}, \beta)$ plotted along the critical temperature in two dimensions calculated from mean-field theory (i.e., the dashed line in Fig. 4.4). Beyond this critical line, $n = 0$ and a fit is no longer possible.

$$\beta_3 = \frac{J\beta n^2}{2}, \tag{C.7}$$

$$\gamma_3 = \beta n^2 \gamma(\mathbf{m}, \beta) = 2\beta_3 \frac{\gamma(\mathbf{m}, \beta)}{J}. \tag{C.8}$$

From Fig. C.1, $\beta_3 > 1.06$, hence Eq. (C.7) yields an upper bound on the critical temperature of $k_B T_c/J < .118$. In general, by solving

$$\frac{2}{J}\gamma(\mathbf{m}, \beta) = \frac{1}{\beta_3 - 1.06} \exp[-5.6(\beta_3 - 1.085)] \tag{C.9}$$

for β we obtain an expression for the critical temperature $T = 1/k_B\beta$. The solution at various $\mathbf{m}$ is the critical temperature in two dimensions shown in Fig. 4.4. We note that in the limit of small m, the expression for the critical temperature is well approximated by $k_B T/J \simeq 0.1167 m^{1/12}$.

Notes

1. For consistency with the notation used in Ref. [93], we treat $\mathbf{S}_i$ as the *staggered* magnetization. Note that Eq. (C.1) then leads to an antiferromagnetic ground state for $\beta_3 > 0$.

D

The screened interaction

Here we estimate the impact of screening effects mentioned in chapters 5 and 7 on the critical temperature. In the random phase approximation (RPA), we can estimate screening effects by replacing the interaction potential with a screened interaction containing a sum of bubble diagrams

If we close the external lines, then the first term of this series is identical to that of the ladder sum evaluated in Eq. (5.14). The second term in the series is

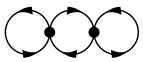

$$= -\frac{V_0}{\hbar}\frac{1}{\hbar\beta V}\sum_{\substack{\mathbf{k},\mathbf{k}'\\ nn'}} G(\mathbf{k},n)G(\mathbf{k}',n')V_0\Pi.$$

Here,

$$\begin{aligned}\Pi &= -\frac{1}{\hbar^2\beta V}\sum_{\mathbf{q},m} G(\mathbf{q},m)^2 \\ &= -\frac{1}{\hbar^2\beta V}\sum_{\mathbf{q},m}\left(\frac{1}{i\omega_m - (\varepsilon_{\mathbf{q}}-\mu)/\hbar}\right)^2 \\ &= -\beta\frac{4\pi}{(2\pi)^3}\left(\frac{2m}{\hbar^2}\right)^{3/2}\frac{1}{2}\int_0^\infty d\varepsilon \frac{\sqrt{\varepsilon}}{4\sinh^2\left[\frac{\beta}{2}(\varepsilon-\mu)\right]},\end{aligned}$$

where we took the thermodynamic limit in the last step. Taking into account the multiplicity of the diagrams, we can now evaluate the entire bubble series as it appears in the perturbative expansion of the action in Eq. (5.10), namely,

$$
\begin{aligned}
&2\frac{1}{2}\ \text{ 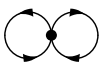 }\ + 2^4\frac{1}{2!}\frac{1}{2^2}\ \text{ 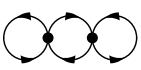 }\ + 2^8\frac{1}{3!}\frac{1}{2^3}\ \text{ 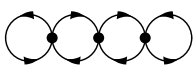 }\ + \cdots \\
&= -\frac{V_0}{\hbar}\frac{1}{\hbar\beta V}\sum_{\substack{\mathbf{k},\mathbf{k}'\\ nn'}} G(\mathbf{k},n)G(\mathbf{k}',n')\left(1+\frac{4}{2}V_0\Pi+\frac{4^2}{3}(V_0\Pi)^2+\ldots\right) \\
&= \frac{-1}{\hbar^2\beta V}\sum_{\substack{\mathbf{k},\mathbf{k}'\\ nn'}} G(\mathbf{k},n)G(\mathbf{k}',n')\frac{1}{4\Pi}\ln\left(\frac{1}{1-4V_0\Pi}\right). \qquad \text{(D.1)}
\end{aligned}
$$

If we do not close the external lines (the symmetrisation factor $1/p$ is then absent), we obtain

$$
\text{  } = V_0\sum_{p=0}^{\infty}(4V_0\Pi)^p = \frac{V_0}{1-4V_0\Pi}.
$$

We estimate the effects of screening on NSR theory by replacing the interaction with the screened interaction at every order of the ladder sum. The self-energy in the T-matrix approximation then becomes

$$
\begin{aligned}
&\text{ 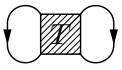 } = \text{ 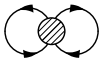 } + \frac{1}{2}\ \text{  }\ + \cdots \\
&= \sum_{M,\mathbf{K}}\sum_{p=1}^{\infty}\frac{1}{p}\left[\frac{V_0}{1-4V_0\Pi}\Xi'(\mathbf{K},i\omega_M)\right]^p \\
&= \sum_{M,\mathbf{K}}\ln\left[\frac{1}{[T^{2\mathrm{B}}(i\omega_M)]^{-1}-4\Pi-\Xi'(\mathbf{K},i\omega_M)}\right] \\
&\qquad\qquad - \sum_{M,\mathbf{K}}\ln\left[\frac{V_0}{1-4V_0\Pi}\right] \qquad \text{(D.2)}
\end{aligned}
$$

where we used the renormalization procedure of §5.3.2. Note that we made a zero-momentum approximation by neglecting momentum transfer between internal loops. This is valid for the low energies of interest here. Comparing this result with Eq. (5.27), we see that screening the interaction

amounts to the substitution $\Xi' \to \Xi' + 4\Pi$. The screened thermodynamic potential is then

$$\frac{\Omega}{V} = -\frac{1}{\beta V}\ln Z_0 - \frac{1}{\beta V}\sum_{M,\mathbf{K}} \ln\left[\frac{1}{[T^{2\mathrm{B}}(i\omega_M)]^{-1} - 4\Pi - \Xi'(\mathbf{K}, i\omega_M)}\right] - \frac{1}{\beta V}\sum_{M,\mathbf{K}} \ln\left[\frac{V_0}{1 - 4V_0\Pi}\right]. \quad \text{(D.3)}$$

We can absorb Π into $T^{2\mathrm{B}}$ which amounts to performing a temperature and μ-dependent shift of the scattering length. The critical temperature curve obtained without screening can be rescaled in this way to produce an approximate critical temperature curve that includes screening. Note that this is not self-consistent as the extra μ-dependence is not properly taken into account in the number equation. However, a fully self-consistent calculation is beyond the scope of the present work.

Bibliography

[1] S. N. Bose, *Plancks Gesetz und Lichtquantenhypothese*, Z. Phys. **26,** 178 (1924).

[2] A. Einstein, *Quantentheorie des einatomigen idealen Gases*, Sitz. Ber. Preuss. Akad. Wiss. (Berlin) **22,** 261 (1924).

[3] P. Kapitza, *Viscosity of liquid helium below the λ-point*, Nature **141,** 74 (1938).

[4] J. F. Allen and A. D. Misener, *Flow of liquid helium II*, Nature **141,** 75 (1938).

[5] E. L. Raab, M. Prentiss, Alex Cable, Steven Chu, and D. E. Pritchard, *Trapping of Neutral Sodium Atoms with Radiation Pressure*, Phys. Rev. Lett. **59,** 2631 (1987).

[6] Naoto Masuhara, John M. Doyle, Jon C. Sandberg, Daniel Kleppner, Thomas J. Greytak, Harald F. Hess, and Greg P. Kochanski, *Evaporative Cooling of Spin-Polarized Atomic Hydrogen*, Phys. Rev. Lett. **61,** 935 (1988).

[7] C. Monroe, W. Swann, H. Robinson, and C. Wieman, *Very cold trapped atoms in a vapor cell*, Phys. Rev. Lett. **65,** 1571 (1990).

[8] M. H. Anderson, J. R. Ensher, M. R. Matthews, C. E. Wieman, and E. A. Cornell, *Observation of Bose-Einstein condensation in a dilute atomic vapor*, Science **269,** 198 (1995).

[9] C. C. Bradley, C. A. Sackett, J. J. Tollett, and R. G. Hulet, *Evidence of Bose-Einstein condensation in an atomic gas with attractive interactions*, Phys. Rev. Lett. **75,** 1687 (1995).

[10] K. B. Davis, M. O. Mewes, M. R. Andrews, N. J. van Druten, D. S. Durfee, D. M. Kurn, and W. Ketterle, *Bose-Einstein condensation in a gas of sodium atoms*, Phys. Rev. Lett. **75,** 3969 (1995).

[11] H. Kamerlingh-Onnes, *The resistance of platinum at helium temperatures*, Comm. Phys. Lab. Univ. Leiden **119,** Part B. (1911).

[12] H. Kamerlingh-Onnes, *The resistance of gold and pure mercury at helium temperatures*, Comm. Phys. Lab. Univ. Leiden **120b** (1911).

[13] H. Kamerlingh-Onnes, *The disappearance of the resistance of mercury*, Comm. Phys. Lab. Univ. Leiden **122b** (1911).

[14] H. Kamerlingh-Onnes, *On the sudden change in the rate at which the resistance of mercury disappears*, Comm. Phys. Lab. Univ. Leiden **124c** (1911).

[15] J. Bardeen, L. N. Cooper, and J. R. Schrieffer, *Theory of superconductivity*, Phys. Rev. **108,** 1175 (1957).

[16] Henning Heiselberg, *Fermi systems with long scattering lengths*, Phys. Rev. A **63,** 043606 (2001).

[17] George A. Baker, *Neutron matter model*, Phys. Rev. C **60,** 054311 (1999).

[18] J. Carlson, S.-Y. Chang, V. R. Pandharipande, and K. E. Schmidt, *Superfluid Fermi gases with large scattering length*, Phys. Rev. Lett. **91,** 050401 (2003).

[19] Yu. A. Litvinov *et al.*, *Isospin dependence in the odd-even staggering of nuclear binding energies*, Phys. Rev. Lett. **95,** 042501 (2005).

[20] Roberto Casalbuoni and Giuseppe Nardulli, *Inhomogeneous superconductivity in condensed matter and QCD*, Rev. Mod. Phys. **76,** 263–320 (2004).

[21] A. Sedrakian and U. Lombardo, *Thermodynamics of a n-p condensate in asymmetric nuclear matter*, Phys. Rev. Lett. **84,** 602 (2000).

[22] Mark Alford, Jeffrey A. Bowers, and Krishna Rajagopal, *Crystalline color superconductivity*, Phys. Rev. D **63,** 074016 (2001).

[23] Paulo F. Bedaque, *Color superconductivity in asymmetric matter*, Nucl. Phys. A **697,** 569 (2002).

[24] P. F. Kolb and U. Heinz, *Quark Gluon Plasma 3* (World Scientific, Singapore, 2003), p. 634.

[25] H. T. C. Stoof, M. Houbiers, C. A. Sackett, and R. G. Hulet, *Superfluidity of Spin-Polarized ^{6}Li*, Phys. Rev. Lett. **76,** 10 (1996).

[26] C. J. Myatt, E. A. Burt, R. W. Ghrist, E. A. Cornell, and C. E. Wieman, *Production of two overlapping Bose-Einstein condensates by sympathetic cooling*, Phys. Rev. Lett. **78,** 586 (1997).

[27] Andrew G. Truscott, Kevin E. Strecker, William I. McAlexander, Guthrie B. Partridge, and Randall G. Hulet, *Observation of Fermi pressure in a gas of trapped atoms*, Science **291,** 2570 (2001).

[28] B. DeMarco and D. S. Jin, *Onset of Fermi degeneracy in a trapped atomic gas*, Science **285,** 1703 (1999).

[29] B. DeMarco, S. B. Papp, and D. S. Jin, *Pauli blocking of collisions in a quantum degenerate atomic Fermi gas*, Phys. Rev. Lett. **86,** 5409 (2001).

[30] M. Greiner, C. A. Regal, and D. S. Jin, *Emergence of a molecular Bose-Einstein condensate from a Fermi gas*, Nature **426,** 537 (2003).

[31] S. Jochim, M. Bartenstein, A. Altmeyer, G. Hendl, S. Riedl, C. Chin, J. Hecker Denschlag, and R. Grimm, *Bose-Einstein condensation of molecules*, Science **302,** 2101 (2003).

[32] M. W. Zwierlein, C. A. Stan, C. H. Schunck, S. M. F. Raupach, S. Gupta, Z. Hadzibabic, and W. Ketterle, *Observation of Bose-Einstein condensation of molecules*, Phys. Rev. Lett. **91,** 250401 (2003).

[33] William C. Stwalley, *Stability of spin-aligned hydrogen at low temperatures and high magnetic fields: New field-dependent scattering resonances and predissociations*, Phys. Rev. Lett. **37,** 1628 (1976).

[34] E. Tiesinga, B. J. Verhaar, and H. T. C. Stoof, *Threshold and resonance phenomena in ultracold ground-state collisions*, Phys. Rev. A **47,** 4114 (1993).

[35] M. Houbiers, H. T. C. Stoof, W. I. McAlexander, and R. G. Hulet, *Elastic and inelastic collisions of ^{6}Li atoms in magnetic and optical traps*, Phys. Rev. A **57,** R1497 (1998).

[36] C. A. Regal, M. Greiner, and D. S. Jin, *Observation of resonance condensation of fermionic atom pairs*, Phys. Rev. Lett. **92,** 040403 (2004).

[37] M. W. Zwierlein, C. A. Stan, C. H. Schunck, S. M. F. Raupach, A. J. Kerman, and W. Ketterle, *Condensation of pairs of fermionic atoms near a Feshbach resonance*, Phys. Rev. Lett. **92,** 120403 (2004).

[38] Joseph Kinast, S. L. Hemmer, M. E. Gehm, A. Turlapov, and J. E. Thomas, *Evidence for superfluidity in a resonantly interacting Fermi gas*, Phys. Rev. Lett. **92,** 150402 (2004).

[39] M. Bartenstein, A. Altmeyer, S. Riedl, S. Jochim, C. Chin, J. Hecker Denschlag, and R. Grimm, *Collective excitations of a degenerate gas at the BEC-BCS crossover*, Phys. Rev. Lett. **92,** 203201 (2004).

[40] T. Bourdel, L. Khaykovich, J. Cubizolles, J. Zhang, F. Chevy, M. Teichmann, L. Tarruell, S. J. J. M. F. Kokkelmans, and C. Salomon, *Experimental study of the BEC-BCS crossover region in lithium 6*, Phys. Rev. Lett. **93,** 050401 (2004).

[41] G. B. Partridge, K. E. Strecker, R. I. Kamar, M. W. Jack, and R. G. Hulet, *Molecular probe of pairing in the BEC-BCS crossover*, Phys. Rev. Lett. **95,** 020404 (2005).

[42] P. S. Jessen and I. H. Deutsch, *Optical lattices*, Adv. At. Mol. Opt. Phys. **37,** 95 (1996).

[43] J. G. Bednorz and K. A. Müller, *Possible high-Tc superconductivity in the Ba-La-Cu-O system*, Z. Phys. B **64,** 189 (1986).

[44] W. Hofstetter, J. I. Cirac, P. Zoller, E. Demler, and M. D. Lukin, *High-temperature superfluidity of fermionic atoms in optical lattices*, Phys. Rev. Lett. **89,** 220407 (2002).

[45] Qijin Chen, Jelena Stajic, Shina Tan, and K. Levin, *BCS-BEC crossover: From high temperature superconductors to ultracold superfluids*, Phys. Rep. **412,** 1 (2005).

[46] D. Jaksch, C. Bruder, J. I. Cirac, C. W. Gardiner, and P. Zoller, *Cold bosonic atoms in optical lattices*, Phys. Rev. Lett. **81,** 3108 (1998).

[47] M. P. A. Fisher, P. B. Weichman, G. Grinstein, and D. S. Fisher, *Boson localization and the superfluid-insulator transition*, Phys. Rev. B **40,** 546 (1989).

[48] M. Greiner, O. Mandel, T. Esslinger, T. W. Hänsch, and I. Bloch, *Quantum phase transition from a superfluid to a Mott insulator in a gas of ultracold atoms*, Nature **415,** 39 (2002).

[49] Martin W. Zwierlein, André Schirotzek, Christian H. Schunck, and Wolfgang Ketterle, *Fermionic superfluidity with imbalanced spin populations*, Science **311,** 492 (2006).

[50] Guthrie B. Partridge, Wenhui Li, Ramsey I. Kamar, Yean-an Liao, and Randall G. Hulet, *Pairing and phase separation in a polarized Fermi gas*, Science **311,** 503 (2006).

[51] D. D. Osheroff, R. C. Richardson, and D. M. Lee, *Evidence for a new phase of solid He^3*, Phys. Rev. Lett. **28,** 885 (1972).

[52] D. D. Osheroff, W. J. Gully, R. C. Richardson, and D. M. Lee, *New magnetic phenomena in liquid He^3 below 3 mK*, Phys. Rev. Lett. **29,** 920 (1972).

[53] A. Schilling, M. Cantoni, J. D. Guo, and H. R. Ott, *Superconductivity above 130 K in the HgBaCaCuO system*, Nature **363,** 56 (1993).

[54] P. Dai, B. C. Chakoumakos, G. F. Sun, K. W. Wong, Y. Xin, and D. F. Lu, *Synthesis and neutron powder diffraction study of the superconductor* $HgBa_2Ca_2Cu_3O_{8+\delta}$ *by Tl substitution*, Physica C **243,** 201 (1995).

[55] A. F. Hebard, M. J. Rosseinsky, R. C. Haddon, D. W. Murphy, S. H. Glarum, T. T. M. Palstra, A. P. Ramirez, and A. R. Kortan, *Superconductivity at 18 K in potassium-doped* C_{60}, Nature **350,** 600 (1991).

[56] Yoichi Kamihara, Takumi Watanabe, Masahiro Hirano, and Hideo Hosono, *Iron-based layered superconductor* $LaO_{1-x}F_xFeAs$ *(x=0.05–0.12) with* $T_c = 26$ *K*, J. Am. Chem. Soc. **130,** 3296 (2008).

[57] Hiroki Takahashi, Kazumi Igawa, Kazunobu Arii, Yoichi Kamihara, Masahiro Hirano, and Hideo Hosono, *Superconductivity at 43 K in an iron-based layered compound* $LaO_{1-x}F_xFeAs$, Nature **453,** 376 (2008).

[58] J. Hubbard, *Electron correlations in narrow energy bands*, Proc. Roy. Soc. A **276,** 238 (1963).

[59] P. W. Anderson, *The resonating valence bond state in* La_2Cu0_4 *and superconductivity*, Science **235,** 1196 (1987).

[60] F. C. Zhang and T. M. Rice, *Effective Hamiltonian for the superconducting Cu oxides*, Phys. Rev. B **37,** 3759 (1988).

[61] V. S. Letokhov, *Narrowing of the doppler width in a standing wave*, JETP Letters **7,** 272 (1968).

[62] C. Salomon, J. Dalibard, A. Aspect, H. Metcalf, and C. Cohen-Tannoudji, *Channeling atoms in a laser standing wave*, Phys. Rev. Lett. **59,** 1659 (1987).

[63] R. Jordens, N. Strohmaier, K. Günter, H. Moritz, and T. Esslinger, *A Mott insulator of fermionic atoms in an optical lattice*, Nature **455,** 204 (2008).

[64] U. Schneider, L. Hackermuller, S. Will, Th. Best, I. Bloch, T. A. Costi, R. W. Helmes, D. Rasch, and A. Rosch, *Metallic and insulating phases of repulsively interacting fermions in a 3D optical lattice*, Science **322,** 1520 (2008).

[65] Immanuel Bloch, Jean Dalibard, and Wilhelm Zwerger, *Many-body physics with ultracold gases*, Rev. Mod. Phys. **80** (2008).

[66] D. B. M. Dickerscheid, U. Al Khawaja, D. van Oosten, and H. T. C. Stoof, *Feshbach resonances in an optical lattice*, Phys. Rev. A **71,** 043604 (2005).

[67] Wilhelm Zwerger, *Mott-Hubbard transition of cold atoms in optical lattices*, J. of Opt. B **5,** S9 (2003).

[68] Michael Köhl, Henning Moritz, Thilo Stöferle, Kenneth Günter, and Tilman Esslinger, *Fermionic atoms in a three dimensional optical lattice: Observing Fermi surfaces, dynamics, and interactions*, Phys. Rev. Lett. **94,** 080403 (2005).

[69] H. T. C. Stoof, K. B. Gubbels, and D. B. M. Dickerschied, *Ultracold Quantum Fields* (Springer, Dordrecht, 2009).

[70] M. Köhl, H. Moritz, T. Stöferle, K. Günter, and T. Esslinger, *Fermionic atoms in a three dimensional optical lattice: Observing Fermi surfaces, dynamics, and interactions*, Phys. Rev. Lett. **94,** 080403 (2005).

[71] Patrick A. Lee, Naoto Nagaosa, and Xiao-Gang Wen, *Doping a Mott insulator: Physics of high-temperature superconductivity*, Rev. Mod. Phys. **78,** 17 (2006).

[72] F. Werner, O. Parcollet, A. Georges, and S. R. Hassan, *Interaction-induced adiabatic cooling and antiferromagnetism of cold fermions in optical lattices*, Phys. Rev. Lett. **95,** 056401 (2005).

[73] P. B. Blakie, A. Bezett, and P. Buonsante, *Degenerate Fermi gas in a combined harmonic-lattice potential*, Phys. Rev. A **75,** 063609 (2007).

[74] Ehud Altman, Eugene Demler, and Mikhail D. Lukin, *Probing many-body states of ultracold atoms via noise correlations*, Phys. Rev. A **70,** 013603 (2004).

[75] T. Rom, Th. Best, D. van Oosten, U. Schneider, S. Foelling, B. Paredes, and I. Bloch, *Free fermion antibunching in a degenerate atomic Fermi gas released from an optical lattice*, Nature **444,** 733 (2006).

[76] J. Zinn-Justin, *Quantum Field Theory and Critical Phenomena*, fourth ed. (Oxford University Press, 2002).

[77] A. Auerbach, *Interacting Electrons and Quantum Magnetism* (Springer-Verlag, New York, 1994).

[78] L. D. Carr, G. V. Shlyapnikov, and Y. Castin, *Achieving a BCS transition in an atomic Fermi gas*, Phys. Rev. Lett. **92,** 150404 (2004).

[79] R. Staudt, M. Dzierzawa, and A. Muramatsu, *Phase diagram of the three-dimensional Hubbard model at half filling*, Eur. Phys. J. B **17,** 411–415 (2000).

[80] K. Borejsza and N. Dupuis, *Antiferromagnetism and single-particle properties in the two-dimensional half-filled Hubbard model: A nonlinear sigma model approach*, Phys. Rev. B **69,** 085119 (2004).

[81] D. Bailin and A. Love, *Superfluidity and superconductivity in relativistic fermion systems*, Phys. Rep. **107,** 325 (1984).

[82] Mark Alford, Krishna Rajagopal, and Frank Wilczek, *QCD at finite baryon density: nucleon droplets and color superconductivity*, Phys. Lett. B **422,** 247 (1998).

[83] Arnaud Koetsier, D. B. M Dickerscheid, and H. T. C. Stoof, *BEC-BCS crossover in an optical lattice*, Phys. Rev. A **74,** 033621 (2006).

[84] T. Gottwald and P. G. J. van Dongen, *Antiferromagnetic order of repulsively interacting fermions on optical lattices*, arXiv:0903.5265 .

[85] Arnaud Koetsier, R. A. Duine, Immanuel Bloch, and H. T. C. Stoof, *Achieving the Néel state in an optical lattice*, Phys. Rev. A **77,** 023623 (2008).

[86] M. Snoek, I. Titvinidze, C. Toke, K. Byczuk, and W. Hofstetter, *Antiferromagnetic order of strongly interacting fermions in a trap: Real-space dynamical mean-field analysis*, New J. Phys. **10,** 093008 (2008).

[87] S. Das Sarma, Subir Sachdev, and Lian Zheng, *Canted antiferromagnetic and spin-singlet quantum Hall states in double-layer systems*, Phys. Rev. B **58,** 4672 (1998).

[88] David J. Gross, *Meron configurations in the two-dimensional O(3) σ-model*, Nucl. Phys. B **132,** 439 (1978).

[89] Ian Affleck, *Mass generation by merons in quantum spin chains and the O(3) σ-model*, Phys. Rev. Lett. **56,** 408 (1986).

[90] K. Moon, H. Mori, Kun Yang, S. M. Girvin, A. H. MacDonald, L. Zheng, D. Yoshioka, and Shou-Cheng Zhang, *Spontaneous interlayer coherence in double-layer quantum Hall systems: Charged vortices and Kosterlitz-Thouless phase transitions*, Phys. Rev. B **51,** 5138 (1995).

[91] J. M. Kosterlitz and D. J. Thouless, *Ordering, metastability and phase transitions in two-dimensional systems*, J. Phys. C **6,** 1181 (1973).

[92] J. M. Kosterlitz, *The critical properties of the two-dimensional XY model*, J. Phys. C **7,** 1046 (1974).

[93] Markus Klomfass, Urs M. Heller, and Henrik Flyvbjerg, *Interpolating between Ising, XY-, and non-linear σ-models*, Nucl. Phys. B **360,** 264 (1991).

[94] N. D. Mermin and H. Wagner, *Absence of ferromagnetism or antiferromagnetism in one- or two-dimensional isotropic Heisenberg models*, Phys. Rev. Lett. **17,** 1133 (1966).

[95] E. Fradkin, *Field Theories of Condensed Matter Systems* (Addison-Wesley, Redwood City, 1991).

[96] S. Föllingand F. Gerbier, A. Widera, O. Mandel, T. Gericke, and I. Bloch, *Spatial quantum noise interferometry in expanding ultracold atom clouds*, Nature **434,** 481 (2005).

[97] M. Greiner, C. A. Regal, J. T. Stewart, and D. S. Jin, *Probing pair-correlated fermionic atoms through correlations in atom shot noise*, Phys. Rev. Lett. **94,** 110401 (2005).

[98] N. Fabbri, D. Clément, L. Fallani, C. Fort, M. Modugno, K. M. R. van der Stam, and M. Inguscio, *Excitations of Bose-Einstein condensates in a one-dimensional periodic potential*, Phys. Rev. A **79,** 043623 (2009).

[99] D. Clément, N. Fabbri, L. Fallani, C. Fort, and M. Inguscio, *Exploring correlated 1D Bose gases from the superfluid to the Mott-insulator state by inelastic light scattering*, Phys. Rev. Lett. **102,** 155301 (2009).

[100] Z. Hadzibabic, P. Krüger, M. Cheneau, B. Battelier, and J. B. Dalibard, *Berezinskii-Kosterlitz-Thouless crossover in a trapped atomic gas*, Nature **441,** 1118 (2006).

[101] T. Gericke, P. Würtz, D. Reitz, T. Langen, and H. Ott, *High-resolution scanning electron microscopy of an ultracold quantum gas*, Nature Phys. **4,** 949 (2008).

[102] P. Würtz, T. Langen, T. Gericke, A. Koglbauer, and H. Ott, *Experimental demonstration of single-site addressability in a two-dimensional optical lattice*, arXiv:0903.4837 .

[103] Sankalpa Ghosh and R. Rajaraman, *Meron pseudospin solutions in quantum Hall systems*, Int. J. Mod. Phys. B **12,** 37 (1998).

[104] Herman Feshbach, *Unified theory of nuclear reactions*, Ann. Phys. (NY) **5,** 357 (1958).

[105] Herman Feshbach, *A unified theory of nuclear reactions. II*, Ann. Phys. (NY) **19,** 287 (1962).

[106] P. Nozières and S. Schmitt-Rink, *Bose condensation in an attractive fermion gas: From weak to strong coupling superconductivity*, J. Low Temp. Phys. **59,** 195 (1985).

[107] D. S. Petrov, C. Salomon, and G. V. Shlyapnikov, *Weakly bound dimers of Fermionic atoms*, Phys. Rev. Lett. **93,** 090404 (2004).

[108] Joseph Kinast, Andrey Turlapov, John E. Thomas, Qijin Chen, Jelena Stajic, and Kathryn Levin, *Heat capacity of a strongly interacting Fermi gas*, Science **307,** 1296 (2005).

[109] Guthrie B. Partridge, Wenhui Li, Ramsey I. Kamar, Yean an Liao, and Randall G. Hulet, *Pairing and phase separation in a polarized Fermi gas*, Science **311,** 503 (2006).

[110] Thilo Stöferle, Henning Moritz, Kenneth Günter, Michael Köhl, and Tilman Esslinger, *Molecules of fermionic atoms in an optical lattice*, Phys. Rev. Lett. **96,** 030401 (2006).

[111] R. Micnas, J. Ranninger, and S. Robaszkiewicz, *Superconductivity in narrow–band systems with local nonretarted attractive interactions*, Rev. Mod. Phys. **62,** 113 (1990).

[112] C. N. Yang and Shou-Cheng Zhang, *SO(4) symmetry in a Hubbard model*, Mod. Phys. Lett. B **4,** 759 (1990).

[113] Shou-Cheng Zhang, *A unified theory based on SO(5) symmetry of superconductivity and antiferromagnetism*, Science **275,** 1089 (1997).

[114] Eugene Demler and Shou-Cheng Zhang, *Quantitative test of a microscopic mechanism of high-temperature superconductivity*, Nature **396,** 733 (1998).

[115] R. A. Duine and H. T. C. Stoof, *Atom–molecule coherence in Bose gases*, Phys. Rep. **396,** 115 (2004).

[116] Henning Moritz, Thilo Stöferle, Kenneth Günter, Michael Köhl, and Tilman Esslinger, *Confinement induced molecules in a 1D Fermi gas*, Phys. Rev. Lett. **94,** 210401 (2005).

[117] D. B. M Dickerscheid and H. T. C. Stoof, *Feshbach molecules in a one–dimensional Fermi gas*, Phys. Rev. A **72,** 053625 (2005).

[118] G. M. Falco and H. T. C. Stoof, *Crossover temperature of Bose-Einstein condensation in an atomic Fermi gas*, Phys. Rev. Lett. **92,** 130401 (2004).

[119] M. W. J. Romans and H. T. C. Stoof, *Dressed Feshbach molecules in the BEC–BCS crossover*, Phys. Rev. Lett. **95,** 260407 (2005).

[120] Thomas Busch, Berthold-Georg Englert, Kazimierz Rzążewski, and Martin Wilkens, *Two cold atoms in a harmonic trap*, Found. Phys. **28,** 549 (1998).

[121] D. M. Eagles, *Possible pairing without superconductivity at low carrier concentrations in bulk and thin-film superconducting semiconductors*, Phys. Rev. **186,** 456 (1969).

[122] A. J. Leggett, *Diatomic molecules and Cooper pairs*, in *Modern Trends in the Theory of Condensed Matter. Proceedings of the XVIth Karpacz Winter School of Theoretical Physics, Karpacz, Poland* (Springer-Verlag, Berlin, 1980), pp. 13–27.

[123] *Ultracold Fermi Gases, Proceedings of the International School of Physics "Enrico Fermi", Course CLXIV, Varenna, 20 - 30 June 2006*, M. Inguscio, W. Ketterle, and C. Salomon, eds., (IOS Press, Amsterdam, 2008).

[124] K. Xu, T. Mukaiyama, J. R. Abo-Shaeer, J. K. Chin, D. E. Miller, and W. Ketterle, *Formation of quantum-degenerate sodium molecules*, Phys. Rev. Lett. **91,** 210402 (2003).

[125] H. T. C. Stoof, *Atomic Bose gas with a negative scattering length*, Phys. Rev. A **49,** 3824 (1994).

[126] F. Ferlaino, S. Knoop, M. Mark, M. Berninger, H. Schöbel, H.-C. Nägerl, and R. Grimm, *Collisions between tunable halo dimers: Exploring an elementary four-body process with identical bosons*, Phys. Rev. Lett. **101,** 023201 (2008).

[127] S. Knoop, F. Ferlaino, M. Mark, M. Berninger, H. Schöbel, H. C. Nägerl, and R. Grimm, *Observation of an Efimov-like trimer resonance in ultracold atom-dimer scattering*, Nature Phys. **5,** 227 (2009).

[128] David J. Thouless, *Perturbation theory in statistical mechanics and the theory of superconductivity*, Ann. Phys. (NY) **10,** 553 (1960).

[129] H. T. C. Stoof, M. Bijlsma, and M. Houbiers, *Theory of interacting quantum gases*, J. Res. Natl. Inst. Stand. Technol. **101,** 443 (1996).

[130] G. M. Falco, R. A. Duine, and H. T. C. Stoof, *Molecular Kondo Resonance in Atomic Fermi Gases*, Phys. Rev. Lett. **92,** 140402 (2004).

[131] W. A. B. Evans and R. I. M. A. Rashid, *A conserving approximation evaluation of superfluid density within the pair theory of superfluids*, J. Low Temp. Phys. **11,** 93 (1973).

[132] Leo Radzihovsky, Jae Park, and Peter B. Weichman, *Superfluid transitions in bosonic atom-molecule mixtures near a Feshbach resonance*, Phys. Rev. Lett. **92,** 160402 (2004).

[133] M. W. J. Romans, R. A. Duine, Subir Sachdev, and H. T. C. Stoof, *Quantum phase transition in an atomic Bose gas with a Feshbach resonance*, Phys. Rev. Lett. **93,** 020405 (2004).

[134] A. D. Lange, K. Pilch, A. Prantner, F. Ferlaino, B. Engeser, H.-C. Nägerl, R. Grimm, and C. Chin, *Determination of atomic scattering lengths from measurements of molecular binding energies near Feshbach resonances*, Phys. Rev. A **79,** 013622 (2009).

[135] G. M. Bruun, A. D. Jackson, and E. E. Kolomeitsev, *Multichannel scattering and Feshbach resonances: Effective theory, phenomenology, and many-body effects*, Phys. Rev. A **71,** 052713 (2005).

[136] P. Massignan and H. T. C. Stoof, *Efimov states near a Feshbach resonance*, Phys. Rev. A **78,** 030701(R) (2008).

[137] C. Chin, M. Bartenstein, A. Altmeyer, S. Riedl, S. Jochim, J. Hecker Denschlag, and R. Grimm, *Observation of the pairing gap in a strongly interacting Fermi gas*, Science **305,** 1128 (2004).

[138] C. H. Schunck, Y. Shin, A. Schirotzek, M. W. Zwierlein, and W. Ketterle, *Pairing without superfluidity: The ground state of an imbalanced Fermi mixture*, Science **316,** 867 (2007).

[139] V. Schweikhard, S. Tung, and E. A. Cornell, *Vortex proliferation in the Berezinskii-Kosterlitz-Thouless regime on a two-dimensional lattice of Bose-Einstein condensates*, Phys. Rev. Lett. **99,** 030401 (2007).

[140] T. Kraemer *et al.*, *Evidence for Efimov quantum states in an ultracold gas of caesium atoms*, Nature **440,** 315 (2006).

[141] E. Mueller and S. Basu, *Stability of Bosonic atomic and molecular condensates near a Feshbach resonance*, arXiv:cond-mat/0507460 .

[142] Lan Yin, *Phase diagram of a Bose gas near a wide Feshbach resonance*, Phys. Rev. A **77,** 043630 (2008).

[143] M. C. Ogilvie and G. S. Guralnik, *Instantons and vortices in two dimensions*, Nucl. Phys. B **190,** 325 (1981).

Summary

This thesis explores certain extraordinary phenomena that occur when a gas of neutral atoms is cooled to the coldest temperatures in the universe — much colder, in fact, than the electromagnetic radiation that permeates the vacuum of interstellar space. At those extreme temperatures, quantum effects dominate and the collective behaviour of the atoms can have unexpected consequences. For example, Bose-Einstein condensation may occur where the atoms lose their individual identities to coalesce into a macroscopic quantum particle.

Although such ultracold atomic gases are interesting in their own right, much of the excitement generated in this field is due to the possibility that studying these gases could shed light on intractable problems in other areas of physics. This is predominantly due to the uniquely high degree of control over various physical parameters that ultracold atomic gases afford to experimentalists. Recent technological advances exploit this advantage to study quantum phenomena in a detail that would not be possible in other systems. For instance, atoms can be made to attract or repel each other, the strength of this interaction can be set to almost any value, and external potentials of various geometries and periodicities can be introduced. In this way, atoms can be used to model phenomena as diverse as the quark-gluon plasmas arising in high-energy particle physics, the colour superfluids conjectured to exist in the core of neutron stars, and the high-temperature superconductivity exhibited by electrons on the ion lattice of certain compounds. Indeed, ultracold atomic gases also have a

demonstrated applicability to quantum information and computation.

Due to a subtle interplay between electronic and nuclear spins known as the hyperfine interaction, atoms can have either an integer or half-integer total spin quantum number, making them either bosonic or fermionic at low temperatures, respectively. With the exception of chapter 7, the work presented here concerns fermionic atoms in periodic potential formed by interfering laser beams. Indeed, the standing light wave created by the interfering beams gives rise to a lattice potential because of the Stark effect which couples the electronic energy levels of the atoms to the spatially undulating electric field.

Furthermore, fermionic atoms can be prepared in two different hyperfine states corresponding to the "spin-up" and "spin-down" quantum states, and as such mimic electrons moving in the lattice structure of solids. This system is well described by the famous Hubbard model which we introduce in chapter 2 and, under certain conditions, undergoes a phase transition into the *Néel state* which believed to be a precursor to superconductivity in certain high-temperature superconductors. In chapter 3, we calculate precisely how the Néel state may be achieved in an ultracold fermionic atom gas.

When the number of spin-up and spin-down atoms is unequal the system becomes spin-canted and exhibits both ferro- and antiferromagnetic characteristics, as we show in chapter 4. We also find there are topological excitations present in the quantum spin texture known as merons which have never unambiguously been observed before.

In order to form a Bose-Einstein condensate, fermionic atoms must first form pairs, and can do so in two contrasting ways. The relationship between these two qualitatively different forms of pairing is described in chapter 5, and we examine how these two types of pairs transform into one another in an optical lattice in chapter 6.

Finally, chapter 7 is a detailed field-theoretic study of pairing as it occurs in an ultracold Bose gas. There, we find there is an intriguing bosonic analogy of the two forms of fermion pairing and explore the properties of these pairs.

Samenvatting

In deze scriptie worden een aantal bijzondere fenomenen verkend die plaats vinden waneer een gas van neutral atomen gekoeld word tot de koudste temperaturen in het universum, veel kouder nog zelfs dan de elektromagnetische straling in het vacuüm van de interstellaire ruimte. Bij deze extreme temperaturen domineren kwantum effecten en kan het gezamenlijke gedrag van de atomen onverwachte effecten hebben. Bose-Einsteincondensatie kan bijvoorbeeld plaats vinden waarbij de atomen hun individuele identiteit verliezen en samensmelten tot een macroscopisch kwantumdeeltje.

Hoewel zulke ultrakoude atomaire gassen op zichzelf al interessant genoeg zijn, komt veel van het enthousiasme in dit gebied door de mogelijkheid dat onderzoek naar deze gassen lastige problemen in andere delen van de fysica zou kunnen ophelderen. Dit komt voornamelijk omdat experimentalisten met uitzonderlijk hoge precisie ultrakoude atomaire gassen kunnen beheersen. Hier word gebruik van gemaakt door recente technologische vernieuwingen om kwantumfenomenen te bestuderen in veel meer detail dan in andere systemen mogelijk is. Zo kan men controleren of de atomen elkaar aantrekken of afstoten, aan de sterkte van de interactie kan bijna elke waarde worden toegekend, en externe potentialen van verschillende vorm en periodiciteit kunnen worden geintroduceerd.

Op deze manier kunnen atomen worden gebruikt om diverse fenomenen te modeleren, zoals quark-gluon plasmas die te vinden zijn in de hoge energie fysica, de kleursupervloeibaarheid die verwacht worden in de kern van neutronensterren, en de hogetemperatuursupergeleiding die elektronen

vertonen op de ionroosters van zekere stoffen. Het is zelfs zo dat ultrakoude atomische gassen toepassingen hebben in het gebied van kwantuminformatie en -computatie.

Door een subtiel wisselwerking tussen electronische en kernspins die bekend staan als de hyperfine interactie kunnen atomen zowel een geheel als een halftallig getal als spin hebben, waardoor bij lage temperaturen de gassen zowel bosonisch als fermionisch van karakter kunnen zijn. Met uitzondering van hoofdstuk 7, gaat deze scriptie over fermionische atomen in een periodieke potentiaal die gemaakt word door interfererende laserstralen.

Het licht vormt een roostervormige potentiaal voor de atomen door het Stark effect dat de elektronische energieniveaus van de atomen koppelt aan het elektrische veld in de staande lichtgolf. Verder kunnen de atomen in twee hyperfine toestanden worden geprepareerd die overeenkomen met de "spin-omhoog" en "spin-omlaag" kwantumtoestanden. Zo kunnen we elektronen, die zich bewegen op een rooster in een vaste stof, simuleren. Dit system wordt goed beschreven door het beroemde Hubbardmodel dat we in hoofdstuk 2 presenteren. Onder zekere omstandigheden ondergaat dit systeem een faseovergang naar de Néeltoestand, warvan men denkt dat het een voorbode is van supergeleiding in sommige hogetemperatuursupergeleiders. In hoofdstuk 3 rekenen we precies uit hoe deze toestand kan worden bereikt in een ultrakoud fermionisch atomair gas.

Als het aantal spin-omhoog en spin-omlaag atomen niet gelijk is vertoont het systeem zowel ferro- als antiferromagnetische eigenschappen, zoals we laten zien in hoofdstuk 4. We ontdekken daar ook topologische excitaties in de kwantumspintextuur, bekend als merons, die nog nooit eerder ondubbelzinnige zijn waargenomen.

Om een Bose-Einsteincondensaat te vormen, moeten fermionische atomen eerste paren vormen. Dit kan geburen op twee tegenovergestelde manieren. De relatie tussen deze twee kwalitatief verschillende soorten paring wordt beschreven in hoofdstuk 5, en we onderzoeken hoe deze twee soort paren met elkaar verbonden zijn in een optische rooster in hoofdstuk 6.

Tenslotte is hoofdstuk 7 een uitgebreide veldentheoretische studie van paring in een ultrakoude bosnische gas. We vinden en intrigerende bosnische analogie voor de twee vormen van paring.

Acknowledgements

So many people have helped me more than they realise in the last few years that this section can only be at best incomplete. Nevertheless, I would like to acknowledge the support of a few people who have played an integral role.

First of all, I would like to thank my supervisor, Henk Stoof. More than a world renowned physicist and research director of the Institute for Theoretical Physics, he is also a person who genuinely takes the well being of his students to heart, whose quickness of thought has not eroded his patience, and who is generous with his time however little he has of it. I am very fortunate indeed to have had such brilliant guidance over the last four years.

Much of the work in this thesis was accomplished in part with the help and advice of Rembert Duine who joined the ITP faculty in 2006. His relaxed, jovial demeanour veils the serious and creative physicist that lies beneath.

My time at the ITP was very pleasant thanks in no small part to the academic and administrative staff, postdocs and my fellow PhD students. In particular, I would like to thank Koos Gubbels and Lih-King Lim who have been great company both here and away at conferences during our transformation from being the "new kids" to becoming the "old dogs", and also Dennis Dickerscheid, Mathijs Romans, Giovanni Maria Falco, Masud Haque, Pietro Massignan, and Achilleas Lazarides for many interesting discussions and physics advice. Thank you also Michiel Snoek, Bas Zoe-

tekouw, Daniele Oriti, Brendan Foster and Hedwig van Driel for the very convivial atmosphere in the office, helping me with all the little problems, and for putting up with my computer that sounds like a vacuum cleaner during a power surge each time I launch a computation.

My close friends have been a pillar of my life in Utrecht over the past few years; Aaron Chase, Aaron Swaving, Asya Zhelyazkova, Dirk Smits, Jordan Rizov, Sofie Willems, Gabriel Grigorescu, Chris Hawle, Andor Lukacs, Catalin "I-gura K. Kuru" Rusu, Tijmen Wisman, Emanuele Simili, Dimos Ntanis, Xhevdet "Gigo" Gegollaj, Emi Kirilova, Adam Ehrat, Lila Zotou, Gentian Zyberi, Emma Sydenham, Jan-Bas de Graaff, Zuzana Rychnavska, Ianina Lipara, Elspeth Greer, Madalina Busuioc, Ramona Biholar, Shamiso Zinzombe, Nancy Djadda, Sasha Zozulya, Liesbeth Gulpers, and Arne Verliefde, I relish the memories of the wonderful times we shared. Chris, Gabriel, Cata and Tijmen kept the jazz alive in my fingers, and opened up a new direction in music for me. My Kiwi compatriots and life-long friends Adam and Aaron cultivate a small patch of New Zealand in Utrecht that swiftly whisks away any homesickness and, in truth, without the collaboration and mutual support of Aaron I would not even have made it to the Netherlands. I look forward to more happy times, exciting travels, engrossing discussions, and an enduring friendship with all of you in the future.

Thank you to my family in NZ – my mum Brigitte and brother Alain – for being there during tough times, je sais que je peux toujours compter sur vous! I am also very grateful to my supportive extended family in the Netherlands, France and England.

Finally, I feel deeply indebted to my girlfriend, Erta Mosho, for the magnificent times we spent together during the past three years, and for her caring, unwavering support and encouragement of which I am certainly undeserving.

Curriculum Vitae

Arnaud Koetsier was born in Neuilly sur Seine, Paris on September 16$^{\text{th}}$, 1980. After living six years in Kuala Lumpur, Malaysia, he moved to Auckland, New Zealand in 1989 where he attended Waiheke High School and the Senior College of New Zealand before studying for a bachelors degree in physics and mathematics at the University of Auckland. He joined the Masters in Theoretical Physics program at Utrecht University in 2002, writing a dissertation in high-energy physics entitled "Matrix Models of 2D String Theory in Non-trivial Backgrounds" under the guidance of prof.dr. G. 't Hooft. In 2005 he joined the BEC group of prof.dr.ir. H. T. C. Stoof as a PhD researcher at the Institute for Theoretical Physics of Utrecht University, where he published a number of research articles and presented work at several international conferences. He will defend this PhD thesis on July 6$^{\text{th}}$, 2009.

Publications

- Arnaud Koetsier, D. B. M. Dickerscheid, H. T. C. Stoof, *BEC-BCS crossover in an optical lattice*, Phys. Rev. A **74**, 033621 (2006)
- Arnaud Koetsier, R. A. Duine, Immanuel Bloch, H. T. C. Stoof, *Achieving the Néel state in an optical lattice*, Phys. Rev. A **77**, 023623 (2008)
- Arnaud Koetsier, P. Massignan, R. A. Duine, H. T. C. Stoof, *A strongly interacting Bose gas: Nozières and Schmitt-Rink theory and beyond*, Phys. Rev. A **79,** 063609 (2009)
- Arnaud Koetsier, F. van Liere, and H. T. C. Stoof, *The imbalanced antiferromagnet in an optical lattice*, submitted to Nature Phys.